

Marquette University

e-Publications@Marquette

Dissertations (2009 -)

Dissertations, Theses, and Professional
Projects

Dual-modality Smartphone-based Fiber-optic Microendoscope System for Early Detection of Cervical Neoplasia

XIANGQIAN HONG

Marquette University

Follow this and additional works at: https://epublications.marquette.edu/dissertations_mu



Part of the [Engineering Commons](#)

Recommended Citation

HONG, XIANGQIAN, "Dual-modality Smartphone-based Fiber-optic Microendoscope System for Early Detection of Cervical Neoplasia" (2019). *Dissertations (2009 -)*. 883.

https://epublications.marquette.edu/dissertations_mu/883

DUAL-MODALITY SMARTPHONE-BASED FIBER-OPTIC
MICROENDOSCOPE SYSTEM FOR EARLY
DETECTION OF CERVICAL
NEOPLASIA

by

Xiangqian Hong, B.S., M.E.

A Dissertation submitted to the Faculty of the Graduate School,
Marquette University,
in Partial Fulfillment of the Requirements for
the Degree of Doctor of Philosophy

Milwaukee, Wisconsin

August 2019

ABSTRACT
DUAL-MODALITY SMARTPHONE-BASED FIBER-OPTIC
MICROENDOSCOPE SYSTEM FOR EARLY
DETECTION OF CERVICAL
NEOPLASIA

Xiangqian Hong, B.S., M.E.

Marquette University, 2019

Cervical cancer remains the leading cause of death for women in low middle-income countries (LMICs), where the incidence and mortality of cervical cancer are disproportionately high. Due to the poor medical conditions and lack of resources, the benefits of early screening methods such as Pap smear and HPV test have yet to be realized in these areas. The more viable screening option - visual inspection with acetic acid (VIA) is relatively easier to implement and lower in cost. However, the effectiveness of VIA on the early detection of cervical cancer is still in question because of its low specificity, which may lead to many unnecessary follow-up diagnoses and treatments.

Optical endoscopy is a powerful tool for detecting pre-cancerous changes in the epithelial tissue of the cervix. In this dissertation, we report the design and development of a dual-modality fiber-optic microendoscope system (SmartME) that integrates high-resolution fluorescence imaging (FLI) and quantitative diffuse reflectance spectroscopy (DRS) onto a smartphone platform. A smartphone App has also been developed to control the SmartME, pre-process the data, and wirelessly communicate with a remote server where the image and data are processed to extract diagnostically meaningful tissue parameters. The SmartME device has been thoroughly tested and calibrated. The FLI has a spatial resolution of $\sim 3.5 \mu\text{m}$, which allows imaging of subcellular organelles and determining the nuclear-cytoplasmic ratio of epithelial tissues. The DRS has a spectral resolution of 2 nm and is capable of measuring optical properties of epithelial tissues with a mean error of $\sim 5\%$, which is comparable to what can be achieved with a commercial spectrometer. The feasibility of the device in measuring biological samples has been verified *ex vivo* using monolayer cervical cancer cells, tumor tissue from xenograft solid tumor models and other normal tissues. *In vivo* study on healthy human oral mucosa tissues has demonstrated that the SmartME can noninvasively quantify the tissue parameters and distinguish between different tissue types. The SmartME may provide a compact, cost-effective, and globally connected solution for early detection of neoplastic changes in epithelial tissues.

ACKNOWLEDGMENTS

Xiangqian Hong, B.S., M.E.

I would first like to thank my family for their unwavering support throughout my pursuit of Ph.D. degree.

I would like to express my greatest appreciation to my advisor Dr. Bing Yu for his continuous guide and support over the years. His expertise, advice, and enthusiasm really inspired and prepared me to start a career in healthcare. I would also like to thank my Ph.D. committee: Dr. Taly Gilat-Schmidt, Dr. Said H. Audi, Dr. Amit Joshi, and Dr. Anjishnu Banerjee, for their insightful comments and suggestions.

I am thankful to all members at Yu Lab for their help and support, especially Liam Fruzyna for his assistance in developing software for this project. I would like to thank all who have helped me to develop new skills and collaborators I had the pleasure to work with.

TABLE OF CONTENTS

ACKNOWLEDGMENTS	i
TABLE OF CONTENTS.....	ii
LIST OF TABLES	v
LIST OF FIGURES	vi
CHAPTER 1: INTRODUCTION AND BACKGROUND	1
1.1 CERVICAL CANCER	1
1.1.1 HPV infection leads to cervical cancer	1
1.1.2 High incidence and mortality rates in LMICs.....	1
1.2 CERVICAL CANCER SCREENING.....	2
1.2.1 Screening in developed countries	3
1.2.2 Screening in LMICs.....	5
1.2.3 Challenges for cervical cancer screening in LMICs	7
1.3 OPTICAL ENDOSCOPY FOR CERVICAL NEOPLASIA DETECTION	7
1.3.1 Optical coherence tomography	8
1.3.2 Raman spectroscopy	9
1.3.3 Fluorescence imaging	10
1.3.4 Diffuse reflectance spectroscopy	11
1.3.5 Combined techniques.....	12
1.4 SMARTPHONE IN HEALTHCARE.....	14
1.5 SOLUTION: SMARTPHONE-BASED DUAL-MODALITY FIBER-OPTIC MICROENDOSCOPE.....	15
1.6 OUTLINE OF THEIS.....	16
CHAPTER 2: SMARTPHONE-BASED FLUORESCENCE IMAGING.....	19
2.1 INTRODUCTION	19
2.1.1 Fluorescence process	19
2.1.2 Absorption and fluorescence of Proflavine.....	22

2.2 OPTICAL DESIGN	22
2.2.1 System layout.....	22
2.2.2 Simulation of imaging module.....	24
2.2.3 Simulation of illumination module	27
2.2.4 System assembly	29
2.3 PERFORMANCE CHARACTERIZATION.....	32
2.3.1 Imaging a uniform fluorescence reference slide	32
2.3.2 Fiber bundle pixelation artifact removal.....	33
2.3.3 Spatial resolution characterization.....	36
2.3.4 Fluorescence imaging of biological samples	37
2.3.5 Quantitative information: nuclear-cytoplasmic ratio	39
2.4 DISCUSSION	41
CHAPTER 3: SMARTPHONE DIFFUSE REFLECTANCE SPECTROSCOPY	45
3.1 DIFFUSE REFLECTANCE SPECTROSCOPY	45
3.1.1 Diffuse reflectance	46
3.1.2 Tissue optical properties	47
3.1.3 Modeling of light-tissue interaction using Monte Carlo simulation	49
3.2 OPTICAL DESIGN	53
3.2.1 System layout.....	53
3.2.2 Ray-tracing simulation.....	54
3.2.3 System assembly	58
3.3 PERFORMANCE CHARACTERIZATION.....	61
3.3.1 Wavelength calibration and resolution verification.....	61
3.3.2 Phantom validation	64
3.4 DISCUSSION	66
CHAPTER 4: A DUAL-MODALITY SMARTPHONE MICROENDOSCOPE FOR QUANTIFYING THE PHYSIOLOGICAL AND MORPHOLOGICAL PROPERTIES OF EPITHELIAL TISSUES.....	69

4.1 HARDWARE DEVELOPMENT	69
4.1.1 SmartME instrumentation	69
4.1.2 Fabrication of miniature fiber-optic probe.....	72
4.2 SOFTWARE DEVELOPMENT	74
4.2.1 Smartphone App development.....	74
4.2.2 Wireless communication with the server.....	77
4.3 PERFORMANCE VERIFICATION AND IN VIVO STUDY	79
4.3.1 System performance characterization	79
4.3.2 <i>Ex vivo</i> measurements of biological samples.....	80
4.3.3 <i>In vivo</i> measurements of healthy oral tissue	82
4.4 DISCUSSION	87
CHAPTER 5: CONCLUSIONS AND SUGGESTED FUTURE WORK	89
5.1 SUMMARY	89
5.2 SIGNIFICANCE OF THIS WORK.....	91
5.2 FUTURE INVESTIGATIONS.....	93
BIBLIOGRAPHY	95

LIST OF TABLES

Table 1-1: Effectiveness of current cervical cancer screening methods.....	7
Table 1-2: Summary of advanced optical techniques in cervical cancer detection	13
Table 2-1: Values defined in the LDE for FLI module (optimized).....	25
Table 2-2: Non-sequential component editor including illumination module.....	28
Table 3-1: Values defined in the LDE for DRS.....	57
Table 3-2: Wavelength calibrated using third-degree polynomial fitting.....	63
Table 3-3: Expected phantom properties averaged over 430 nm – 630 nm	65

LIST OF FIGURES

Figure 1-1: Estimated cervical cancer incidence and mortality rates worldwide in 2018..	2
Figure 1-2: Schematics of cervical intraepithelial neoplasia development	3
Figure 1-3: Morphology of cervical epithelial cells	5
Figure 1-4: Acetowhitening phenomenon during VIA test	6
Figure 1-5: HRME system developed by Richards-Kortum group	10
Figure 2-1: Jablonski diagram illustrating the three-stage process of fluorescence	20
Figure 2-2: Excitation and emission spectra (generic)	21
Figure 2-3: The fluorescence excitation and emission spectra of Proflavine in water	22
Figure 2-4: Schematic diagram of the smartphone microendoscope for FLI	23
Figure 2-5: Simulation of fluorescence imaging system	25
Figure 2-6: Simulation of imaging quality.....	27
Figure 2-7: Simulation of fiber bundle light coupling	29
Figure 2-8: Exploded view of all components for FLI	30
Figure 2-9: The completed smartphone FLI system	32
Figure 2-10: Fluorescence image of a uniform fluorescence reference slide	33
Figure 2-11: Flowcharts for image calibration and fiber pattern removal.....	34
Figure 2-12: Fiber pattern removed image of the uniform fluorescence reference slide..	35
Figure 2-13: Fluorescence images taken from a 1951 USAF resolution target.....	36
Figure 2-14: Fluorescence images of <i>ex vivo</i> tissue.....	38
Figure 2-15: Fluorescence images of <i>ex vivo</i> cell line and <i>in vivo</i> oral mucosa tissue.....	39
Figure 2-16: Inverted images for N/C extraction.....	41
Figure 2-17: Compare between smartphone-based FLI system with HRME.....	42
Figure 3-1: Schematic representation of light-tissue interaction	46
Figure 3-2: Absorption spectra of HbO ₂ and Hb	48
Figure 3-3: Illustration of source-detection-separation.....	50

Figure 3-4: Forward and inverse models of Palmer’s fast Monte Carlo simulation.....	53
Figure 3-5: Schematic diagram of the smartphone-based DRS.....	54
Figure 3-6: Diagram showing light incident normally to a transmission diffraction grating	56
Figure 3-7: Ray-tracing simulation of the DRS system.....	58
Figure 3-8: Exploded view of all components for DRS	59
Figure 3-9: Collimation of light from a fiber.....	60
Figure 3-10: The completed smartphone DRS system	61
Figure 3-11: Raw and cropped spectral images of calibration lamps.....	61
Figure 3-12: Peak wavelengths used for wavelength calibration	62
Figure 3-13: Spectrum of a monochromatic light source	64
Figure 3-14: Spectra of liquid phantoms	65
Figure 3-15: Extracted vs. expected μ_a and μ_s' for all phantoms	66
Figure 3-16: Compare between smartphone-based DRS system with a commercial spectrometer.....	67
Figure 4-1: Schematic diagram of the SmartME	71
Figure 4-2: The completed SmartME device.....	72
Figure 4-3: Picture of the integrated dual-modality endoscope probe.....	73
Figure 4-4: Architecture of the smartphone App.....	75
Figure 4-5: Screenshots of the SmartME App.....	76
Figure 4-6: Image snipping and wavelength calibration in the App.....	77
Figure 4-7: SmartME remote server	78
Figure 4-8: Display of results in the App.....	79
Figure 4-9: Fluorescence images of HeLa cells.....	80
Figure 4-10: Fluorescence image of tumor tissue <i>in vitro</i>	82
Figure 4-11: DRS and FLI measurements of healthy oral tissues	84
Figure 4-12: Quantitative analysis of tissue properties.....	86
Figure 5-1: The development history of SmartME.....	89

Figure 5-2: Benefits of using SmartME in clinical applications..... 92

CHAPTER 1: INTRODUCTION AND BACKGROUND

1.1 CERVICAL CANCER

1.1.1 HPV infection leads to cervical cancer

Human papillomavirus (HPV) is a widespread viral infection of the reproductive tract.^[1] Although about 90% HPV infections disappear spontaneously without any medical intervention in 6 months to 2 years ^[2], persistent infections with certain cancer-causing HPV may become chronic and pre-cancerous lesions, progress either to high-grade cervical intraepithelial neoplasia (CIN) or to invasive cancer.^[3] More than 150 different types of HPV have been identified, of which 14 HPV types, including HPV 16, 18, 31, 33, 35, 39, 45, 51, 52, 56, 58, 59, 66 and 68, are considered cancer-causing or “high-risk”.^[4] Particularly, HPV 16 and 18 are most commonly associated with the development of cervical cancer and are known to cause more than 70% of all cervical cancers.^[1] A 60-year study evaluating HPV infections in more than 10,000 confirmed invasive cancer cases in 38 countries around the world has revealed that cancer-causing types of HPV are detected in nearly all cervical cancers.^[5]

1.1.2 High incidence and mortality rates in LMICs

Globally, cervical cancer remains the fourth most common cancer in women with an estimated 570,000 new cases in 2018 and 311,000 deaths every year.^[6] Besides, the number of deaths keeps increasing and it is estimated to reach 460,000 per year by 2040. In 2018, approximately 84% of new cases and 90% of deaths due to cervical cancer occur in LMICs.^[6] Figure 1-1 shows the latest incidence and mortality rates of cervical cancer

worldwide. The disproportionately high incidence and mortality rates in LMICs are mainly due to limited access to early preventative methods. In most cases, cervical cancer is not detected until it has progressed to invasive cervical cancer in these countries, resulting in a higher rate of death from cervical cancer.

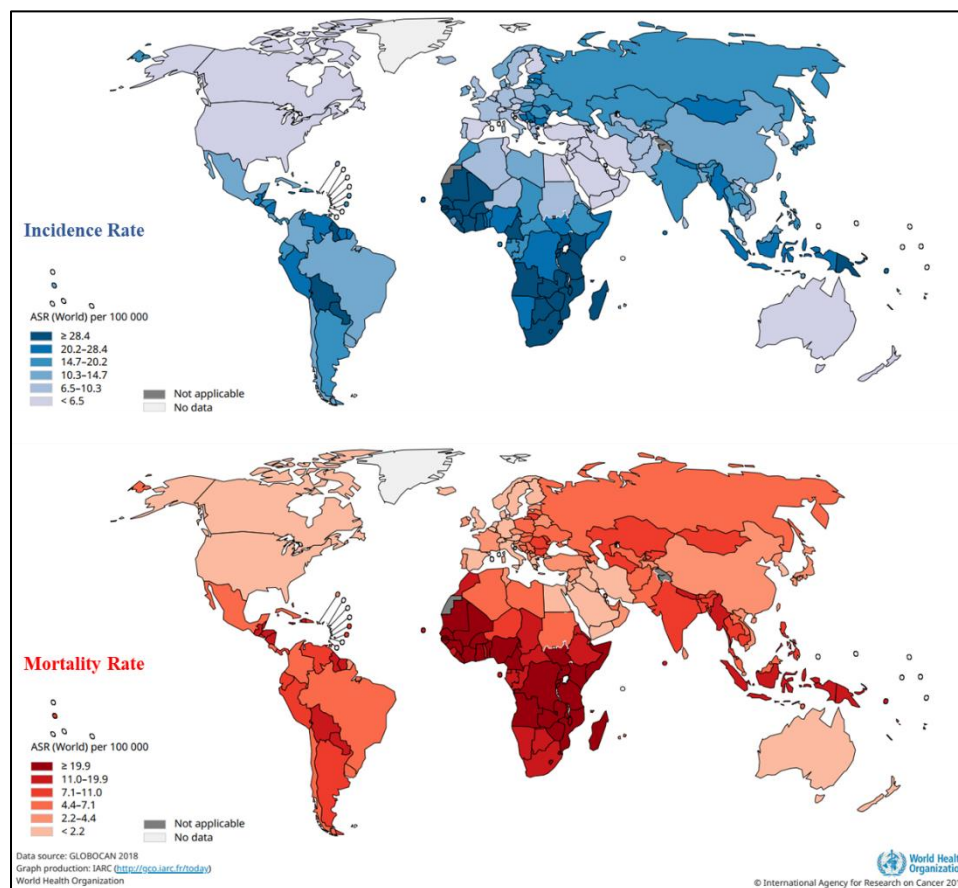


Figure 1-1: Estimated cervical cancer incidence and mortality rates worldwide in 2018

1.2 CERVICAL CANCER SCREENING

In general, the precancerous change of cervical tissue can be classified into three stages, namely CIN1/CIN2/CIN3, based on the thickness of the affected epithelium tissue. CIN1 is the mild intraepithelial neoplasia when one-third of the epithelium is affected. While the higher degree lesions, CIN2 and CIN3 have dysplasia about two

thirds and all of the epithelium layer, respectively.^[7] The high-grade cervical intraepithelial neoplasia (CIN2+) will eventually progress into invasive cancer if left untreated (Figure 1-2). Early detection and treatment is the key to saving a patient's life. Early screening allows pre-cancerous lesions to be detected at an early stage when treatment has a high cure rate. Studies suggest that ~90% of the patients who were diagnosed at an early stage (stage I) lived more than five years, while the 5-year survival rates for stage II and III are less than 50% and 10%, respectively.^[8]

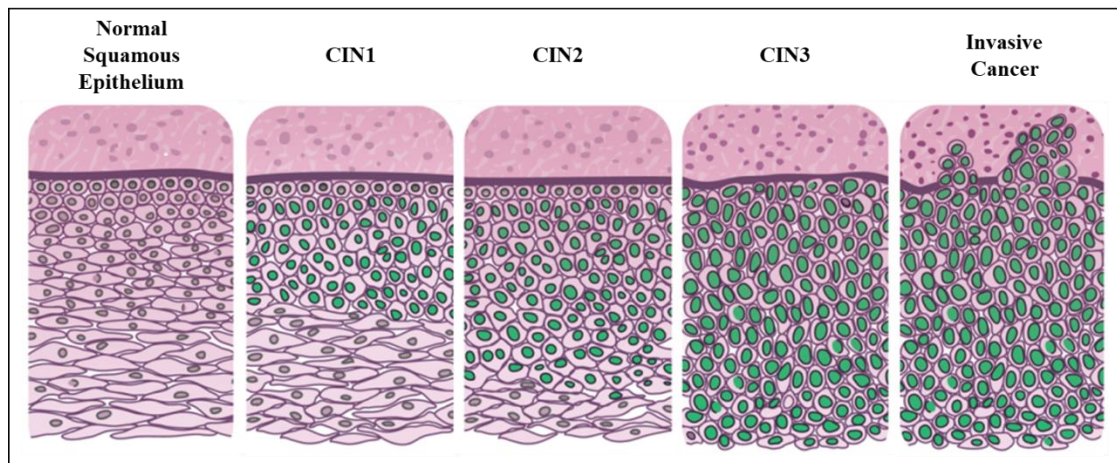


Figure 1-2: Schematics of cervical intraepithelial neoplasia development

(Photo credit: Novikova, T. Adapted from reference 7)

1.2.1 Screening in developed countries

In developed countries, a comprehensive approach has been developed for cervical cancer prevention, diagnosis and treatment. It includes HPV vaccination of girls starting as early as age 9, regular screening and diagnosis, and treatment of pre-cancer lesions for women from age 30. Particularly, the regular screening allows pre-cancerous lesions to be detected at an early stage when treatment has a high cure rate. In the US, cervical cancer deaths have been reduced by 70% since 1941 when the Papanicolaou

(Pap) smear screening was first introduced.^[9] Pap smear screening is still the primary approach in early detection of cervical cancer at present. The common procedures of a Pap smear test involve the collection of cells from the cervix for microscopic examination and identification of abnormal cells based on cytological characteristics, such as altered nuclear shape and increased nuclear size, which have been reported to be associated with cancer cells.^[10] The Bethesda system (TBS) is a widely used system for reporting Pap smear results. A low-grade squamous intraepithelial lesion (LSIL) usually indicates mild intraepithelial neoplasia (CIN1). Expanded nucleus with a size at least three times bigger than the normal nucleus can be observed, leading to an increased nuclear-cytoplasmic ratio (N/C). A high-grade squamous intraepithelial lesion (HSIL) indicates moderate intraepithelial neoplasia (CIN2) and severe intraepithelial neoplasia (CIN3). Cells in HSIL have expanded nuclei with reduced cytoplasm, leading to an even larger N/C than LSIL, as illustrated in Figure 1-3^[11]. Studies have shown that using nuclear morphometry such as nuclear size/diameter^[12] and N/C^[13] can effectively differentiate LSIL from HSIL and malignant cervical smears. The collected cells during a Pap smear test can also be used for the HPV test, which has been typically used as an adjunct to the Pap smear because of the high prevalence of HPV infection in the absence of cervical disease.^[14]

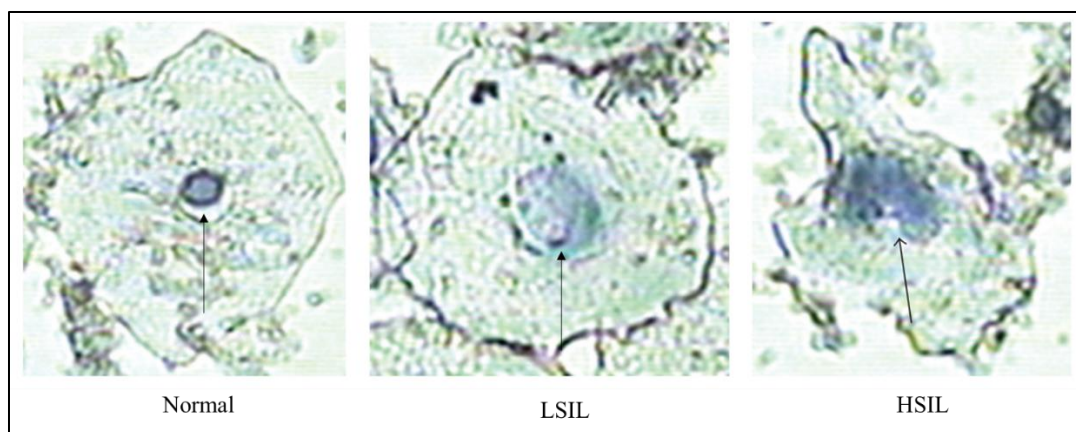


Figure 1-3: Morphology of cervical epithelial cells

(Photo credit: Yang, L., *et al.* Reference 11)

1.2.2 Screening in LMICs

Due to the lack of resources in LMICs, the benefits of the regular cervical cancer screening have yet to be realized in LMICs.^[15-17] Employing Pap smear and HPV test requires multiple visits, a centralized laboratory, and skilled staff for processing and evaluation of cytology, virology, and pathology specimens.^[18,19] The Alliance for Cervical Cancer Prevention has suggested a see-and-treat paradigm for cervical cancer prevention in LMICs.^[20] The most viable option is to screen using a more cost-effective method called visual inspection with acetic acid (VIA) or VIA with magnification (VIAM) and to treat the pre-cancerous lesions using loop electrosurgical excision procedure (LEEP) or cryotherapy.^[21-23] Performing a VIA test starts with a vaginal speculum exam during which diluted acetic acid (5%) will be applied to the cervix. Due to the acetowhitening phenomenon, as shown in Figure 1-4, the tissue in the abnormal area will temporarily turn white when exposed to acetic acid. Suspicious lesions will be identified by viewing the cervix to identify color changes on the cervix.^[24,25] However, studies have shown that the acetowhitening phenomenon is not exclusive to precancerous

lesions, normal epithelial tissue with infection or inflammation may appear similar to the positive ones, which leads to a lower accuracy for pre-screening. Although coagulation of the nucleoprotein and polymerization of cytokeratin have been hypothesized as the physical origin of the acetowhitening phenomenon^[26,27], the mechanism of acetowhitening effect is still not fully understood.^[28] Many efforts have been made to improve the performance of acetowhitening-based inspection, including modeling the temporal pattern of acetowhitening (rising and decay)^[29-31] or quantitatively measuring the intensity of backscattered light during acetowhitening process^[32-34] in benign and suspicious lesions. However, large variability in findings or even contradictory results in the acetowhite temporal patterns were observed from measurements in the cell suspension^[28] and tissue *in vivo*^[32,33]. The acetowhite rising and decay pattern is highly dependent on the concentration of acetic acid applied and is very sensitive to the physical conditions of the tissue which are related to patient age and race, the stage of menstruation, or the way colposcopy is performed.^[35]

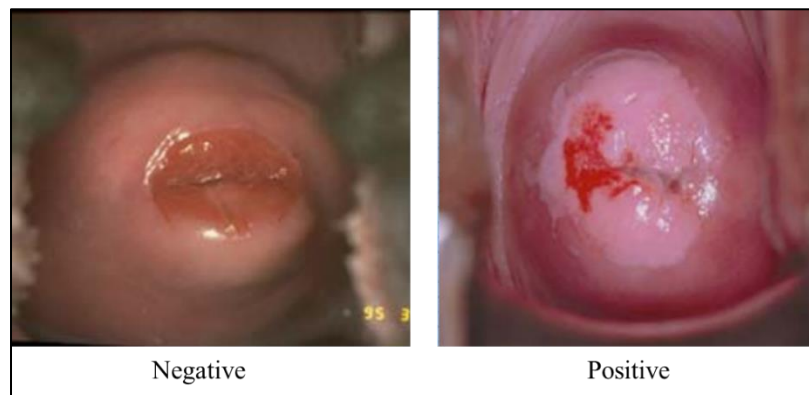


Figure 1-4: Acetowhitening phenomenon during VIA test

(Photo credit: Gaffikin *et al.* Adapted from reference 24)

1.2.3 Challenges for cervical cancer screening in LMICs

Sensitivity and specificity are two statistical measures that are widely used to quantify the diagnostic performance in medical diagnosis. Sensitivity, also known as the true positive rate, measures the proportion of patients with the disease who will be identified to have a positive result. Specificity, also known as the true negative rate, is defined as the proportion of patients without the disease who will be identified to have a negative result. Table 1-1 illustrates the effectiveness of VIA/VIAM in terms of sensitivity and specificity when compared to the Pap smear test. Although the sensitivity of the VIA/VIAM approach is as good as, if not better than, the Pap smear, the specificity is significantly lower.^[36-39] In a see-and-treat paradigm, this would cause a large amount of overtreatment and unnecessary health care (e.g., biopsy and follow-ups), which would reduce the effectiveness of this approach. Consequently, there is a critical global need for affordable, effective point-of-care strategies to improve the screening and early diagnostic rates of cervical cancer in LMICs.

Table 1-1: Effectiveness of current cervical cancer screening methods

	Sample size	Sensitivity	Specificity	Reference
Pap smear	16951	40.7 - 73.7%	87.7%	[36]
	1500	75.8%	98.05%	[37]
	200	50.1%	93.1%	[38]
VIA/VIAM	16951	21.9 – 73.6%	84.2%	[36]
	350	82.14%	50%	[39]
	200	90%	37%	[38]

1.3 OPTICAL ENDOSCOPY FOR CERVICAL NEOPLASIA DETECTION

Biophotonics is an emerging interdisciplinary field that studies biomolecules, cells and tissues using optical techniques. The advent of optical endoscopy techniques has made it possible to noninvasively acquire biological and morphological information deep within the cervical tissue. White light endoscopy, such as reflectance colposcopy, is a standard tool that has been extensively used in cervical cancer screening, diagnosis, and treatment. In the past decades, various high-resolution imaging modalities, including optical coherent tomography (OCT),^[40-44] Raman spectroscopy,^[45-50] fluorescence imaging,^[51-53] fluorescence spectroscopy^[54-56], diffuse reflectance spectroscopy,^[57-61] and photoacoustic imaging^[62,63] narrow-band imaging,^[64-67] have been successfully incorporated into endoscopic probes for early detection and delineation of epithelial neoplasia.

1.3.1 Optical coherence tomography

Studies on OCT have been growing rapidly in recent years. It is one of the most promising technologies for non-invasive imaging of biological tissue, especially in the clinical diagnosis of ophthalmology, dentistry and dermatology. OCT uses near-infrared light and low-coherence interferometry to take cross-sectional images of the internal structure of the biological tissue. By using the principle of interference, signals of tissue at different depths can be obtained. OCT provides a typical resolution of 1-15 μm and up to 4 mm penetration depth by using near-infrared light.

Researchers have conducted pilot studies on applying OCT in the detection of cervical neoplasia. Gallwas *et al.* reported a sensitivity of 95% and a specificity of 46% for the detection of neoplasia and cancerous lesions using OCT in 60 patients.^[68] Another

study on discriminating different CIN grades in 120 patients achieved an averaged sensitivity of 97% and specificity of 40%, respectively, with the threshold at CIN 1. The sensitivity decreased to 85% with the threshold at CIN 2, while the specificity increased to 62%.^[40] These studies demonstrate the high sensitivity of OCT in distinguishing neoplasia grades and cancerous lesions. However, it was relatively more difficult to differentiate the CIN1 and the healthy tissue (false positive) due to other benign modifications, which resulted in a much lower specificity of OCT. The same group reported improved specificity of 69% in a more recent study by combining OCT and microscopy.

1.3.2 Raman spectroscopy

Raman spectroscopy is another promising tool that can be used in the early diagnosis of cancer due to its capability of obtaining highly detailed spectroscopic information of the tissue. During the development of cancer, the structure of proteins, nucleic acids, lipids, and carbohydrates changes. These changes can be effectively detected by Raman spectroscopy to reveal the underlying molecular structure and precancerous modifications. Raman spectroscopy can provide rich structural features and molecular fingerprint at the molecular level.

The feasibility of using Raman spectroscopy as a label-free diagnostic method for the early detection of cervical cancer has been studied by different groups. Duraipandian *et al.* achieved an average accuracy of 82.6% by using simultaneous fingerprint and high-wavenumber confocal Raman spectroscopy in an *in vivo* study.^[50] Another study indicates that Raman spectroscopy can discriminate high-grade dysplasia lesions from

healthy tissue with a sensitivity of 89% and specificity of 81%, both are higher when comparing to regular colposcopy, which has a sensitivity and specificity of 87% and 72%, respectively. [69]

1.3.3 Fluorescence imaging

Endoscopic FLI with a fluorescence dye allows imaging of subcellular organelles, such as cell nuclei of the mucosa of the cervix. To improve the efficacy of cervical cancer screening in LMICs, fiber-optic endoscopes have been developed for high-resolution fluorescence imaging of cell nuclei. [30,51,70,71] The Richards-Kortum group reported a high-resolution fluorescence microendoscope (HRME) [72,73], shown in Figure 1-5, based on a fiber bundle for molecular imaging of cell culture and living tissue. Two pilot studies conducted by Pierce *et al.* and Quinn *et al.* demonstrated the use of nuclear-cytoplasmic ratio (N/C) obtained with the HRME achieved a sensitivity of 100% and specificity of 65%, [52] and a sensitivity of 86% and specificity of 87%, [53] respectively, in differentiating CIN2+ lesions from non-neoplastic cervical tissues.

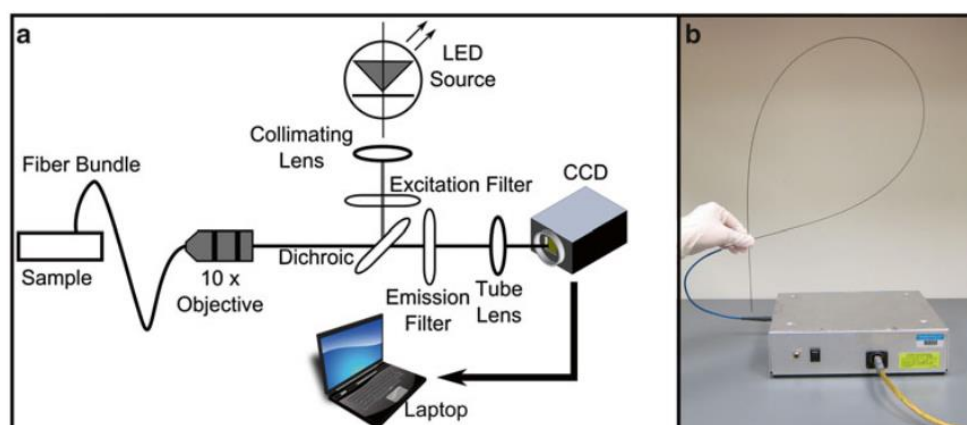


Figure 1-5: HRME system developed by Richards-Kortum group

(Photo credit: Grant, B. D, Springer. Reference 64)

However, the reported HRME system uses expensive components such as the scientific camera^[72] or DSLR camera^[74], and the system has to connect to a local computer, which limits its portability and makes the system less easy-to-use. Therefore, additional studies are required to reduce the size and cost of the endoscopic fluorescence imaging system while maintaining its effectiveness in the early detection of cervical cancer.

1.3.4 Diffuse reflectance spectroscopy

Diffuse reflectance spectroscopy is very sensitive to the optical properties of epithelial tissue^[75-78] and has demonstrated its potential for early detection of cancers in cervix,^[79-84] oral cavity,^[85-89] colon,^[57,61,90,91] and Barrett's esophagus.^[58,59,92] The absorption (μ_a) and reduced scattering coefficients (μ'_s) of epithelial tissues reflect their underlying physiological and morphological properties.^[93] For instance, dominant absorbers in the visible wavelength range in cervical tissues include oxy-hemoglobin and deoxy-hemoglobin, arising from blood vessels in the stroma. Light scattering is primarily caused by cell nuclei and organelles in the epithelium and stroma, as well as collagen fibers and cross-links in the stroma. Neoplastic epithelial tissue exhibits significant changes in their physiological and morphological characteristics that can be quantified optically given that the stromal layer absorption is expected to increase with angiogenesis,^[78,84,94-96] resulting in decreased stromal scattering with the neoplastic progression that coincides with the degradation of extracellular collagen networks.^[78,85,93,97-99] In contrast, epithelial scattering increases due to increased nuclear size and DNA content, as well as hyperchromasia.^[78,84,93,94,100] In the visible wavelength range, DRS has a penetration depth that can be tuned to be comparable to the thickness of

the epithelial layer or deeper to probe both the epithelial and stromal layers.^[77,94,101]

These advantages enable DRS to be used as a cost-effective (<\$5,000), fast and sensitive tool for early detection of cervical cancer. Thekkek *et al.* have summarized several studies on cervical tissue optical spectroscopy^[51], in which DRS was shown to achieve sensitivities and specificities in the ranges of 83 – 92% and 80 – 90%, respectively.^[18]

1.3.5 Combined techniques

While imaging and spectroscopy are being actively studied, few imaging or spectroscopy modalities alone can achieve the high sensitivity and specificity required for early cancer detection, and often two or more are required to provide the physician or computer algorithm with complementary information about the lesion in question. A technique that is superior on one side may have limitations on the other side so that its application will be limited. For example, OCT allows high-resolution imaging at larger depths but cannot provide functional information of the tissue. Raman spectroscopy provides highly detailed spectroscopic information but has very weak signal and small field of view that limited within a small range of wavenumbers. Recent years have seen increasing research on the integration of multiple imaging modalities into a single device to obtain complementary tissue information.^[102-104] Freeberg *et al.* developed an instrument that combined fluorescence and reflectance spectroscopy for the detection of cervical neoplasia. An 850-patient clinical study using the instrument has shown significant differences in mean intensity between normal and high-grade tissue.^[105] Similar device developed by Twiggs *et al.* that combines fluorescence and reflectance spectroscopy achieved a sensitivity of 91.3% in differentiating high-grade lesions (CIN2+).^[106] However, the instruments used in both groups are not portable or globally

connected. The devices have to be connected to and controlled by a local computer for data acquisition and analysis, which limits their application in LMIC.

However, because most of these modern optical imaging methods are still in the early stage of development, it is hard to judge the diagnostic efficacy of each imaging modality.^[107] Table 1-2 summarizes the performance and research status of several common optical imaging techniques. The major drawbacks of current high-resolution endoscopes are the use of expensive (over \$10,000) and power-consuming light sources and detectors. Moreover, they often need experienced engineers to operate the sophisticated instruments and physicians to interpret the images, making them unaffordable to LMICs. Besides, some systems require a scanning mirror inside the endoscopes, which is bulky and incompatible with magnetic resonance imaging and computerized tomography scanners.

Table 1-2: Summary of advanced optical techniques in cervical cancer detection

Technique	Functional information	Morphological information	Depth (μm)	Imaging speed (s)	Research status	References
OCT	×	√	<4000	<2	Ex/In vivo	[40 - 44]
Raman spectroscopy	√	×	>1000	<5	Ex/In vivo	[45 – 50]
FLI	×	√	<100	<100	Ex/In vivo	[51 – 53]
FLS	√	×	<100	<15	Ex/In vivo	[54 – 56]
DRS	√	×	<2000	<1	Ex/In vivo	[57 – 61]

1.4 SMARTPHONE IN HEALTHCARE

The cost of wireless technology has decreased over the years^[108], thereby making smartphones, a subset of mobile phones, a very affordable device, even for people living in many rural areas and developing countries. The International Telecommunication Union reported that the mobile-broadband subscriptions reached 4.3 billion globally in 2017; Between 2012 and 2017, the most rural areas saw the largest growth rate of mobile broadband subscriptions. Mobile broadband becomes more affordable than fixed broadband in most developing countries.^[109] In addition to a high-resolution camera, smartphones also offer enormous computational power and wireless Internet access. The smartphone-based diagnosis could potentially reduce healthcare costs, provide wireless access to advanced laboratories, and experienced physicians in developed countries, thus revolutionizing healthcare delivery in LMICs.

Smartphones are playing an emerging role in optical imaging for medical and biological applications — for example, Breslauer *et al.*^[110] reported a mobile phone microscope with a field-of-view (FOV) of 180 μm in diameter and a 1.2 μm resolution for the diagnosis of hematologic and infectious diseases. Switz *et al.*^[111] added a reversed camera lens to a mobile phone to enable high-quality imaging over a FOV of $\sim 10\text{mm}^2$ and successfully identified red and white blood cells in blood smears and soil-transmitted helminth eggs in stool samples. Tseng *et al.*^[112] demonstrated a lens-free holographic microscope on a mobile phone that has been used to image variously sized microparticles. Zhu *et al.*^[113] reported wide-field FLI on a mobile phone over a FOV of $\sim 81\text{mm}^2$ with a resolution of $\sim 20\text{ }\mu\text{m}$. Smartphone spectrometers with nanometer to sub-nanometer accuracy have also been reported.^[114-120] Gallegos *et al.*^[115] demonstrated

the use of a smartphone spectrometer to measure shifts in the resonant wavelength of a label-free photonic crystal biosensor with 0.009 nm accuracy. Edwards *et al.*^[120] reported a miniature, visible to near-infrared G-Fresnel spectrometer that connected with a smartphone through a Micro USB port for measurement of hemoglobin. Wang *et al.*^[118] have proposed multiple methods for implementing smartphone-based spectroscopy. Smith *et al.*^[117] developed two attachments that transform a phone camera into either a microscope or a spectrometer.

Most smartphone imaging/spectroscopy devices utilize an external module attached to the rear camera of a smartphone, but only a few attachments have been designed for a fiber-optic endoscope. Bromwich *et al.*^[121] proposed an adaptor for coupling a traditional endoscope to a videophone for transmitting images collected by the endoscope to a remote observer. Wu *et al.*^[122] recently transformed a smartphone into an endoscope for acquiring otorhinoscopic images from six patients for remote diagnosis. Jongasma *et al.*^[123] developed an otoendoscope system based on a mobile phone, which has been commercialized by Endoscope-i Ltd. MobileOCT has recently marketed a multimodal smartphone imaging system that can simultaneously undertake bright-field, polarization difference, and spectral imaging with applications for cervical cancer detection in developing countries.^[124] The device uses a rigid imaging tube and requires sophisticated imaging optics; thus, its application in LMICs is limited.

1.5 SOLUTION: SMARTPHONE-BASED DUAL-MODALITY FIBER-OPTIC MICROENDOSCOPE

To fulfill the urgent need of practical and efficient approaches for cervical cancer screening in LMICs and reduce the cost of optical endoscopes, we have designed and

developed a portable, cost-effective, and easy-to-use optical microendoscope system, named SmartME and tested its capability of characterizing biological properties *in vivo*. The device consolidates the optical endoscope technologies into a smartphone platform that is capable of performing both fluorescence imaging and diffuse reflectance spectroscopy. This solution takes the advantages of both methods and provides high-resolution imaging and quantitative information about the tissue physiology. We hypothesises that **1**) there are significant differences in the biomarkers (nuclear size and density, hemoglobin concentration, absorption, and scattering) among high- and low-grade lesions and their normal/benign counterparts, and **2**) these contrasts can be detected by the proposed dual modality device.

1.6 OUTLINE OF THEIS

The development procedures of the SmartME device involve instrumentation of smartphone-based FLI and DRS separately and combination of two imaging modules together. In Chapter 2, we described the design and development of a smartphone-based fiber-optic microendoscope for high-resolution fluorescence imaging and present the procedure and results of performance characterization. The design was first simulated and optimized in Zemax OpticStudio to fulfill the high-performance requirements. The imaging system was characterized using a 1951 USAF target to determine its spatial resolution. With the help of fluorescence contrast agent proflavine, high-resolution fluorescence images were successfully taken from biological samples to evaluate its performance. Image processing approaches to remove the fiber bundle artifacts and extract N/C from the fluorescence images were developed.

In Chapter 3, we present the design and development of a smartphone-based spectrometer for diffuse reflectance measurement. The design was also simulated and optimized in Zemax to evaluate its feasibility. The developed DRS system was characterized and calibrated using two calibration lamps. An optical resolution of 2 nm was estimated, which is comparable to a commercially available benchtop spectrometer. Tissue-mimicking phantom experiment was performed to evaluate the accuracy of the system in measuring diffuse reflectance and extracting optical properties based on a fast Monte Carlo model. An averaged error of less than 5% was achieved, which is also as good as a commercial spectrometer that has been extensively verified in clinical studies.

In Chapter 4, we demonstrated the instrumentation of the dual-modality fiber-optic microendoscope SmartME by combining the FLI and DRS together. The SmartME has a spatial resolution of $\sim 3.5 \mu\text{m}$ for FLI and high accuracy in measuring diffuse reflectance in tissue. A smartphone App has also been developed to control the phone camera, collect the images/spectra, and communicate with the remote server. When used with the App, the device can take FLI and DRS measurements on epithelial tissues, wirelessly transfer the data to the server for real-time data processing, and return the results to the SmartME within a minute. Our preliminary studies have demonstrated that the dual-modality SmartME can accurately characterize the biological properties and provide complementary information about epithelial tissues. The SmartME has great potential to provide a compact, cost-effective, and 'smart' solution for early detection of neoplastic changes in epithelial tissues, especially in low resource settings.

Chapter 5 summarizes the achievements and current limitations of the dissertation work and discusses the future work to further improve the SmartME device and fully

investigate the potential of the SmartME for early detection of neoplasia in epithelial tissues in clinical studies.

CHAPTER 2: SMARTPHONE-BASED FLUORESCENCE IMAGING

Portions of this chapter are derived from the following publication:

Hong, X., Nagarajan, V. K., Mugler, D. H., & Yu, B. (2016). Smartphone microendoscopy for high resolution fluorescence imaging. *Journal of Innovative Optical Health Sciences*, 9(05), 1650046.^[108]

In this chapter, we described the design and development of a smartphone-based fiber-optic microendoscope for high-resolution fluorescence imaging and present the procedure and results of performance characterization. The design was first simulated and optimized in Zemax to fulfill the high-performance requirements. The developed system was characterized using a 1951 USAF target to determine its spatial resolution. With the help of fluorescence contrast agent proflavine, high-resolution fluorescence images were successfully taken from biological samples to evaluate the performance of the system. The experiments have demonstrated the potential of developing a compact, easy-to-use and cost-effective smartphone-based microendoscope to improve the screening and early diagnostic rates of many medical conditions in LMIC.

2.1 INTRODUCTION

2.1.1 Fluorescence process

Fluorescence is a form of photoluminescence that occurs in certain molecules called fluorophores. When a fluorophore is irradiated with light at a specific wavelength, it absorbs light energy and enters to an excited state, then immediately retreats and emits light with wavelengths longer than the incident light. This three-stage process is illustrated by the Jablonski diagram^[125] in Figure 2-1.

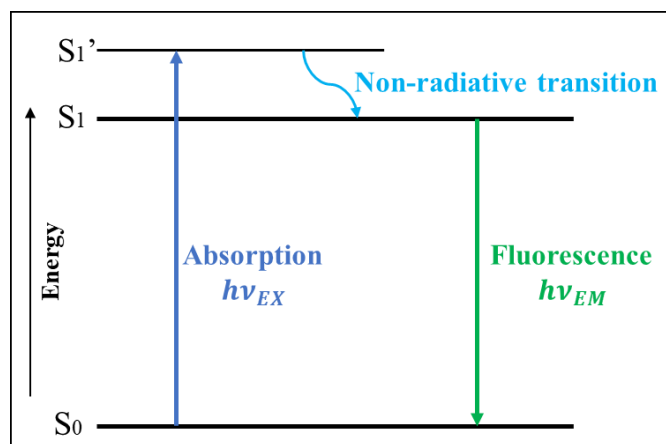


Figure 2-1: Jablonski diagram illustrating the three-stage process of fluorescence

Absorption and excitation: when a fluorescent molecule absorbs the energy of the incident light, the electrons in it are stimulated from the ground state S_0 to the excited state S_1' , so that $S_0 + hv_{EX} = S_1'$, where h is the Planck constant, v_{EX} is the frequency of the incident photon.

Non-radiative transition: Electrons in the excited state can release their energy and transit to the ground state in different ways. In a non-radiative transition process, electrons can transit from the excited state S_1' via a very fast (less than a picosecond) without radiation to a slightly lower excited state S_1 . The energy difference between the two excited states is called the Stokes Shift.

Emission: The excited states are unstable so that electrons at the excited state S_1 will transit back the ground state S_0 . When the electrons are restored to the ground state, the energy is released in the form of light. The light emitted here is fluorescence, and its frequency is v_{EM} , so that $S_1 = S_0 + hv_{EM}$. The energy of the emitted photon is lower than the excitation photon due to energy loss (heat) during the non-radiative transition,

and therefore fluorescence usually has a longer wavelength. The ratio of the total number of photons emitted to the total number of photons absorbed is called quantum yield.

Excitation spectrum and emission spectrum are two important indicators for characterizing fluorescent materials. In general, one fluorophore material can be excited by light at different wavelengths. Their emitting fluorescence can also cover a certain range of wavelengths. The excitation spectrum refers to the relationship between the intensity of the emission and the excitation wavelength. Based on the excitation spectrum, the wavelength range of the excitation light required to illuminate the fluorophores can be determined, and the optimal excitation wavelength at which the intensity of a certain emission is maximum can also be determined. The emission spectrum refers to the intensity and energy distribution of light of different wavelengths emitted by excitation at a specific wavelength. A typical illustration of excitation and emission spectra is presented in Figure 2-2.

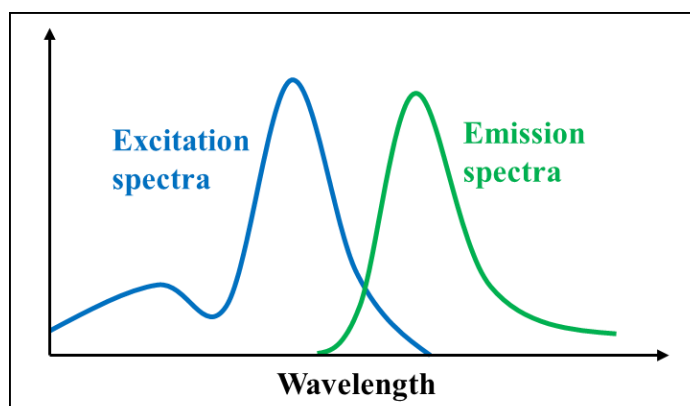


Figure 2-2: Excitation and emission spectra (generic)

2.1.2 Absorption and fluorescence of Proflavine

Proflavine, an acriflavine derivative, was first introduced into clinical use in 1917 for antiseptic applications.^[126] It was typically used as an antiseptic drug that can be topically applied on the skin,^[127] based on its capability to induce a genetic mutation by intercalating the DNA. This preferential cell nuclei staining property has later been shown to provide strong fluorescent contrast, allowing for its applications in endoscopic fluorescence imaging.^[128] The measured absorption peaks of proflavine in the water at PH = 7 are 260 nm around 445 nm^[129-132] and exhibits a fluorescence emission centered at 515 nm, with a quantum yield of 0.34.^[133,134]

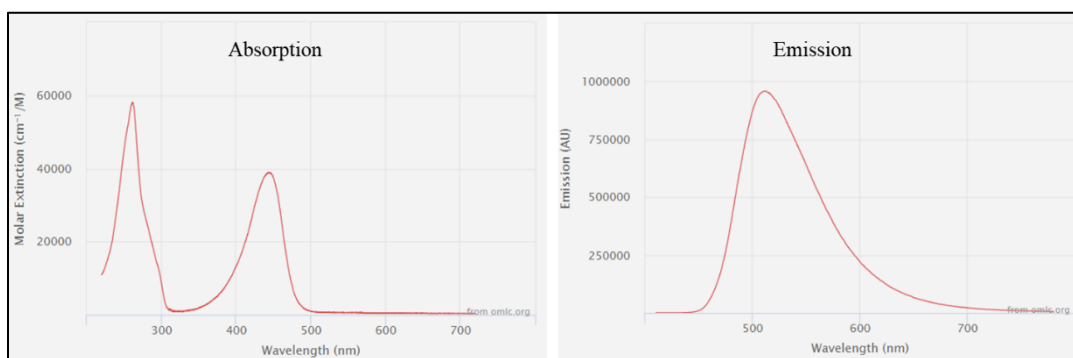


Figure 2-3: The fluorescence excitation and emission spectra of Proflavine in water

(Photo credit: Scott Prah, OMLC. Reference 122)

2.2 OPTICAL DESIGN

2.2.1 System layout

The smartphone-based fiber-optic microendoscope consists of a smartphone with a rear camera, imaging optics which was engineered as an attachment, and a fiber optic imaging bundle. A schematic diagram of the smartphone microendoscope is shown in Figure 2-4. The imaging optics include a band-pass filter for fluorescence excitation

(BP1), a dichroic beamsplitter (DBS), a finite microscope objective (OBJ), a band-pass fluorescence emission filter (BP2), an eyepiece (EP). The filtered excitation light from a blue light emitting diode (LED) propagates through a condenser lens (CL) and be redirected by the beamsplitter towards the objective to achieve a Kohler illumination (uniform illumination) on the proximal end of the fiber bundle plugged into the FC/PC connector. The distal end of the imaging bundle is in contact with the target being tested, such as biological tissue. The fluorescence emissions from the target are collected by the same fiber bundle, propagate through the objective, beamsplitter and emission filter that blocks the excitation lights, and then enter the rear camera of the smartphone after being collimated by the eyepiece.

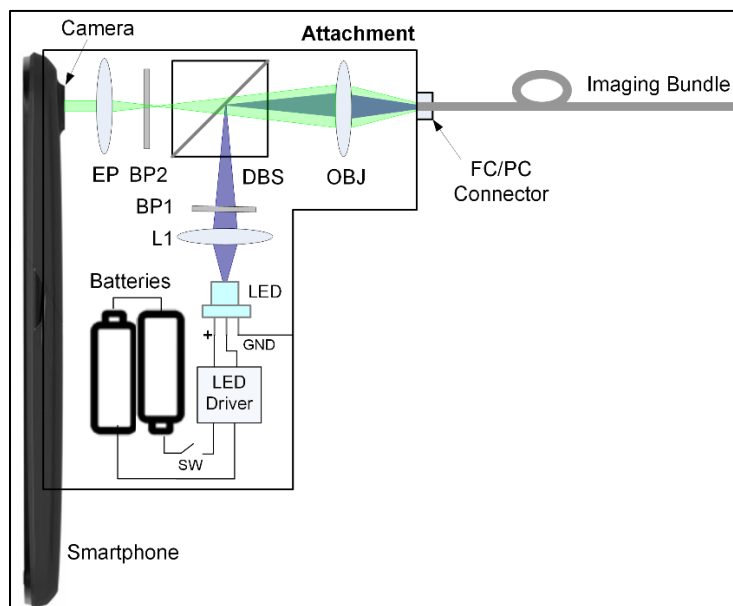


Figure 2-4: Schematic diagram of the smartphone microendoscope for FLI

EP – eyepiece; BP1 and BP2 – optical bandpass filters; DBS - dichroic beamsplitter; OBJ – microscope objective; L1 – condenser lens; LED - light-emitting diode; GND – ground; SW – ON/OFF switch

The use of off-the-shelf optic components in optical system design can provide tremendous advantages in terms of reduced cost and development effort. Hence finding the most appropriate stock optics is critical to the system development. Zemax is a widely used optical design program that offers features and functions for comprehensive analysis, simulation and design. The design follows the system layout shown schematically in Figure 2-4. The blue beam represents the propagation of the blue LED light source. The green beam represents the in-focus fluorescence captured by the phone camera. The fluorescent microendoscope is designed in two major modules:

- **Imaging module:** Microscope objective to the eyepiece lens and cellphone camera.
- **Illumination module:** Light focusing system to the microscope objective to deliver excitation light to the fiber bundle.

2.2.2 Simulation of imaging module

Simulation of the imaging module was to determine the specification of optical lens to be used and the overall size of the design. It starts with sequentially defining each surface/element in the lens data editor (LDE), as shown in Table 2-1. A triplet lens and a doublet lens were used to represent the achromatic objective lens and eyepiece lens, respectively. This method is the easiest way to give enough degrees of freedom for optimization to further overcome aberrations. A 1 mm thick glass plate after the last objective element was added and tilted by 45 degrees about the x-axis to model the decenter introduced by the dichroic beamsplitter in the system, followed by a single surface to represent the emission filter. Note that coating profiles of the dichroic mirror and emission band-pass filter were not pre-defined to simplify the design process because

the introduction of these elements should not affect the imaging quality. A general cellphone camera module was imported and placed at the end of the system to become the last element. The total track length was required to be less than 200 mm. Vary the radii and thicknesses of each surface in the LDE to optimize the imaging quality. Figure 2-5 depicts the design simulation.

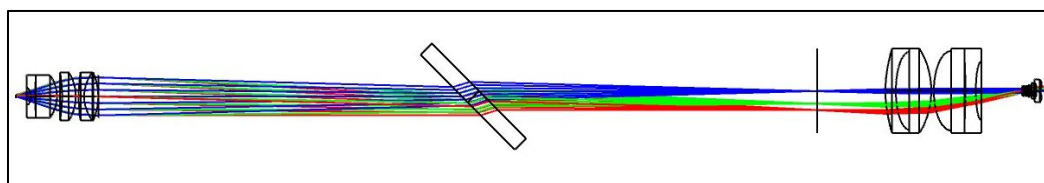


Figure 2-5: Simulation of fluorescence imaging system

Elements from left to right: objective lens, dichroic beamsplitter, emission filter, eyepiece lens, and cellphone camera. The coating profiles of the mirror and filter were not defined in the design.

Table 2-1: Values defined in the LDE for FLI module (optimized)

Surf.	Type	Comment	Radius	Thickness	Material	Coating	Clear Semi-Dia	Chip Zone	Mech Semi-Dia	Conic	TCE x 1E-6
0	OB	Standard	Infinity	2.840			0.300	0.000	0.300	0.0...	0.000
1	(ap)	Standard	-3.416	0.787	F5		4.000 U	0.000	4.000 U	3.3...	-
2	(ap)	Standard	0.463	4.200	SK5		4.000 U	0.000	4.000 U	-38...	-
3	(ap)	Standard	-7.115	0.993			4.000 U	0.000	4.000 U	0.6...	0.000
4	(ap)	Standard	-24.601	2.600	SK5		4.572 U	0.000	4.572 U	-17...	-
5	(ap)	Standard	-8.843	0.565			4.572 U	0.000	4.572 U	0.6...	0.000
6	(ap)	Standard	28.178	1.041	SF1		4.572 U	0.000	4.572 U	-3...	-
7	(ap)	Standard	6.978	2.700	K10		4.572 U	0.000	4.572 U	-0...	-
8	(ap)	Standard	-10.402	0.000			4.572 U	0.000	4.572 U	-1...	0.000
9	STC	Standard	Infinity	70.495			4.000 U	0.000	4.000	0.0...	0.000
10	(ap)	Standard	BS	Infinity	3.000	N-BK7	12.700 U	0.000	12.700	0.0...	-
11	(ap)	Standard	Infinity	64.554			12.700 U	0.000	12.700	0.0...	0.000
12		Standard	Infinity	13.000	P		8.000 U	0.000	8.000	0.0...	0.000
13	(ap)	Standard	21.782	2.000	SF11		8.000 U	0.000	8.000 U	-6...	-
14	(ap)	Standard	20.940	6.750	BK7		8.000 U	0.000	8.000 U	7.1...	-
15	(ap)	Standard	-15.891	0.500			8.000 U	0.000	8.000 U	0.6...	0.000
16	(ap)	Standard	17.221	6.000	BK7		8.000 U	0.000	8.000 U	4.2...	-
17	(ap)	Standard	-190.534	2.000	SF11		8.000 U	0.000	8.000 U	111...	-
18	(ap)	Standard	29.936	8.682	C		8.000 U	0.000	8.000 U	28...	0.000
19	(ap)	Even Asphere	1.714	0.617	COC		0.917 U	0.000	0.941 U	-1...	-
20	(ap)	Even Asphere	-7.181	0.023			0.941 U	0.000	0.941	0.0...	0.000
21	(ap)	Even Asphere	7.867	0.280	AL-62...		0.939 U	0.000	0.939	0.0...	-
22	(ap)	Even Asphere	1.864	0.377			0.908 U	0.000	0.939	-0...	0.000
23	(ap)	Even Asphere	6.208	0.436	COC		1.009 U	0.000	1.115 U	0.0...	-
24	(ap)	Even Asphere	7.014	0.278			1.115 U	0.000	1.115	-89...	0.000
25	(ap)	Even Asphere	6.053	0.550	COC		1.222 U	0.000	1.452 U	-21...	-
26	(ap)	Even Asphere	50.000	0.263			1.452 U	0.000	1.452	0.0...	0.000
27	(ap)	Even Asphere	2.227	0.840	COC		1.493 U	0.000	2.146 U	0.0...	-
28	(ap)	Even Asphere	1.456	1.101	V		2.146 U	0.000	2.146	-3...	0.000
29	IM.	Standard	Infinity	-			0.975	0.000	0.975	0.0...	0.000

In an optical system design, aberrations take place when light from one point of an object diverge from a single point after traveling through the system. An optical designer must correct the aberrations because they cause the image formed by the system to be blurred or distorted. The most common types of optical aberrations include spherical aberration, astigmatism, chromatic aberration, defocus, coma, and Petzval field curvature. The image simulation feature of Zemax simulates the image formed by the optical system when a 2D picture is imaged through it. It is ideal for characterizing the real performance of an optical system. A built-in full-color bitmap, as shown in Figure 2-6(left), was used to simulate the imaging quality of the FLI system. Due to optical aberrations, the blurry image in the middle was generated by the FLI system before optimization. Details of the picture, especially the tiny objects such as the leaves and the human figures, became indistinguishable. Furthermore, although the achromatic objectives are corrected for axial chromatic aberration and spherical aberration in color, it will still result in uneven distribution of light from the center to the edge of the field-of-view. Correction for flatness of field is required for a better performance. In addition to the imaging quality, a proper magnification was required so that the images occupy the most area of the camera sensor. Based on the camera specification of Moto G (1st Gen), the optimized simulation suggested that using a 20X plan achromatic objective (AmScope PA20X-B) with a wide-field 16X eyepiece (AmScope EP16X23-S) would provide required imaging performance and in the meantime most of the sensor area would be used. The objective has a numeric aperture of 0.40 (larger than the NA of the imaging bundle 0.39) and standardized tube length of 160 mm.

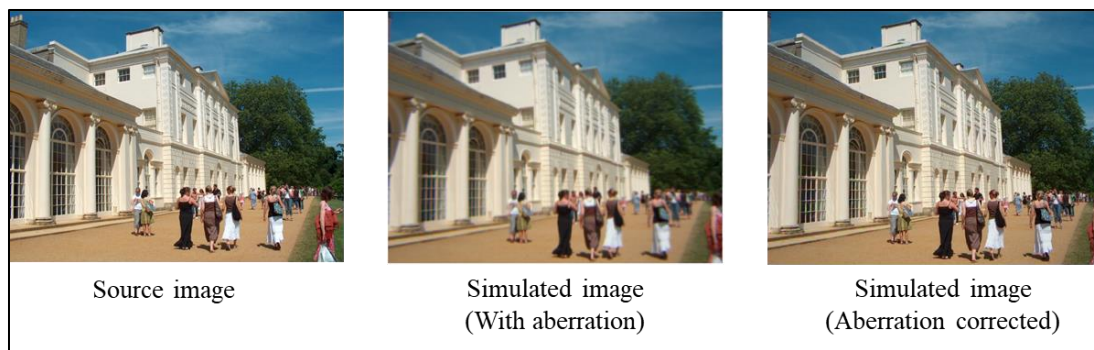


Figure 2-6: Simulation of imaging quality

2.2.3 Simulation of illumination module

The selection of the light source, excitation filter, dichroic beamsplitter and emission filter is based on the use of the fluorescence dye. Therefore, the purpose of the illumination simulation was to simulate how much light power could be obtained out of the fiber image bundle by using the selected optical components when combining the illumination and imaging modules. In this study, a blue LED (455 nm, M455L3, Thorlabs), excitation filter (FF01-452/45, Semrock), dichroic beamsplitter (475 nm cutoff, 475DCXRU, Chroma Technology), and emission filter (FF01-550/88, Semrock) were used based on the use of proflavine (Sigma-Aldrich P2508), a topically applied DNA dye, as the fluorescence contrast agent. The peak excitation and emission wavelength of proflavine are 445 nm and 515 nm, respectively. The fiber bundle (FIGH-30-650S, Fujikura) has an imaging area of 600 μm and consists of $\sim 30,000$ individual fibers of $\sim 3 \mu\text{m}$ in diameter with a center-to-center distance about 3.3 μm . The single core has a numerical aperture (NA) of approximately 0.39.

Table 2-2: Non-sequential component editor including illumination module

Object Type	Comment	Ref Object	Inside Of	X Position	Y Position	Z Position	Tilt About X	Tilt About Y	Tilt About Z	Material
1 Source File	rayfile_LD...	0	0	0.000	-35.630	56.000	-90.000	0.000	0.000	-
2 CAD Part: STEP/IGES	LD_CQ7P...	0	0	0.000	-35.630	56.000	-90.000	0.000	0.000	ABS...
3 Annular Aspheric Lens		2	0	0.000	0.000	16.189	0.000	0.000	0.000	B270
4 Standard Lens		0	0	0.000	90.638	56.000	45.000	0.000	0.000	N-BK7
5 Standard Lens		0	0	0.000	90.638 P	137.000	0.000	0.000	0.000	K10
6 Standard Lens		5	0	0.000	0.000	2.700	0.000	0.000	0.000	SF1
7 Standard Lens		6	0	0.000	0.000	1.606	0.000	0.000	0.000	SK5
8 Standard Lens		7	0	0.000	0.000	3.593	0.000	0.000	0.000	SK5
9 Standard Lens		8	0	0.000	0.000	4.200	0.000	0.000	0.000	F5
10 Standard Surface		9	0	0.000	0.000	3.627	0.000	0.000	0.000	
11 Annular Volume		10	0	0.000	0.000	0.000	0.000	0.000	0.000	ABS...
12 Detector Surface		11	0	0.000	0.000	10.000	0.000	0.000	0.000	
13 Standard Lens		9	0	0.000	0.000	-177.4...	0.000	0.000	0.000	SF11
14 Standard Lens		13	0	0.000	0.000	2.000	0.000	0.000	0.000	BK7
15 Standard Lens		14	0	0.000	0.000	6.500	0.000	0.000	0.000	BK7
16 Standard Lens		15	0	0.000	0.000	6.750	0.000	0.000	0.000	SF11
17 Standard Lens		4	0	0.000	-25.400	25.400	45.000	0.000	0.000	BK7
18 Standard Lens		16	0	0.000	0.000	45.000	0.000	0.000	0.000	BK7
19 Annular Volume		1	0	0.000	0.000	10.000	0.000	0.000	0.000	ABS...

Both sequential ray tracing and non-sequential ray tracing are available in Zemax. In the sequential mode, all of the rays traced must propagate through the same predefined set of surfaces in the same order. By contrast, rays in non-sequential mode can propagate through the optical components in any order and can hit the same object multiple times. The simulation of the illumination was first done in sequential mode. The illumination ray profile of LED is provided by Thorlabs so that it can directly be loaded to the design. Surfaces of the condenser lens were created with preliminary radii of the lens surfaces for further optimization. The illumination module was then combined with the imaging lens system and converted into the non-sequential mode. In the Non-Sequential Component editor shown in Table 2-2, a detector surface (Object 12) was created on the plane of the proximal end of the fiber bundle so that the light power detected on this surface would be treated as the power coupled into the fiber bundle, given that the numerical apertures of the objective lens and the fiber bundle were matched.

The surface of the dichroic beamsplitter and fluorescence filters were coated in this modeling to simulate the real situation. A coating file of the front surface of the dichroic was added so that it would reflect 445 nm and passes 515 nm. Coating files of the excitation filter and emission filter were also defined accordingly. The light power detected on the detector surface was 1.276 mW, which was approved to be very close to the value we measured from the experimental setup.

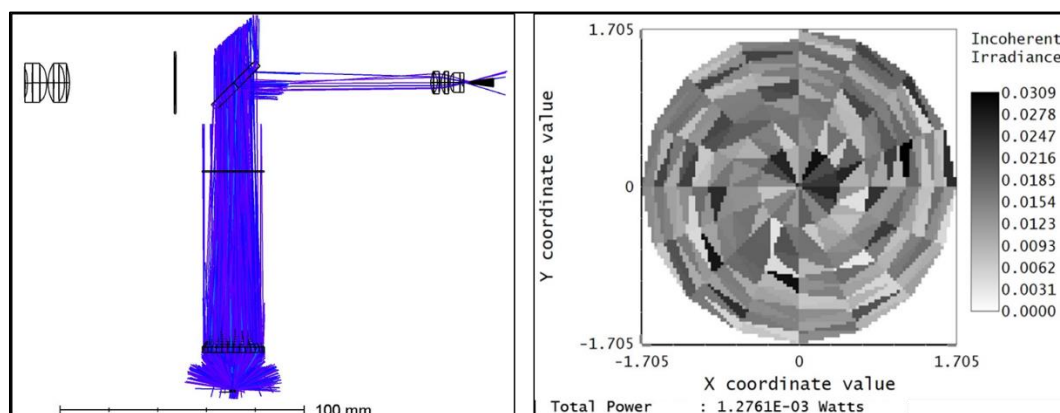


Figure 2-7: Simulation of fiber bundle light coupling

Left: Illumination simulation using the ray profile provided by the manufacturer. **Right:** detector image on a surface placed on the proximal end of the fiber bundle. The detected power was 1.28 mW

2.2.4 System assembly

In addition to the components that have been determined by simulation results and based on the use of fluorescence dye. Optomechanical components were used to fix the position of the optical components and ensure a good alignment. Figure 2-8 illustrates the assembly of the FLI system. All the components are shown at their relative locations. It is important to note that proper orientation of the filters is helpful to maximize performance and minimize autofluorescence. Most mounted filters have an arrow located on the edge of the filter to aid orientation. The dichroic beamsplitter (9) should be mounted with the

coated surface toward the light source (13), excitation filter (11), and the objective lens (4). The excitation filter (11) should be placed with the arrow pointing toward the cage cube (7), and away from the blue LED (13) light source. The emission filter (10) should be positioned with the arrow pointing toward the objective lens (4) and away from the camera (16).

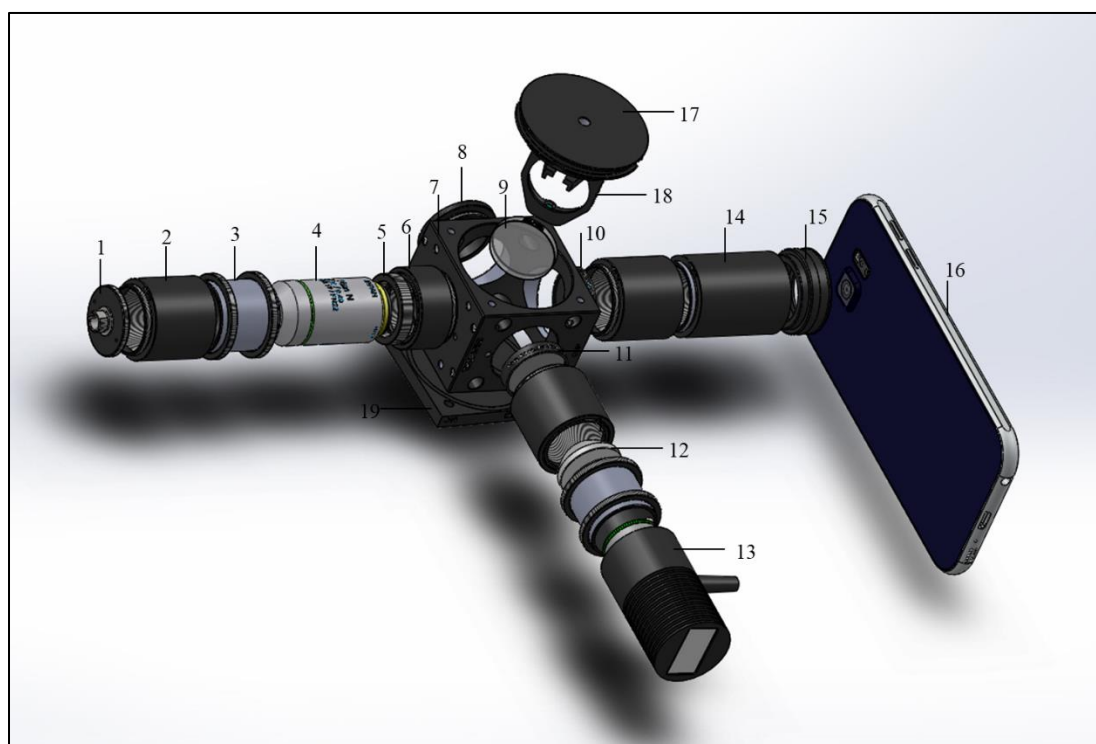


Figure 2-8: Exploded view of all components for FLI

Exploded view showing the relative locations of (1) FC/PC adapter, (2) 1" Long lens tubes, (3) 1" Long lens tube coupler, (4) 20× objective lens, (5) RMS adapter, (6) 0.5" Long lens tube, (7) 30 mm cage cube, (8) end cap, (9) dichroic beamsplitter, (10) emission filter, (11) excitation filter, (12) condenser lens, (13) 455 nm blue LED, (14) 2" Long lens tube, (15) 16× eyepiece lens, (16) Samsung Galaxy S6 cellphone, (17) cage cube platform, (18) optic mount, and (19) blank cover plate.

The most challenging step of the assembly procedure is to properly align the LED (13), dichroic beamsplitter (9) and objective lens focus to deliver maximum power to the

fiber bundle when it connects to the FC/PC adapter (1), while the fiber bundle remains in focus. This alignment can be completed in three steps.

First, attach the fiber bundle to the FC/PC receptor (1), adjust the distance between the FC/PC adapter (1) and objective lens (4) by rotating the lens tube coupler (3) so that a clear and sharp image of the fiber bundle can be captured using the camera. The position of the FC/PC adapter (1) is now optimized, and it should be locked using the lock ring on the lens tube coupler (3). The imaging focus is fixed on the proximal end of the fiber bundle after this step unless the distance between an objective lens and eyepiece lens is altered.

Second, point the distal end of the fiber bundle to a light power meter, adjust the position of the LED (13) to maximize the light intensity exiting the distal end of the fiber bundle. The position of the LED (13) is optimized when the highest power is achieved. Secure the LED (13) in this position using the lock ring on the lens tube coupler.

Third, after completion of the device assembling, slightly rotate/adjust the cage platform with the dichroic beamsplitter mounted on it and measure the power coming out of the fiber. The highest power is achieved when the dichroic beamsplitter is optimally aligned and it should be firmly secured at this location.

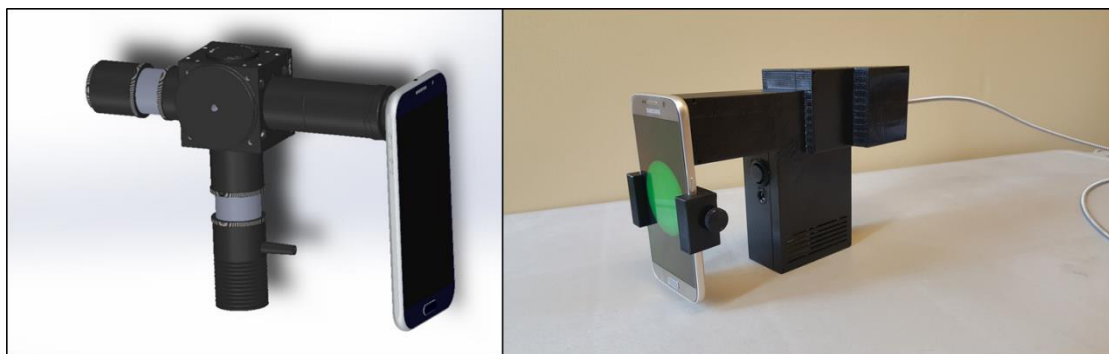


Figure 2-9: The completed smartphone FLI system

Left: the completed FLI system with major optic components. **Right:** picture of the completed FLI system with a 3D-printed enclosure, and the fiber bundle attached.

2.3 PERFORMANCE CHARACTERIZATION

2.3.1 Imaging a uniform fluorescence reference slide

In the prototype shown in Figure 2-9, a 20× plan objective and a 16× wide-field eyepiece were selected in combination with the cellphone camera lens to obtain a proper magnification. The actual imaging area filled 1730 pixels in diameter of the camera sensor array, which represents an image size of $1730 \times 1.4 \mu\text{m} \approx 2.4 \text{ mm}$ in diameter, resulting in 4× magnification (2.4 mm/0.6 mm). Therefore, each fiber occupied ~36 pixels of a raw image. The locations of the proximal end of the fiber bundle and the condenser lens were adjusted so that all pixels in the bundle were uniformly illuminated and clearly imaged onto the camera.

A green fluorescence reference slide (2273-G, Ted Pella) was used to check the uniformity of the system. Figure 2-10 shows a representative image of the proximal end of the fiber bundle when its distal end was in contact with the reference slide. A close look of the image marked by the red box in Figure 2-10 indicates that individual fibers of the bundle were well resolved.

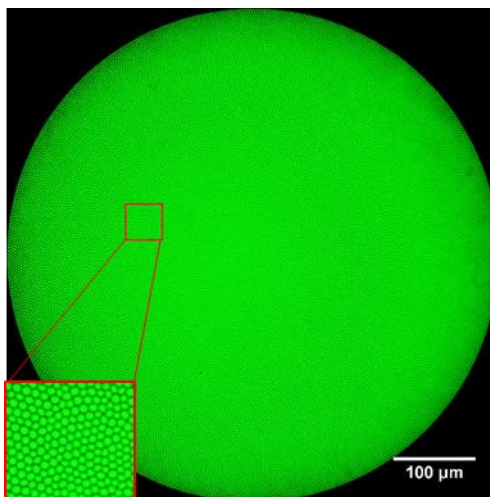


Figure 2-10: Fluorescence image of a uniform fluorescence reference slide

2.3.2 Fiber bundle pixelation artifact removal

While the fiber bundle brings the flexibility of the endoscopic imaging system, its honeycomb pattern artifact also brings inherent noise to the image. A variety of methods for removing the fiber bundle pixelation have been proposed. Generally, the processing methods can be classified into two groups, of which one is filtering and smoothing, and the other is interpolation reconstruction. Göbel *et al.* smoothed the image using Gaussian filtering on images obtained in a two-photon endoscope system.^[135] However, the filtering method actually blurs the image, deteriorates the contrast of the image. Winter *et al.* proposed using different types of adaptive filters in the frequency domain to process the image^[136] Similarly, Suter *et al.* used a low-pass filter to process the image in the frequency domain, filtering out the high-frequency components and retaining only the low-frequency information in the image.^[137] However, choosing the right filter would become much more complicated if the images contain more complex frequency components. Han *et al.* proposed a method that histogram equalization was first applied before Gaussian filtering.^[138] This method improved the imaging quality and minimized

the loss of details when the fiber bundle artifact was removed. Elter *et al.* proposed a method of interpolation reconstruction.^[139] The center of each fiber was obtained first, and the pixel values at these locations were used to reconstruct the original image by interpolation.

Since the intensity within each fiber has a Gaussian distribution, the intensity at the center of each fiber represents the fluorescence intensity collected by that fiber. In this work, we employed the interpolation reconstruction method to eliminate the fiber pattern artifacts in the fiber bundle imaging. Figure 2-11 illustrates the steps to do intensity correction and image reconstruction.

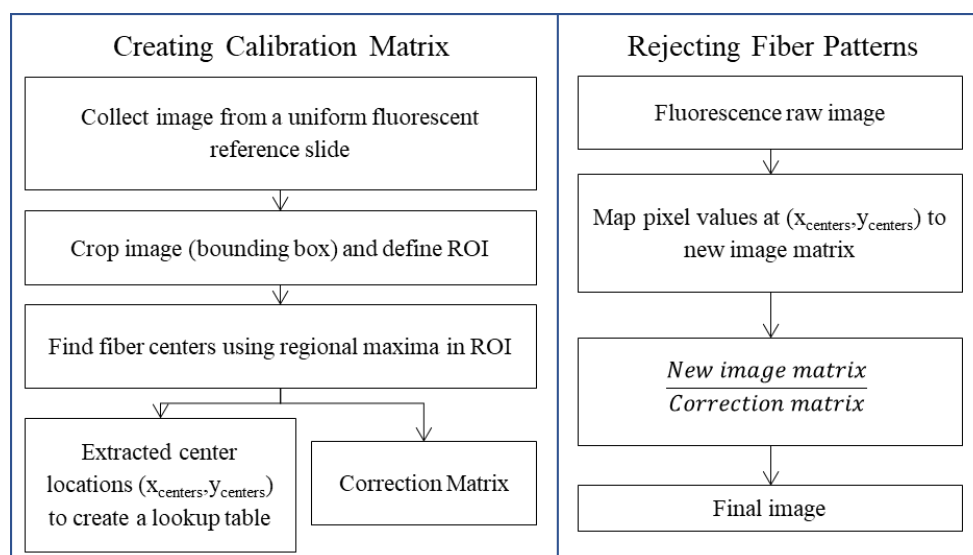


Figure 2-11: Flowcharts for image calibration and fiber pattern removal

First, the image measured from the uniform fluorescent reference slide is used to calibrate the illumination distribution of the fluorescence images. The imaging area of the fiber bundle was defined as the region of interest (ROI) and circularly cropped out of the image. The regional maxima (fibers) within the defined ROI were extracted using a built-

in Matlab function ‘imregionalmax’. The function returns a binary image consisting of 1s at regional maxima and 0s elsewhere. Consequently, the location of fiber centers was given by the coordinates of 1s in the binary image. A lookup table consisting of the fiber center locations was created. Pixel values at these locations in the calibration image were extracted to form a correction matrix. Next, pixel values of a raw fluorescence image at locations that correspond to those in the lookup table were extracted to create a new image, which was divided by the correction matrix using an element-by-element operation to correct for the intensity fluctuation within each fiber. Next, the image was converted to a gray-scale intensity image. The final step was to assign the extracted center pixel values to the neighboring pixels to reconstruct a comb structure free image.

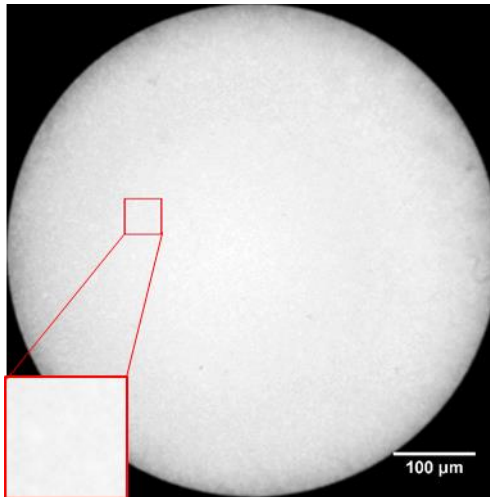


Figure 2-12: Fiber pattern removed image of the uniform fluorescence reference slide

It is important to note that the built-in Matlab function ‘imregionalmax’ can only process images with regional peaks that have maximum connectivity of 26 or less, the raw images with a fiber occupying 36 pixels (on the camera sensor) was scaled to half of its original size. Given that the resolution of the imaging bundle is limited by the center-to-center distance of two adjacent fibers, reducing the image size to half doesn’t change

the spatial resolution of the system. The fiber pattern rejected image of Figure 2-12. The pixelation artifacts were effectively removed in the reconstructed image.

2.3.3 Spatial resolution characterization

To characterize the spatial resolution of the smartphone microendoscope, fluorescence images were taken from a 1951 USAF resolution test target that was placed on top of a green fluorescent reference slide. Figure 2-13(a) and (b) demonstrate the raw and fiber pattern rejected images of the test target, respectively. The intensity function across the lines (not shown) indicates that the valley intensity between the Group 7 Element 2 lines is 3dB below the peak value, while less than 3dB for that of the Group 7 Element 3 lines. This demonstrates that the microendoscope successfully resolved the adjacent lines of Element 2 in Group 7, as can also be visually seen from the enlarged area in Figure 2-13(b). Thus, the spatial resolution was estimated to be about 3.3 μm . This value meets our expectation that the resolution of the setup is limited by the center-to-center distance between two adjacent fibers of the imaging bundle, which is about ~ 3.5 μm .

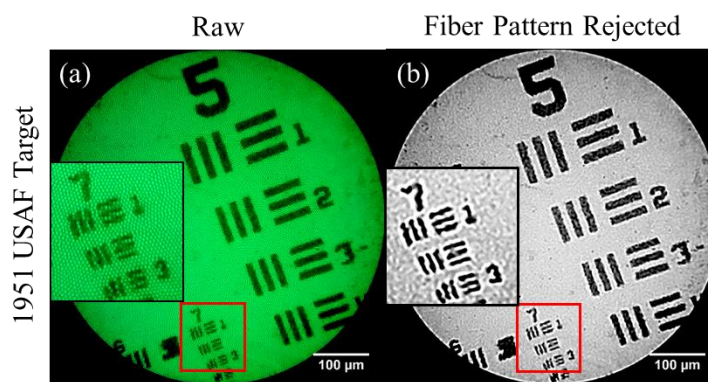


Figure 2-13: Fluorescence images taken from a 1951 USAF resolution target

(a) raw image; (b) fiber patter removed image

2.3.4 Fluorescence imaging of biological samples

Ex vivo porcine adipose and bovine skeletal muscle tissues were also imaged using the prototype FLI microendoscope. Fresh porcine and bovine tissues were obtained from a local butcher's shop within 3 hours of the slaughter of the animals. Experiments were conducted immediately after the tissues were transported to the lab in a cooler. The tissues were sliced into a dimension of 2×2×1 cm (W×D×H). Proflavine at a concentration of 0.01% wt/vol was applied on the surface of the sliced tissues using a cotton swab, and fluorescence images were taken immediately after in a dark room. Typical images are presented in Figure 2-14. The white lipid cells and muscle fascicles are both clearly visible. The brighter backgrounds between the cells of the adipose samples are likely due to the non-specific binding of excessive proflavine on the tissue, which may be reduced by rinsing the sample before imaging.

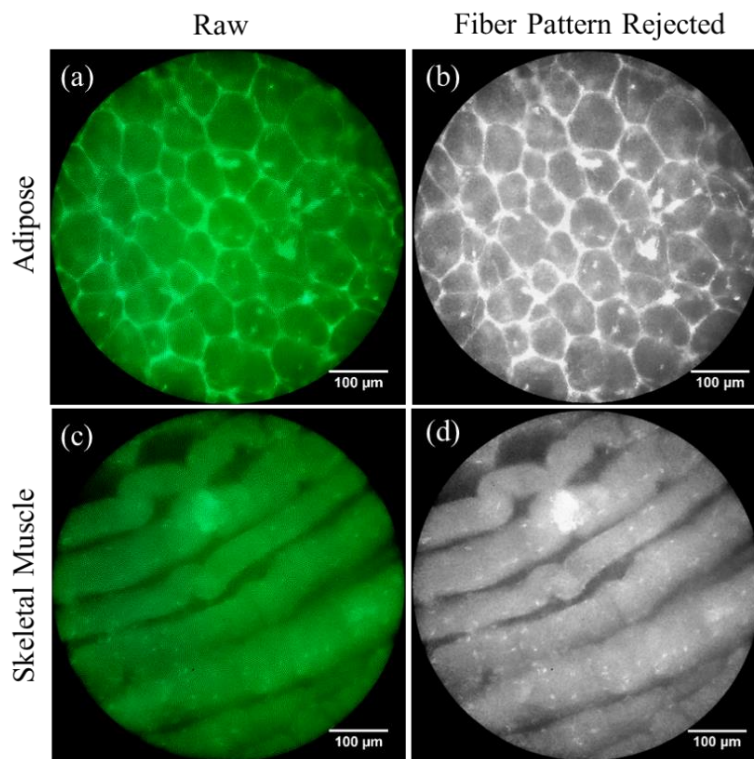


Figure 2-14: Fluorescence images of *ex vivo* tissue

Raw and fiber pattern removed image of *ex vivo* porcine adipose tissue (a, b) and bovine skeletal muscles (c, d).

To test the feasibility of the microendoscope for imaging living cells, both cell lines and oral mucosa from a volunteer (IRB review exempted) were imaged. Images were taken immediately after proflavine (0.01% wt/vol in PBS) was applied on the surfaces of the cells or oral mucosa. The experiment setup and procedures to take images from a single layer of L929 cells in a disk were the same as that used for the *ex vivo* tissues. To image the oral mucosa, the fiber bundle was handheld and brought in gentle contact with the inner cheek of the volunteer. Figure 2-15(a) and (b) show the raw and fiber pattern rejected fluorescence images collected from the L929 cells. The cells can be easily identified with little overlap. It is important to note that the bright spots in the images represent the nuclei instead of the cells because proflavine selectively labels the

cell DNA. Figure 2-15(d) and (e) show the raw and fiber pattern rejected images collected from the oral mucosa. The nuclei of the mucosal cells can be clearly visualized with some background fluorescence, which is attributed to the underlying cells and tissue scattering.

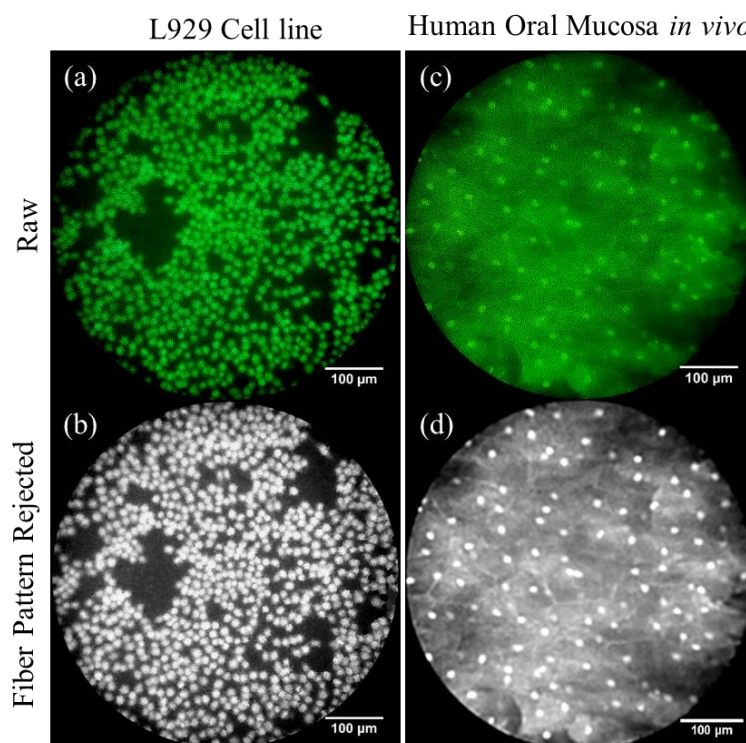


Figure 2-15: Fluorescence images of *ex vivo* cell line and *in vivo* oral mucosa tissue

(a) Raw and (b) processed fluorescence images of a single layer of L929 cells. (c) Raw and (d) processed images of normal human oral mucosa *in vivo*.

2.3.5 Quantitative information: nuclear-cytoplasmic ratio

The images were further processed to extract quantitative information about the samples, such as cell density for cell lines and nuclear-cytoplasmic ratio (N/C) for tissues. The mean projected nuclear area of normal cervical cell is $\sim 36.2 \mu\text{m}^2$ which occupies at least four pixels/fibers of the imaging bundle, while the average nuclear area

of carcinomatous cell is $81.28 \mu\text{m}^2$.^[140] As we mentioned earlier, other studies reported that the LSIL cells have expanded nuclei that are at least three times (in area) as big as the normal nuclei, and HSIL cells have similar expanded nuclei with reduced cytoplasm.^[13] Therefore, although the spatial resolution of the device limits its capability to separate two cell nuclei that are less than $3.5 \mu\text{m}$ apart, the increased size/area of the cell nuclei can readily be detected. Quinn *et al.*^[53] demonstrated that the use of N/C measured from 26 patients in Botswana has achieved a sensitivity of 86% and specificity of 87% in differentiating CIN2+ lesions from non-neoplastic cervical tissues. A median filter was used to reduce the outliers and bring out the core of the bright fluorescent dots. Then the images were inverted to emphasize the dots. Finally, an 'unsharp mask' with a radius of 5 made the images even sharper, as shown in Figure 2-16(a) and (b). From Figure 2-16(a), it was determined, using a particle analysis function of ImageJ, that there was a total of 852 cells within the ROI. Thus, the cell density was $2973 \text{ cells}/\text{mm}^2$, which is very close to the number estimated from a phase contrast microscope image ($\sim 3100 \text{ cells}/\text{mm}^2$). The N/C of the oral mucosa was calculated to be 3.5%.

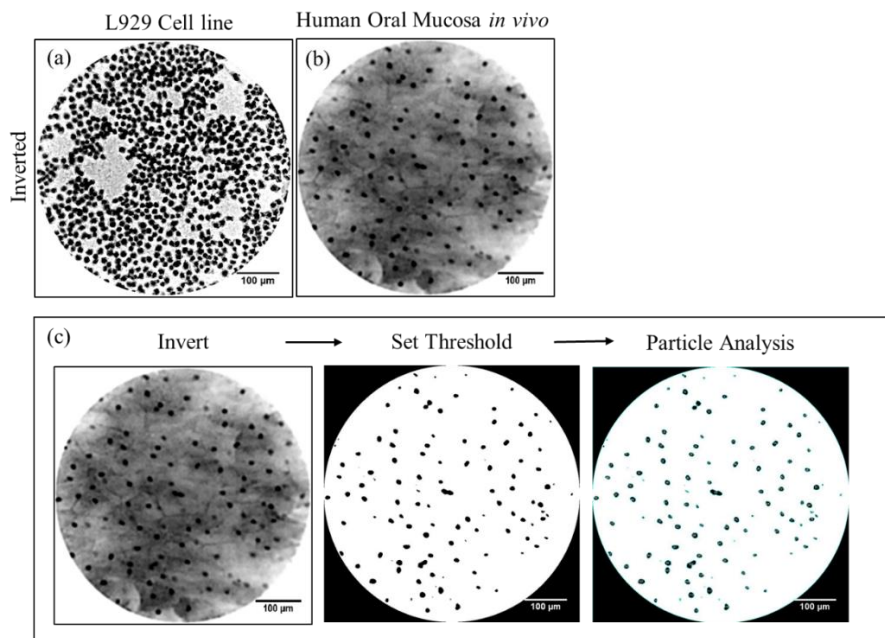


Figure 2-16: Inverted images for N/C extraction

Inverted image of (a) cell line, and (b) oral mucosa tissue. (c) N/C extraction procedures

2.4 DISCUSSION

The results obtained with the prototype smartphone FLI system demonstrate the feasibility of using the smartphone microendoscope for high-resolution fluorescence images. We have constructed a benchtop HRME system, as shown in Figure 2-17(left, top), based on the technology developed by Pierce *et al.*^[72] The system consists of a 1.4 megapixel monochromatic CCD camera with a pixel size of 6.45 μm (Point Grey Research, Inc., Canada), a blue LED, a Dichroic mirror, a 10× infinite corrected objective lens, excitation and emission filters, a fiber-optic imaging bundle, and a laptop computer loaded with custom software for image processing. Figure 2-17(right, top row) shows the images taken with the HRME system from a 1951 USAF resolution test target, *ex vivo* adipose and skeletal muscle of bovine tissues, and oral mucosa of a healthy volunteer, respectively. Proflavine at the concentration of 0.01% wt/vol (in PBS) was applied on the

surfaces of the tissue samples prior to imaging. The tissue images clearly show cell nuclei and tissue structures. Given that the pixel size of smartphones is much smaller than that of the CCD camera in the HRME, high excitation and better imaging optics may be required to obtain fluorescence images of similar quality. Fluorescence images taken using the smartphone-based FLI device were presented in Figure 2-17(bottom). The image quality is comparable to that achieved with the high-resolution microendoscopes (HRME) based on a scientific camera or a DSLR camera^[74].

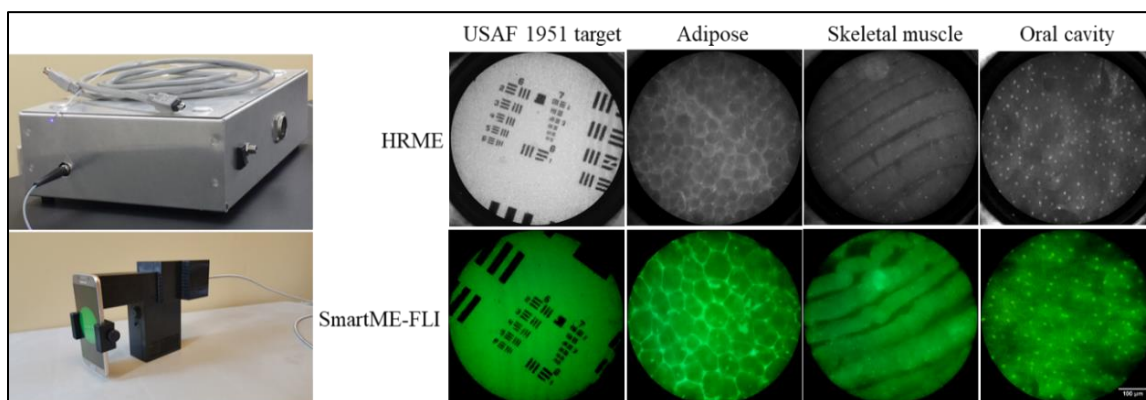


Figure 2-17: Compare between smartphone-based FLI system with HRME

Left: photographs of the benchtop HRME system and our smartphone-based FLI system. **Right:** images taken from a 1951 USAF resolution target, *ex vivo* adipose and skeletal muscle tissues, healthy oral mucosa from volunteers, and using the HRME system (top) and a Samsung smartphone (bottom). The images in each column are not from the same sample.

However, the smartphone microendoscope has several advantages over the HRME and DSLR camera systems. First, scientific or DSLR cameras cost over \$1,000 and very few people own one. Smartphones, especially low-end or used smartphones, are widely available at low cost (<\$100) even in rural areas in LMIC. In particular, being able to use customers' existing smartphones for imaging significantly increases the adoption of the technology in resource-poor settings. Second, the HRME uses a local computer to collect or download images and often requires a trained engineer on site to

operate the system. The smartphone microendoscope does not need a local computer and the application software can be made easy to use, thus further reduces the cost associated with each use of the device in LMIC. More importantly, due to the convenient Internet access through a mobile data plan that is more widely available than a Wi-Fi network, a smartphone microendoscope is more likely to be used as a point-of-care device for telemedicine applications. Finally, our prototype system with a 3D printed enclosure measures about 20×15×5 cm (L×W×H) and weighs only 612 grams. 3D printing of the whole attachment (except the optical components, e.g., LED, lenses, and filters) will make the device even more compact and portable. The final version of the smartphone microendoscope can be readily engineered to a handheld device.

The total cost of the current smartphone microendoscope apparatus is about \$2,000. The primary costs include the imaging fiber bundle (\$1,000 for two meters), optical components (~\$1000). We expect that the cost for a future prototype will be reduced to \$1,000 by batch ordering of the imaging bundle and optical parts as well as using 3D printing technique for the mounting components and enclosure. The final version of the microendoscope for LMIC will include an App (for Android) that is capable of processing the images on the smartphone or sending them to a remote server for processing and receiving the diagnosis.

The biggest challenges in implementing the smartphone microendoscope are: (1) the much smaller sensor pixel size of a smartphone camera than that used in the HRME systems and (2) the unchangeable built-in lens kit. Due to the low throughput of the imaging bundle, it is critical to optimize the efficiency of the imaging optics so that a comparable signal-to-noise ratio can still be achieved with the smaller pixels of the

smartphone cameras. An eyepiece has also been used with the objective lens to correctly image the fiber bundle on to the smartphone camera through the built-in lens kit.

Although the microendoscope described in this report was specifically designed for proflavine as the contrast agent, it can be readily modified for other fluorescence dyes by selecting a LED wavelength and filters that match the excitation/emission spectra of the stain. Almost all smartphone cameras in the market use CMOS sensors, which are sensitive to fluorescence in the visible and near-infrared wavelength range.

The high-resolution smartphone microendoscope allows imaging of subcellular organelles, such as cell nuclei of the mucosa of the cervix, from which the nuclear-cytoplasmic ratio can be determined. The technology can also be readily adapted for imaging suspicious tissues in other internal organ sites, including the GI tracts (colon, liver, esophagus, bladder, pancreas and stomach), prostate, lung, ovarian and oral cavity.

CHAPTER 3: SMARTPHONE DIFFUSE REFLECTANCE SPECTROSCOPY

In this chapter, we described the design and development of a smartphone-based spectrometer for diffuse reflectance measurement. The design was first simulated and optimized in Zemax to evaluate the feasibility. The developed DRS system was characterized and calibrated using two calibration lamps. An optical resolution of 2 nm was estimated, which is comparable to a commercially available benchtop spectrometer (>\$5000). Phantom validation was performed to evaluate the accuracy of the system in measuring diffuse reflectance and extracting optical properties based on Monte Carlo simulation. An averaged error of less than 5% was achieved, which is also as good as a commercial spectrometer that has been extensively verified in clinical studies. Therefore, the smartphone-DRS system has a great potential to provide a cost-effective solution in measuring tissue optical properties and is ready to be combined with other techniques such as FLI to obtain complementary tissue information.

3.1 DIFFUSE REFLECTANCE SPECTROSCOPY

Imaging and spectroscopy are two major groups of optical techniques that are used for biomedical applications. Imaging techniques, such as fluorescence imaging discussed in chapter 2, provide qualitative information by visualizing the morphological structure of the tissue. On the contrary, spectroscopic techniques are able to provide quantitative information of the biochemical or functional properties of the tissue by studying the light-tissue interactions such as absorption and scattering.^[141]

3.1.1 Diffuse reflectance

The phenomenon in which the light emitted into a sample scatters multiple times and eventually comes out is called light diffusion. As illustrated in Figure 3-1, photons that propagate in the tissue will undergo scattering and absorption. Some of the photons are absorbed by specific molecules such as hemoglobin and nucleic acids. Others are scattered multiple times by scatters in the tissue such as mitochondria and cell nuclei, and escape from the tissue in random directions. Diffuse transmission occurs when the emitted light passes through the sample and comes out on the other side. On the other hand, diffuse reflection happens when the outgoing light and the incident light are on the same side. Both the diffuse transmission and diffuse reflections light carry the internal information of the sample, and thus can be collected and analyzed to determine the intrinsic properties of the sample. However, because visible light can only travel for a limited distance in turbid media, the diffuse transmission is less feasible for most applications.

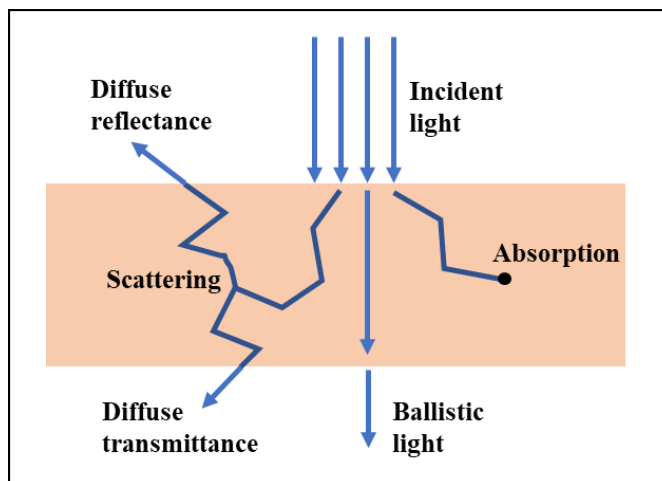


Figure 3-1: Schematic representation of light-tissue interaction

3.1.2 Tissue optical properties

Absorption coefficient μ_a . For the visible light, light absorption in tissue is mainly caused by molecules like hemoglobin, melanin and other pigments. The absorption of light can be described by the absorption coefficient (μ_a), which represents the light extinction due to absorption. The absorption coefficient is wavelength dependent, and it is largely affected by the blood content and oxidation state. Figure 3-2 shows the absorption spectra of oxyhemoglobin (HbO₂) and deoxy-hemoglobin (Hb).^[142] It can be seen that HbO₂ and Hb have very different absorption characteristics across the whole wavelength range, especially at a wavelength longer than 600 nm. The absorption coefficient of most biological tissues is within the range of 0.1 to 10 cm⁻¹.^[143]

Scattering coefficient μ_s . The scattering of light in turbid media is usually characterized using the scattering coefficient (μ_s), which is similar to the absorption coefficient that indicates the light energy loss due to scattering. The uneven refractive index of tissue causes scattering and it depends on the size, density and morphological structure of the tissue contents such as collagen fibers, mitochondria, lipid membrane and nuclei. For example, the water-like lipid membrane interface surrounding each cell and inside a cell has a different refractive index from the gel-like fibrils in the intercellular substance. When both the absorption coefficient and scattering coefficient are given, the total attenuation/extinction coefficient can be obtained as $\mu_t = \mu_a + \mu_s$.

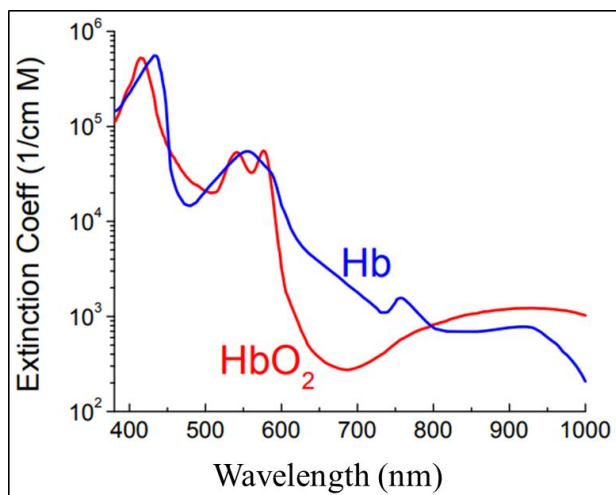


Figure 3-2: Absorption spectra of HbO₂ and Hb

(Photo credit: Scott Prahl, OMLC. Reference 131)

Anisotropy factor g . When a scattering event occurs, the trajectory of the photon is deflected by an angle θ . Each deflection is random, and it can be described using the Henyey-Greenstein phase function, which represents the probability distribution of the photon deflection angle θ at which the scattering event occurs: $P(\theta) = \left[\frac{1}{1-g} - \frac{1}{\sqrt{1+g^2-2g \cos \theta}} \right] \cdot \frac{1-g^2}{2g}$, where g is the scattering anisotropy factor, which is equal to the average of the cosine of the scattering angle: $g = \langle \cos \theta \rangle$ that measures how much the forward direction is retained after a scattering event. For most soft tissues, the value of g is between 0.65 and 0.95.^[143] When $g = 1, 0$ or -1 , it corresponds to three special cases of totally forward scattering, isotropic scattering and totally backward scattering.

Reduced scattering coefficient μ'_s . The introduction of the reduced scattering coefficient is to simplify the description of multiple scattering of photons within the biological tissue. The process in which photons are scattered for multiple times at a step

size of $\frac{1}{\mu_s}$ can be simplified as a single scattering event with a step size of $\frac{1}{\mu'_s}$, where $\frac{1}{\mu'_s}$ is called the reduced scattering free path and μ'_s is the reduced scattering coefficient. The reduced scattering coefficient connects to the scattering coefficient through the equation $\mu'_s = \mu_s(1 + g)$. It is important to note that the reduced scattering coefficient does not follow the superposition principle because the anisotropy factor does not change with concentration of scatters so that the reduced scattering coefficient is no longer linearly related to the concentration.

3.1.3 Modeling of light-tissue interaction using Monte Carlo simulation

Two different methods can be used to describe the absorption and scattering properties of light in biological tissues, namely analytical method and approximation method. The analytical method is based on Maxwell's equation and is the most basic description method in principle. However, the process of deriving the analytical solution is extremely complicated and not practical. Diffusion approximation, one of the most widely used approximation methods, directly describes the migration of photons in the absorption and scattering process. The feasibility of diffusion approximation has been experimentally verified.^[144,145] However, the diffusion approximation model is only suitable when the scattering coefficient is much larger than the absorption coefficient ($\mu_s \gg \mu_a$) and when the source-detection-separation (SDS) is much longer than the free pass of photon migration.^[146]

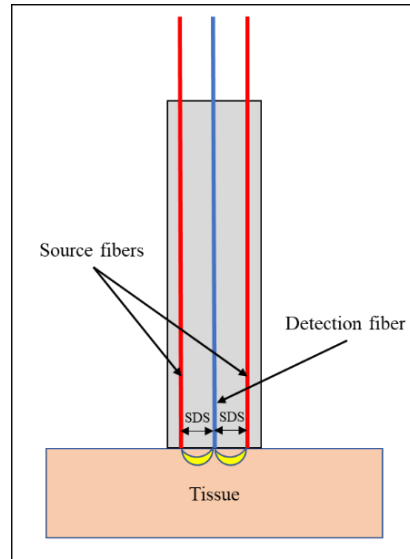


Figure 3-3: Illustration of source-detection-separation

In this study, the SDS is designed to be less than 1 mm in order to obtain enough signal using the optical fiber and the cellphone camera whose sensitivity is much lower than a scientific camera or photodetector, as illustrated in Figure 3-3. Therefore, diffusion approximation is not the best option for providing high accuracy in this application. Monte Carlo modeling of light reflectance developed by Lihong Wang *et al.*^[147,148] offers a better flexibility in terms of range of optical properties and the tissue geometry being studied due to the following advantages: 1) it has no limitation on the light source or boundary conditions so that it can equally be applied to single-layer or multi-layer structures; 2) it does not need to solve the transmission equation and is computationally simple; 3) it has no requirements of the optical parameters and hence works for media that are not scattering dominant. While detailed description about the Monte Carlo simulation of photon migration in tissue and sample programs can be found in reference [129] and [130], the basic idea of this method is described as follows.

To simplify the problem, photons are treated as neutral particles and the light incident is perpendicular to the surface of the tissue. Each photon has an initial weight of 1 and a random travel step $s = \frac{\ln \xi}{\mu_t}$ at its injection into the tissue, where ξ is a random number uniformly distributed between 0 and 1, $\mu_t = \mu_a + \mu_s$ is the total attenuation coefficient due to absorption and scattering. At each step it travels, the photon will be partially absorbed and partially scattered. Absorption causes the weight of the photon to decay. The amount of weight loss is $\Delta w = w \cdot \frac{\mu_a}{\mu_t}$, where w is the weight at the current position. Photon carrying the remaining weight $w - \Delta w = w \frac{\mu_s}{\mu_t}$ continues to transmit in the tissue. From the equations above, it is easy to see that the weight of the photon decays exponentially with a rate of $\frac{\mu_s}{\mu_t}$. While absorption reduces the weight of the photon, scattering changes the direction of propagation. After the photon is scattered, the travel distance s for the next step will be updated. The scattering angle θ , so as the anisotropy factor g , gives the new direction of movement of the scattered photon. As we mentioned in the previous section, the probability of distribution of the cosine of the scattering angle θ is defined by the Henyey-Greenstein phase function.

Consequently, a photon can either be absorbed by absorbers inside the tissue or escape from the tissue after multiple scattering events. For a photon that exits the tissue, it is treated as naturally terminated and the tracking of photon stops. For a photon that keeps propagating in the tissue, the tracking stops when the weight of photon decays to a value less than a preset threshold w_{TH} (e.g., $w_{TH} = 0.00001$). In this way, the Monte Carlo method simulates a large number of photons (in millions) individually as they transport in the tissue. A distribution of photon density at each position of the tissue can

be obtained. In homogenous media, the distribution is roughly banana-shaped between the light source and detector if photons are perpendicularly injected on the same surface of the media (Figure 3-3).

The major drawback of the Monte Carlo simulation is that it is computationally intensive that requires long computation time, especially when simulating a large number of photons. Different approaches have been reported to speed up the simulation.^[57,149-151] In this study, a flexible and fast Monte Carlo model proposed by Palmer *et al.*^[151] was used to extract the optical properties of the tissue or tissue-mimicking phantoms. This model has been validated for absorption coefficient at a range of 0 - 20 cm⁻¹ and reduced scattering coefficients of 7 - 33 cm⁻¹ with high accuracy and has been extensively tested in tissue-mimicking phantoms^[152,153] and multiple preclinical^[154,155] and clinical studies^[18,75,79,156,157]. Beyond this, the model is easily adaptable to arbitrary probe geometry and can be used with a single phantom calibration.

A brief description of Palmer's model is summarized as follows. The model consists of a forward model and an inverse model, as shown in Figure 3-4. The forward model uses pre-determined absorption coefficient, scattering coefficient and anisotropy factor to model the diffuse reflectance. Absorption coefficient μ_a is determined by the extinction coefficient ε_i of the chromophore and its concentration C_i according to the linear relationship $\mu_a = \sum \ln(10) \cdot \varepsilon_i(\lambda) \cdot C_i$. Scattering coefficient μ_s and anisotropy factor g are modeled using Mie theory for spherical particles.^[158] It is important to note that instead of running a simulation for each set of optical properties (μ_a , μ_s , g), a scaling approach^[159] was used in this fast Monte Carlo model to increase the efficiency of computation so that only one single simulation for a given set of μ_a , μ_s , g was required.

In the inverse model, initial parameters including chromophore concentration, size and density of scatterers are loaded into the forward model to model the diffuse reflectance as the predicted values. The measured (unknown) reflectance is then iteratively compared to the predicted values until the sum of squares error between them is minimized. In this way, a set of optical properties (μ_a , μ_s , g) of the measured reflectance can be extracted. From the optical properties, the tissue parameters such as oxy-hemoglobin concentration (HbO_2), deoxy-hemoglobin concentration (Hb), total hemoglobin concentration (THb), and tissue regional saturated oxygenation (rSO_2) can be accurately determined.

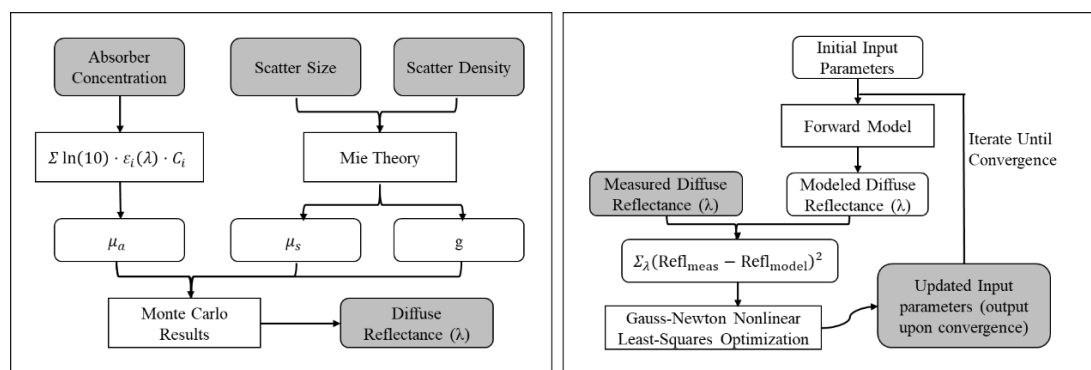


Figure 3-4: Forward and inverse models of Palmer's fast Monte Carlo simulation

(Photo credit: Palmer *et al.* Adapted from reference [133]). **Left:** forward model; **Right:** inverse model.

3.2 OPTICAL DESIGN

3.2.1 System layout

The smartphone-based diffuse reflectance spectrometer consists of a smartphone with a rear camera and imaging optics. A schematic diagram of the smartphone spectrometer is shown in Figure 3-5. The imaging optics include an aspheric lens for light collimation, an optical slit and a transmission grating. The DRS channel uses a white

LED as the light source. The white light is delivered to the tissue through two 200/220 μm multimode fibers, as shown in the end view of the DRS probe in Figure 3-5. Diffuse reflectance is collected by a single detection fiber, collimated by a collimating lens and then narrowed down by a 100 μm slit. The collimated lights are diffracted by a transmission grating and focused by the camera lens to be imaged on to the image sensor of the smartphone. The source-detector separation (center-to-center distance between the source fibers and the detection fiber) is 0.75 mm.

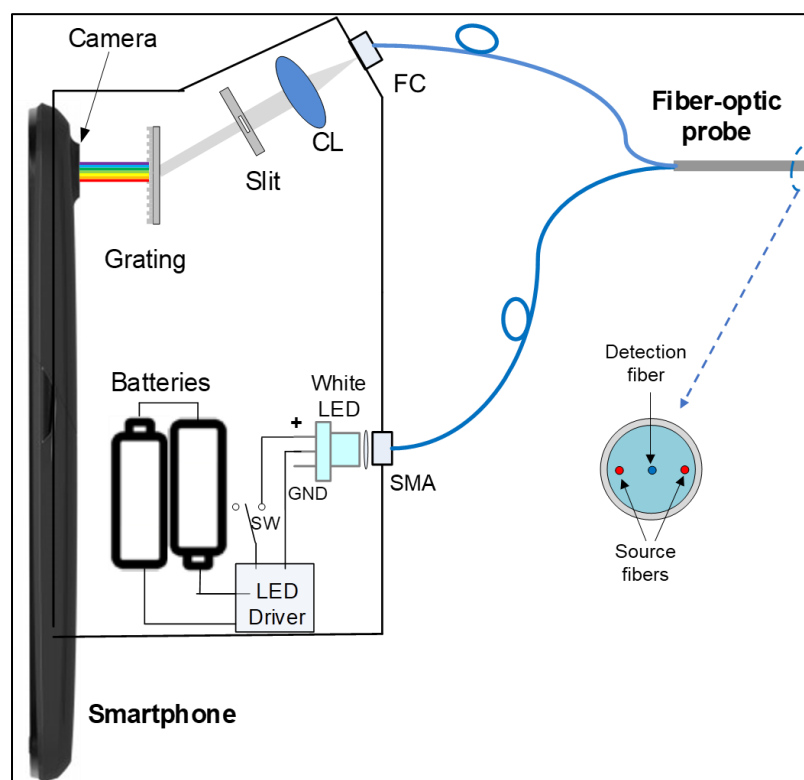


Figure 3-5: Schematic diagram of the smartphone-based DRS

CL – collimating lens; LED - light-emitting diode; GND – ground; SW – ON/OFF switch

3.2.2 Ray-tracing simulation

Prism and diffraction grating are two optical components that are commonly used to split the light in the design of a spectrometer. An optical prism disperses the light

based on the refractive effect, i.e., different wavelengths have different refractive indices so that they can be separated when passing through a prism. Generally, the shorter the wavelength, the larger the deflection angle. In the meantime, the resolution of the prism is higher at the shorter wavelength, which is not desirable in the design of a spectrometer from the perspective of “uniformity” or “linearity”. A diffraction grating uses the multi-slit diffraction effect to decompose the light. It is usually a piece of flat glass or metal engraved with tens of thousands of parallel lines/slits. The formation of light through the grating is a combined result of single slit diffraction and multi-slit interference. When the complex light passes through the grating, the lines of different wavelengths appear at different positions to form a spectrum. When compared to a prism, the spectrum generated by a diffraction grating is relatively uniform, and the distance between two spectral lines with the same wavelength difference does not vary. The uniformity of the grating spectrum not only makes the spectrum easier to calibrate, but also facilitates the preliminary judgment of the wavelength value of the spectral line for qualitative analysis.

Ray tracing simulation software such as Zemax provides the feature to design and model diffractive components. Diffractive surfaces in Zemax are modeled based on the grating equation^[160]: $d(n_2 \sin \theta_2 - n_1 \sin \theta_1) = m\lambda$, where d is the line spacing, n_1 and n_2 are refractive indices, θ_1 is the angle of incidence, θ_2 is the angle between the diffracted light and the grating's normal vector, m is the diffraction order and λ is the wavelength. In this design, the incident light with wavelength λ propagates in the air and normally hits the grating as depicted in Figure 3-6, therefore $\theta_1 = 0$, $n_1 = n_2 \approx 1$. From

the grating equation, the diffraction angle θ_2 can be derived as $\theta_2 = \sin^{-1} \frac{m\lambda}{d} =$

$\sin^{-1} Nm\lambda$, which depends only on the line spacing (d) or the groove density $N = \frac{1}{d}$.

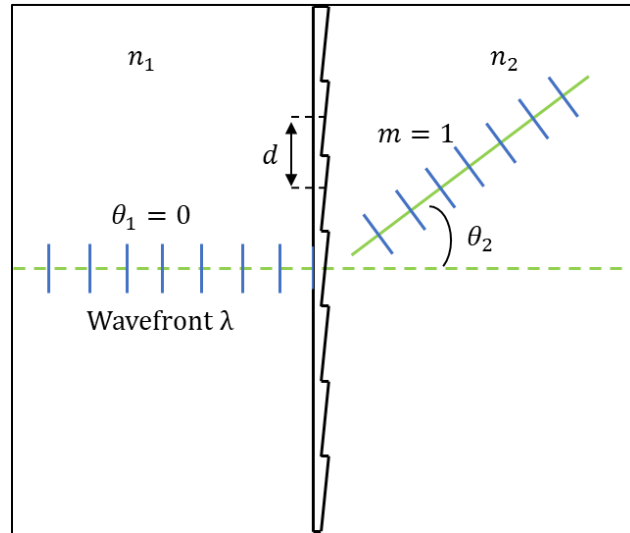


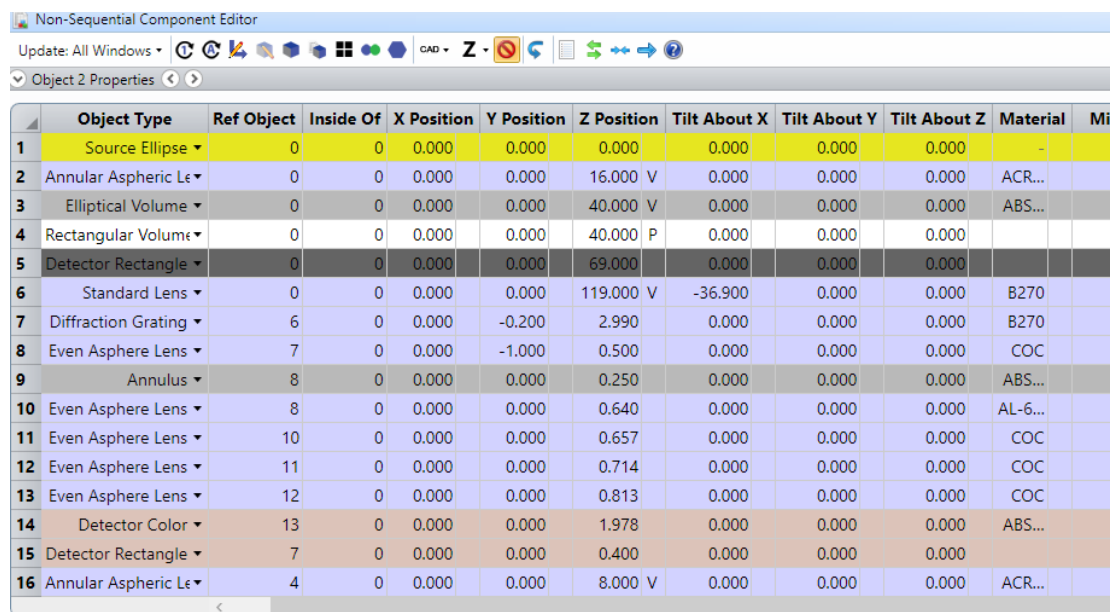
Figure 3-6: Diagram showing light incident normally to a transmission diffraction grating

Throughput and optical resolution are the two most important characteristics of a spectrometer. Generally, there is a tradeoff between resolution and throughput, and they really depend on the specification of the components to be used, especially the grating and slit. For example, grating with a higher groove density has a broader dispersion (nm/pixel) for the same wavelength range; Slit with a smaller entrance (slit width) has a better pixel resolution. Consequently, using a high groove density grating together with a narrower slit will significantly increase the resolving power. However, the signal strength decreases with an increase in the groove density or decrease in the slit width, leading to a lower signal to noise ratio. Simulation of the DRS design is to evaluate whether the proposed combination of the grating (1200 grooves/mm) and slit (100 μm) can provide enough signal strength with acceptable spectral resolution, and to determine the distances

between components. In this study, throughput is more critical because diffused light signal through tissue that can be collected by the optical fiber is extremely weak.

Therefore, the efficiency of the grating is not the most critical factor to be examined in this design, it is assumed to be 100% in Zemax although it depends on the structure of the diffractive surface in the real situation. In the LDE shown in Table 3-1, a groove density of 1200 g/mm and a slit width of 100 μm were assigned to the diffraction grating and slit, respectively. The 1st diffraction order was specified to be simulated. The optimized geometries and simulated spectral image at the camera sensor (last surface in the design) are shown in Figure 3-7. Discrete wavelengths range from 400 nm to 600 nm with an interval of 10 nm were used in the simulation.

Table 3-1: Values defined in the LDE for DRS



Object Type	Ref Object	Inside Of	X Position	Y Position	Z Position	Tilt About X	Tilt About Y	Tilt About Z	Material	Mi
1 Source Ellipse	0	0	0.000	0.000	0.000	0.000	0.000	0.000	-	
2 Annular Aspheric Le	0	0	0.000	0.000	16.000 V	0.000	0.000	0.000	ACR...	
3 Elliptical Volume	0	0	0.000	0.000	40.000 V	0.000	0.000	0.000	ABS...	
4 Rectangular Volume	0	0	0.000	0.000	40.000 P	0.000	0.000	0.000		
5 Detector Rectangle	0	0	0.000	0.000	69.000	0.000	0.000	0.000		
6 Standard Lens	0	0	0.000	0.000	119.000 V	-36.900	0.000	0.000	B270	
7 Diffraction Grating	6	0	0.000	-0.200	2.990	0.000	0.000	0.000	B270	
8 Even Asphere Lens	7	0	0.000	-1.000	0.500	0.000	0.000	0.000	COC	
9 Annulus	8	0	0.000	0.000	0.250	0.000	0.000	0.000	ABS...	
10 Even Asphere Lens	8	0	0.000	0.000	0.640	0.000	0.000	0.000	AL-6...	
11 Even Asphere Lens	10	0	0.000	0.000	0.657	0.000	0.000	0.000	COC	
12 Even Asphere Lens	11	0	0.000	0.000	0.714	0.000	0.000	0.000	COC	
13 Even Asphere Lens	12	0	0.000	0.000	0.813	0.000	0.000	0.000	COC	
14 Detector Color	13	0	0.000	0.000	1.978	0.000	0.000	0.000	ABS...	
15 Detector Rectangle	7	0	0.000	0.000	0.400	0.000	0.000	0.000		
16 Annular Aspheric Le	4	0	0.000	0.000	8.000 V	0.000	0.000	0.000	ACR...	

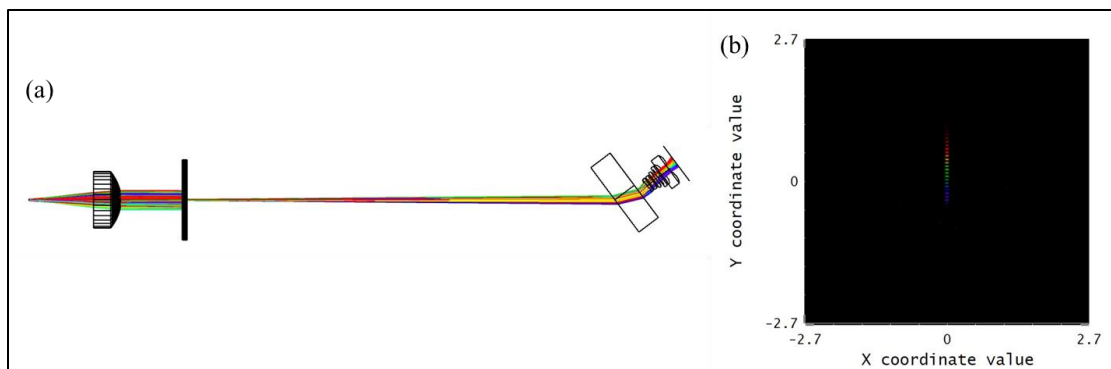


Figure 3-7: Ray-tracing simulation of the DRS system

(a) Elements from left to right: collimating lens, 100 μm slit, 1200 g/mm transmission grating, and cellphone camera with lens and sensor. (b) Simulated spectral image of the 1st diffraction order given discrete wavelengths range from 400 nm to 600 nm with 10 nm intervals.

3.2.3 System assembly

Figure 3-8 illustrates the construction of the DRS system. All the components are shown at their relative locations. It is important to note that the aspheric lens (4) (Thorlabs C110TMD-A) has a relatively short focal length of 4 mm so that it should be placed very close to the FC/PC adapter (1) where the detection fiber will be connected to. A 100 μm slit (Thorlabs S100RD) and 1200 grooves/mm grating (Thorlabs GT13-12) were used to obtain enough signal and, in the meantime, to have adequate resolving power. It is important to note that because a multimode fiber with a diameter of 200 μm and numerical aperture (NA) of 0.22 is used, the relatively larger diameter of the fiber may become the limiting factor of the system resolution even if narrower slits were being used.

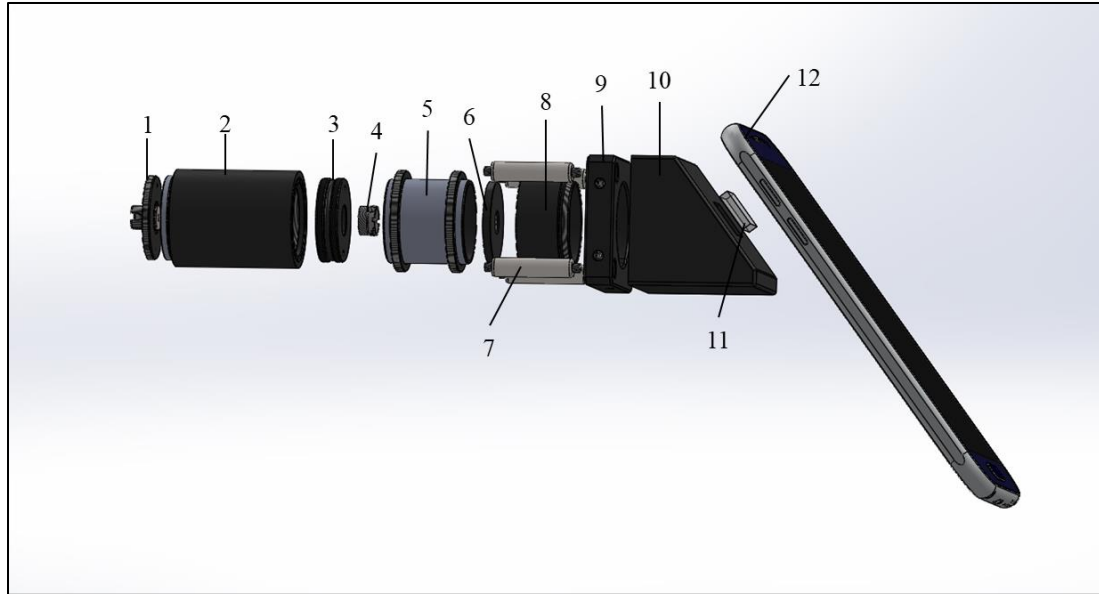


Figure 3-8: Exploded view of all components for DRS

Exploded view showing the relative locations of (1) FC/PC adapter, (2) 2" long lens tubes, (3) SM1 to M9 x 0.5 lens adapter, (4) mounted aspheric lens, (5) 1" long lens tube coupler, RMS adapter, (6) 100 μm slit, (7) 1" long cage assembly rods, (8) 0.5" long lens tubes, (9) cage, (10) grating holder, (11) 1200 groove/mm transmission grating, (12) Samsung Galaxy S6 cellphone.

Another important factor worth attention is the collimation of light. Ideally, light pass through a collimating lens or a collimator should have a fixed size of the beam.

However, no collimation is perfect because there is no actual point source. Consequently, the beam divergence must be considered in the design. Figure 3-9 shows the collimation of light from a fiber. A fiber with a radius of r_1 is placed at the focal point (f) of the collimating lens. The maximum ray of angle out of the fiber is θ_1 . The beam size will be determined by the NA of the fiber and focal length of the collimating lens so that $r_2 = r_1 + f \cdot \tan \theta_1$. Given that the radius of the fiber is usually much smaller than the focal length and $\tan \theta_1 \approx \theta_1$, the radius of the collimated beam can be simplified as $r_2 \approx f \cdot \theta_1$ and increases as it propagates away from the lens with a divergence angle $\theta_2 \approx \frac{r_1}{f}$.^[161]

From the equations derived above, the beam size is directly proportional to the focal

length while the divergence angle is inversely proportional to it. In other words, there is also a tradeoff between the beam diameter and the divergence angle. Obtaining a smaller size of beam spot will at the expense of better collimation.

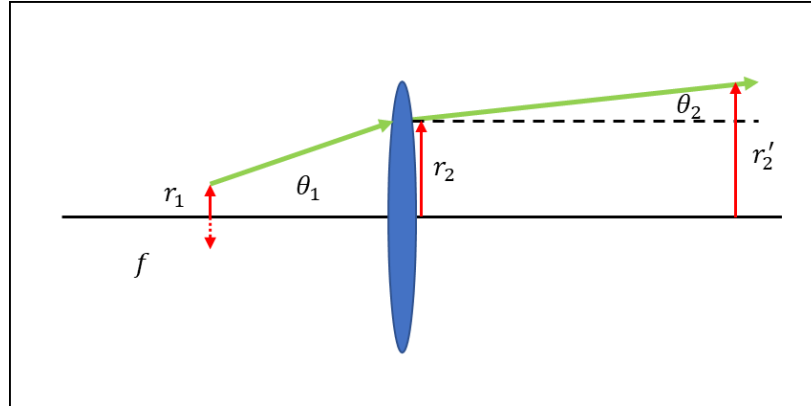


Figure 3-9: Collimation of light from a fiber

(Photo credit: Newport. Adapted from reference 160)

In our design, the radius and numerical aperture of the fiber is $100\ \mu\text{m}$ (r_1) and 0.22, respectively. Therefore, the maximum ray of angle θ_1 equals to 0.22 or 12.7° . Given that the focal length of the collimating lens used in the design is 6.24 mm, the radius of the beam is calculated to be 1.37 mm and the divergence angle of 0.016 or 0.9° . These values are suitable for our application because the slit has a maximum length of 3 mm that is wider than the beam diameter. We wanted to collect as much light as possible to achieve the maximum throughput. The complete smartphone-based DRS is shown in the figure below.

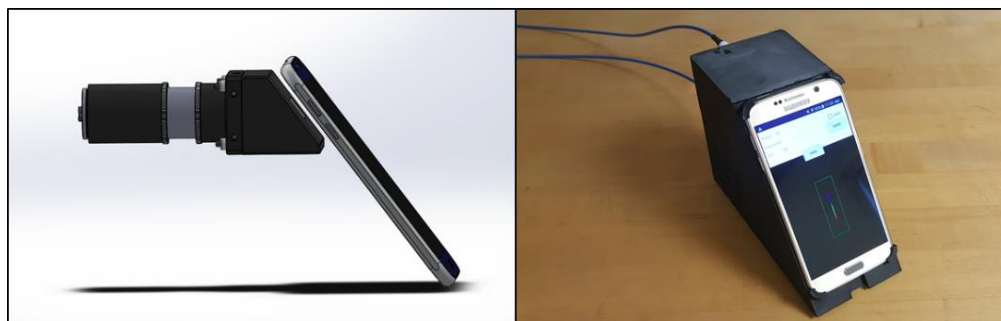


Figure 3-10: The completed smartphone DRS system

Left: the completed DRS system with major optic components. **Right:** picture of the completed DRS system housed in a 3D-printed enclosure, and the fiber-optic probe attached.

3.3 PERFORMANCE CHARACTERIZATION

3.3.1 Wavelength calibration and resolution verification

Two calibration lamps, krypton (6031, Newport) and neon (6032, Newport), were used for wavelength calibration of the DRS system because they have multiple narrow and intense peaks in the visible range. The raw images of the calibration light sources captured by the device are presented in Figure 3-11. A window of 1500×60 (X \times Y) pixels (red box) was used to crop out the 1st diffraction order dispersed spectra. The cropped image was then converted to grayscale, and 60 Y-axis pixel values at the same X location were added up to represent the intensity.

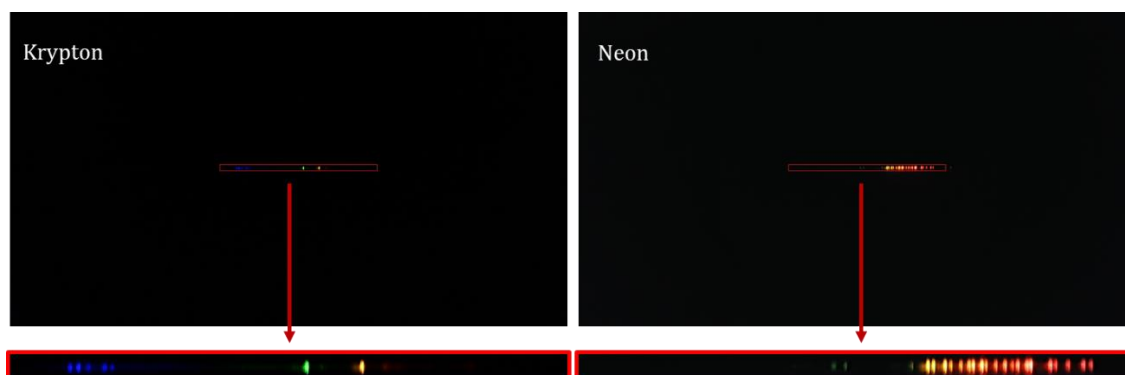


Figure 3-11: Raw and cropped spectral images of calibration lamps

The wavelength calibration was performed by identifying the known peak wavelengths of the calibration lamps and the corresponding pixel positions of the peaks in the spectra. Thirteen peak wavelengths across the range of 420 – 640 nm were identified based on the data sheet provided by the manufacturer^[162], as shown in Figure 3-12.

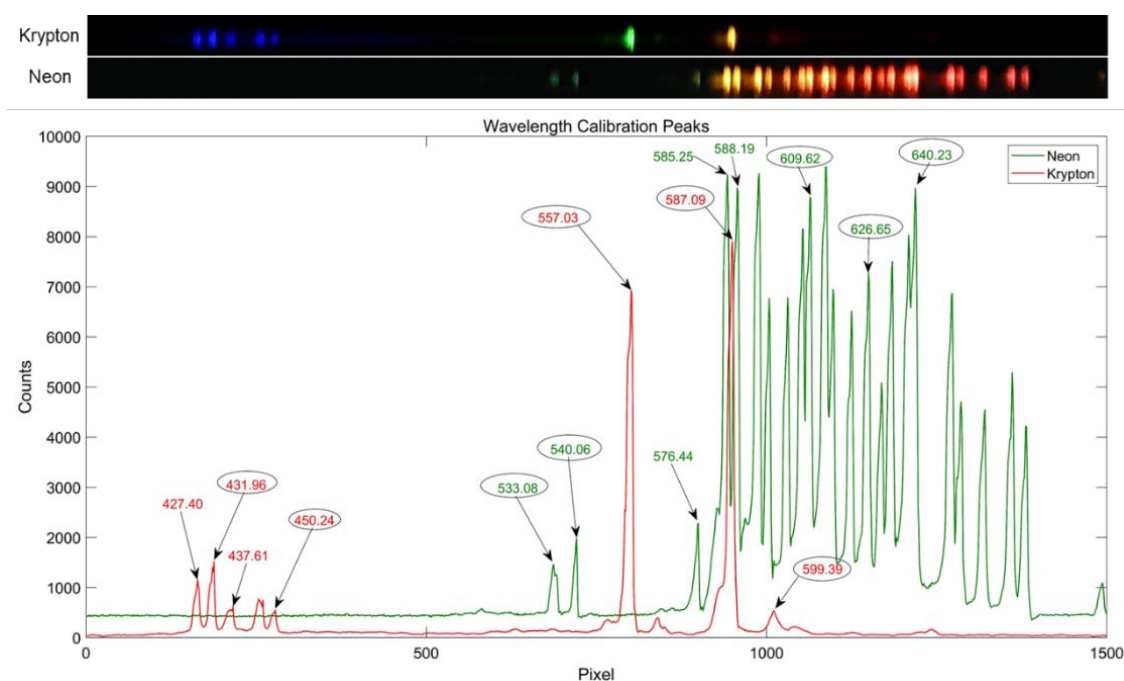


Figure 3-12: Peak wavelengths used for wavelength calibration

The peak wavelengths and pixel positions were fitted with a third-degree polynomial fitting (cubic polynomials) to generate a calibration equation $Y = aX^3 + bX^2 + cX + d$ so that wavelength can be calculated based on it. In the equation, Y is the wavelength, X is the pixel location, and a, b, c and d are coefficients. Table 3-2 provides the calibrated wavelength values calculated using the following cubic function: $Y = -1.01328 \times 10^{-8} \cdot X^3 + 1.94689 \times 10^{-5} \cdot X^2 + 0.19222 \cdot X + 395.32166$. The differences between the calibrated and known values were within the range of -0.45 nm

to 0.26 nm. The total wavelength range of a 1500-pixel spectrum was calculated to be 395.5 nm to 693.3 nm. Therefore, the dispersion was about 0.2 nm/pixel. The spectral resolution of a spectrometer was usually defined as the full width at half maximum (FWHM) of monochromatic light. At the peak of 557.03 nm in Figure 3-12, the FWHM was 10 pixels. Therefore, the spectral resolution was estimated at 2 nm (0.2 nm/pixel multiply by 10).

Table 3-2: Wavelength calibrated using third-degree polynomial fitting

Peak Wavelength (nm)	Pixel Location	Calibrated Wavelength (nm)	Difference (nm)
431.96	188	432.08	0.12
450.24	278	450.05	-0.19
533.08	687	533.28	0.20
540.06	721	540.24	0.18
557.03	801	556.58	-0.45
576.44	900	576.70	0.26
585.25	943	585.40	0.15
587.09	950	586.82	-0.27
594.48	989	594.67	0.19
599.39	1011	599.09	-0.30
609.62	1064	609.68	0.06
626.65	1150	626.71	0.06
640.23	1219	640.22	-0.01

To further verify the resolving power of the DRS device, a spectral image of a handheld laser source with a wavelength ~635 nm (HLS635, Thorlabs) was taken. The typical spectrum of the output light provided by the manufacturer was shown in Figure 3-13(c). The wavelength of the light source is centered at ~637 nm and has short tails on both sides. The spectrum detected using the smartphone-based DRS device were given in Figure 3-13(a), (b), and (d). The sharp peak is centered at 636.3 nm and has an FWHM of ~2 nm, which confirms the optical resolution of the device.

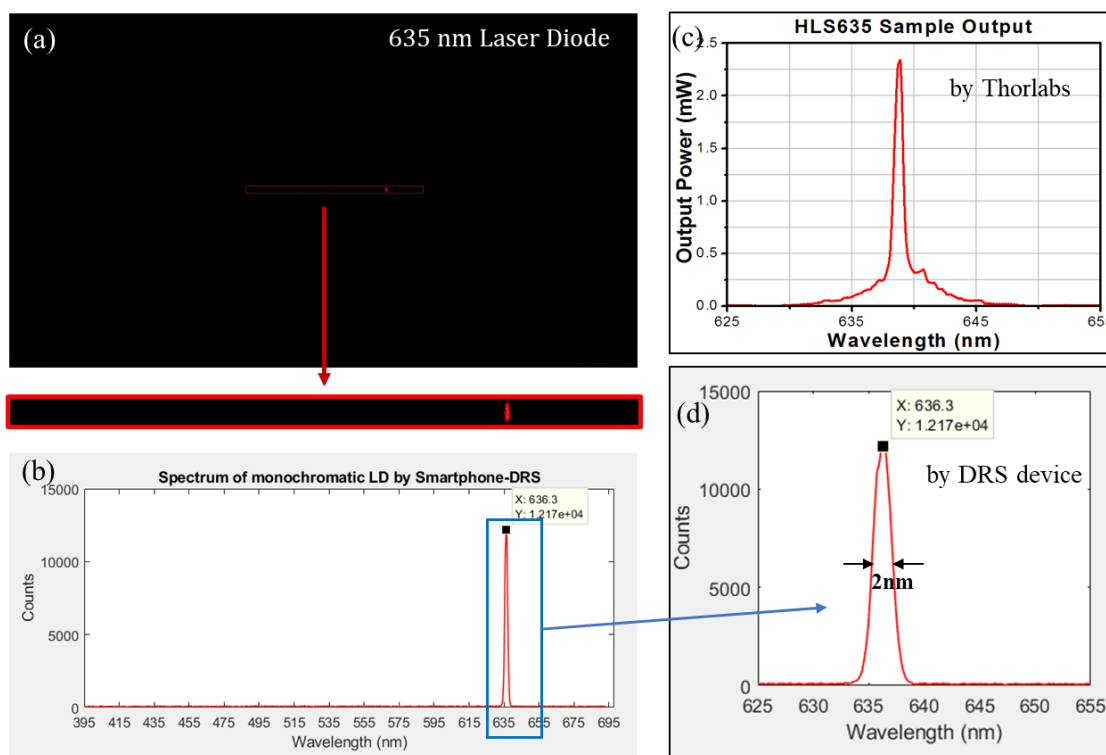


Figure 3-13: Spectrum of a monochromatic light source

(a) Raw and cropped spectral image of a 635 nm handheld laser source; (b) Wavelength calibrated spectrum taken by smartphone-based DRS; (c) typical spectrum of the light source provided by the manufacturer; (d) FWHM indicated that the resolution is about 2 nm.

3.3.2 Phantom validation

To characterize the accuracy of the DRS channel in measuring optical properties of biological samples, 14 tissue-mimicking liquid phantoms with a mean absorption coefficient (μ_a) averaged over the wavelength range from 430 -630 nm between 1 cm^{-1} - 3 cm^{-1} and a mean reduced scattering coefficient (μ_s') between 7 cm^{-1} - 12 cm^{-1} were created using powdered human hemoglobin (H0267, Sigma Aldrich) as absorbers and $1.0 \mu\text{m}$ polystyrene microspheres (07310, Polyscience, Inc.) as scatterers (Table 3-3). The expected μ_a of the phantoms were independently determined from absorbance measurements of the stock hemoglobin solution using a UV/Vis spectrophotometer

(LAMBDA 35, PerkinElmer Inc.) and scaled to the actual concentrations in the phantoms. The expected μ'_s was computed from the density, size, and refractive index of the polystyrene spheres using Mie theory.^[147,158]

Table 3-3: Expected phantom properties averaged over 430 nm – 630 nm

Phantom #	μ_a (cm^{-1})	μ'_s (cm^{-1})	Phantom #	μ_a (cm^{-1})	μ'_s (cm^{-1})
1	1.02	11.64	8	2.37	8.84
2	1.26	11.14	9	2.51	8.55
3	1.48	10.67	10	2.64	8.27
4	1.69	10.25	11	2.76	8.01
5	1.88	9.86	12	2.88	7.77
6	2.05	9.49	13	2.99	7.54
7	2.21	9.15	14	3.09	7.33

A raw picture of the spectral image is shown in Figure 3-14. Spectra were taken at an exposure time of 0.25 second. The 1st order diffractions were cropped out and calibrated using the cubic function obtained in the previous section. Averaged smoothed raw spectra of all of the 14 phantoms are also provided in the following figure. The spectral intensity decreases as the concentration of hemoglobin increases because more light is absorbed within the phantom.

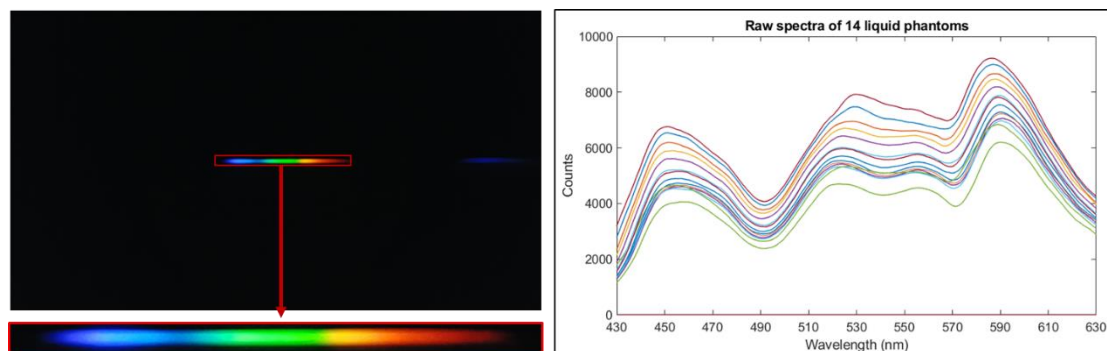


Figure 3-14: Spectra of liquid phantoms

Left: A sample picture (phantom #5) of the raw and cropped spectral images measured from liquid phantoms; **Right:** Wavelength calibrated spectra of all 14 phantoms (intensity of spectrum decreases while the phantom number increases).

The absorption and reduced scattering coefficients μ_a and μ'_s were extracted from the measured spectrum of each phantom using the scaling inverse Monte Carlo model discussed in the first section. The extracted parameters were compared to the expected values, as shown in Figure 3-15. Specifically, the difference between the extracted and expected values (error) was calculated and divided by the expected value. An average error of 6.9% and 5% were obtained for μ_a and μ'_s .

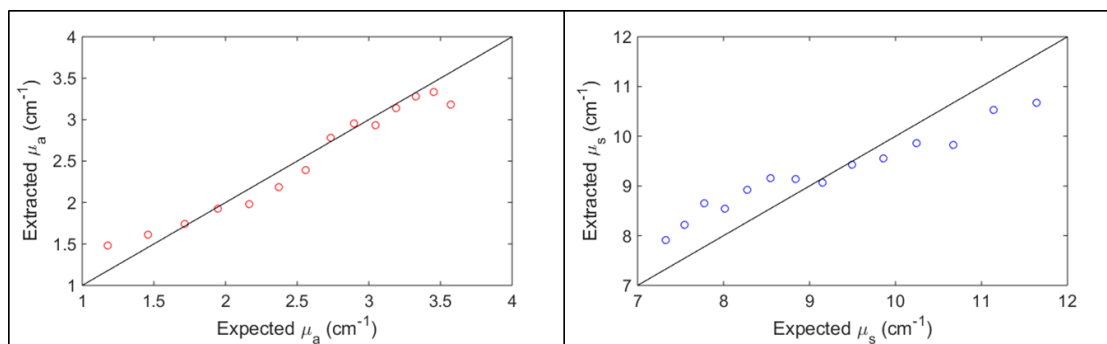


Figure 3-15: Extracted vs. expected μ_a and μ'_s for all phantoms

3.4 DISCUSSION

A benchtop DRS system has been developed in our lab to quantify the optical properties of epithelial tissues. As shown in Figure 3-16(left, top), the spectrometer consists of a three-channel fiber-optic USB spectrometer (Avantes BV, The Netherlands) and a laptop with custom LabVIEW and Matlab software. This commercial spectrometer covers a wavelength range of 400 - 635 nm with a spectral resolution of 1.8 nm. Liquid phantoms covering a similar range of absorption and scattering coefficients used for the smartphone-based DRS validation were employed to evaluate its performance. Figure 3-

16(right, top row) shows the results of the phantom experiment as extracted versus expected wavelength averaged μ_a and μ'_s calculated from the spectra. A mean error of 1.4 % and 6.8% were obtained for μ_a and μ'_s , respectively. The error bars in the plots were due to the different reference phantoms. As a comparison, for the smartphone-based DRS, mean error of 6.9% and 5% were obtained for μ_a and μ'_s . The results are comparable to those of the benchtop DRS system, as shown in Fig. 3-16(right, bottom row).

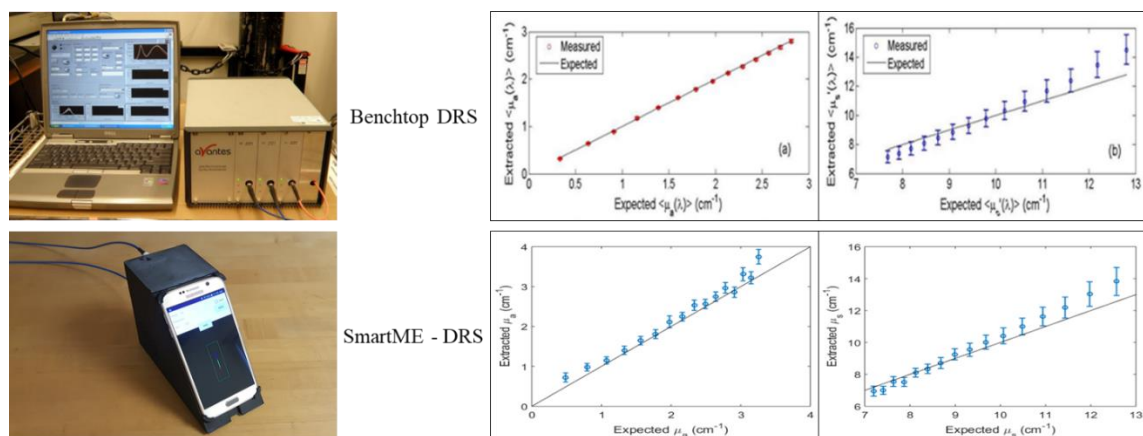


Figure 3-16: Compare between smartphone-based DRS system with a commercial spectrometer

Left: photographs of the benchtop DRS system and experimental SmartME-DRS (w/o FLI channel). **Right:** results of a liquid phantom experiment using the commercial system (top) and smartphone-based DRS (bottom).

Clinical study has been conducted by different groups using a similar benchtop spectrometer and Monte Carlo model to reveal the underlying sources of absorption and scattering contrast in 39 cervical cancer patients.^[79] A significant increase in total hemoglobin concentration was observed in CIN2+ compared to CIN1 lesions and normal tissues. In the meantime, a decrease in mean scattering μ'_s was observed in CIN2+

compared to CIN1 and normal tissues. The result is consistent with others who carried out quantitative spectroscopy of the cervix.^[100,163]

CHAPTER 4: A DUAL-MODALITY SMARTPHONE MICROENDOSCOPE FOR QUANTIFYING THE PHYSIOLOGICAL AND MORPHOLOGICAL PROPERTIES OF EPITHELIAL TISSUES

Portions of this chapter are derived from the manuscripts submitted to Scientific Reports:

Xiangqian Hong, Tongtong Lu, Liam Fruzyna, and Bing Yu. A Dual-modality Smartphone Microendoscope for Quantifying the Physiological and Morphological Properties of Epithelial Tissues. *Scientific Reports*. Submission ID: SREP-19-05266.

In the previous two chapters, we present the development of a smartphone-based fluorescence microendoscope and a smartphone-based spectrometer individually. In this chapter, we further developed a dual-modality fiber-optic microendoscope (named SmartME) that integrates the high-resolution FLI and quantitative DRS onto a smartphone platform for noninvasive quantification of the tissue physiological and morphological properties of epithelial tissues. The SmartME has a spatial resolution of $\sim 3.5 \mu\text{m}$ for FLI and accuracy comparable to those of a benchtop DRS system for measuring the tissue absorption and scattering properties.^[75] When used with the App, the device can be used to perform FLI and DRS on epithelial tissues, wirelessly transfer the data to a remote server for data processing, and potentially return the results to the SmartME within seconds or a few minutes. Our preliminary studies have demonstrated that the dual-modality SmartME can accurately characterize the biological properties and provide complementary information about epithelial tissues. The SmartME has great potential to provide a compact, cost-effective, and ‘smart’ solution for early detection of neoplastic changes in epithelial tissues, especially in low resource settings.

4.1 HARDWARE DEVELOPMENT

4.1.1 SmartME instrumentation

A schematic diagram of the SmartME device is shown in Figure 4-1. The system consists of a smartphone (Samsung Galaxy S6), a miniature fiber-optic endoscope, a phone attachment containing the imaging optics, and an Android Application (App). The system includes two functional channels, an FLI channel and a DRS channel. The details of the configurations of each channel have been described in chapter 2 and 3, respectively. Briefly, a blue LED (455 nm, M455L3, Thorlabs) coupled with a condenser lens (ACL2520U-A, Thorlabs) and a short-pass excitation filter (FF01-452/45, Semrock) are used for fluorescence excitation. The excitation beam is redirected by a dichroic beamsplitter (DBS, AT485DC, Chroma Technology) towards a 10× microscope objective which focuses the excitation lights onto the proximal end of a fiber bundle in the endoscope. The fluorescence emissions are collected by the same fiber bundle at the distal end, propagate through the objective, DBS and a long-pass emission filter (FF01-550/88, Semrock) that blocks the excitation lights, and then are collimated onto the rear camera of the smartphone by a 16× eyepiece. The imaging fiber bundle (FIGH-30-650S, Fujikura) has an imaging area of 600 μm and consists of 30,000 individual fibers with a center-to-center distance of ~3.3 μm. The choice of the blue LED, filters and dichroic beamsplitter for the FLI is based on the use of proflavine.

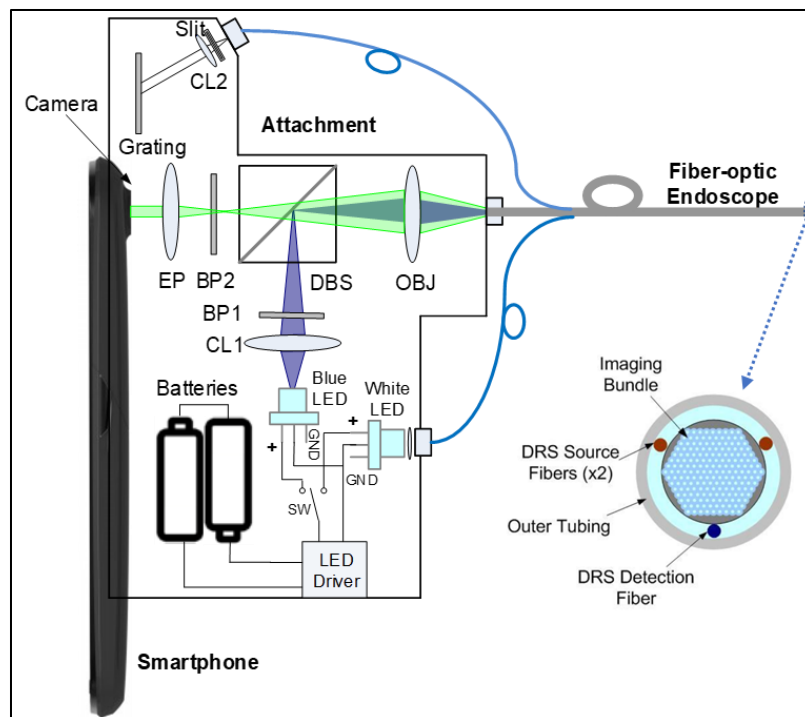


Figure 4-1: Schematic diagram of the SmartME

A schematic diagram of the SmartME and an end view of the miniature dual-modality fiber-optic endoscope (EP - eyepiece; BP1 & BP2 - optical bandpass filters; DBS - dichroic beamsplitter; OBJ - microscope objective; CL1 - condenser lens; CL2 – collimating lens; LED - light emitting diode; GND - ground; SW - ON/OFF/ON switch).

The DRS channel uses a white LED (MCWHF2, Thorlabs) as the light source.

The white light is delivered to the tissue through two 200/220 μm multimode fibers attached along with the imaging fiber bundle, as shown in the end view of the endoscope in Figure 4-1. Diffuse reflectance is collected by a single detection fiber, narrowed down by a 100 μm slit (S100RD, Thorlabs), and then collimated by a collimating lens. The collimated lights are diffracted by a 1200 grooves/mm transmission grating (GT13-12, Thorlabs) and then imaged on to the rear camera of the smartphone. The source-detector separations (center-to-center distance between the source fibers and the detection fiber) are 0.75 mm. The LEDs are powered by the same rechargeable batteries and turned on/off sequentially using a 3-position switch. Both the FLI and DRS channels were

designed and optimized using a combination of the sequential and non-sequential modes in OpticStudio (Zemax LLC).

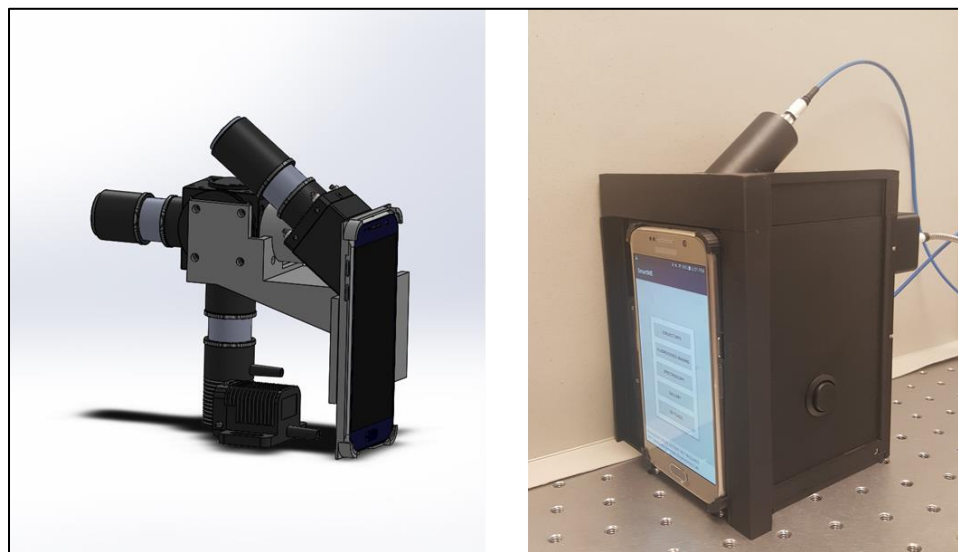


Figure 4-2: The completed SmartME device

Left: the assembly of the SmartME device by combining the FLI and DRS module using 3D printed adapters and a slide mechanism. **Right:** a picture of the combined SmartME device.

The front-face camera has also been tested for the DRS during the development. However, compared to the rear camera, the front-face camera has a much lower imaging quality, and its focal length is fixed. Therefore, using the front-face camera requires a lot of trial-and-error testing to get an acceptable alignment, while the performance of DRS may still be vulnerable to a minimal misalignment. Consequently, the rear camera was used for both FLI and DRS. A sliding mechanism with a fixed moving distance was installed so that the phone can be switched back and forth smoothly to achieve different imaging functions one at a time. The two channels were combined and protected using 3D printed parts that specially made for this design.

4.1.2 Fabrication of miniature fiber-optic probe

The imaging fiber bundle and three DRS fibers were integrated into a fiber-optic endoscope of less than 3 mm in diameter, shown in Figure 4-3. The imaging bundle has 30,000 pixels with a pixel size of $\sim 3 \mu\text{m}$ and an imaging area of 0.65 mm in diameter. At the distal end of the probe, three 200 μm DRS fibers were mounted along with the imaging bundle, two for DRS illumination and one for detection of diffuse reflectance. The center-to-center distance between the source and detection fibers (or SDS) was about 750 μm . According to our simulation with the Monte Carlo forward model with a range of optical properties representative of typical epithelial tissues, this SDS provides a penetration depth of 0.5-2 mm for the wavelength range of 450-630 nm^[75], which would be sufficient to catch most precancerous (CIN1 - CIN3) lesions in the epithelium and stroma layers of the cervix. At the proximal end, the endoscope broke out into three branches. The imaging bundle was connected to the port for fluorescence imaging. The source fibers were connected to a white LED, and the detection fiber was connected to the port for diffuse reflectance spectroscopy. The distal end of the probe was housed in a surgical grade stainless-steel tube so that it can be easily cleaned and sterilized in the medical application.

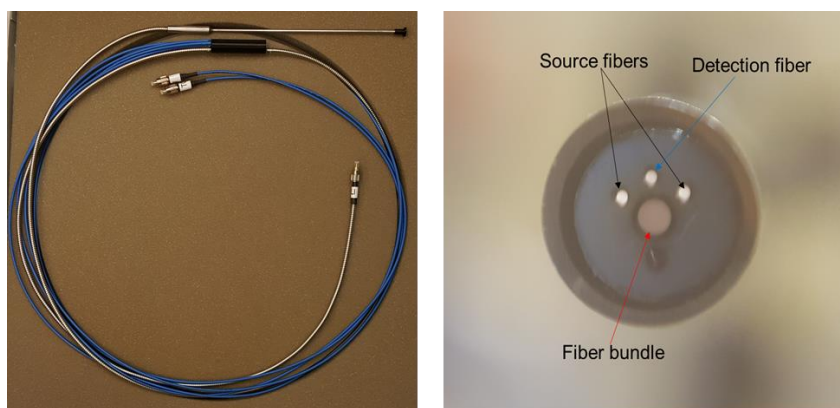


Figure 4-3: Picture of the integrated dual-modality endoscope probe

Left: A picture of the dual-modality probe. The fiber bundle was protected using a stainless-steel armor jacket. The DRS fibers were protected using 3mm blue jacket. Right: an end view of the probe. All optic fibers were housed in a stainless-steel tubing of 3mm in diameter.

4.2 SOFTWARE DEVELOPMENT

4.2.1 Smartphone App development

An Android App has been developed to configure and control the SmartME, pre-process the fluorescence and DRS images, and wirelessly transfer the fluorescence images and diffuse reflectance spectra. The Android App allows a user to set and save the camera parameters, initiate a measurement, store the measured data, display the spectra, perform simple analysis on the results such as gray-scale image conversion and wavelength calibration and communicate with the Cloud services and server. Figure 4-4 shows the architecture of the App workflow. The App consists of two primary interfaces, one for the acquisition and processing of fluorescent images and the other for the collection and processing of spectral images. They are independently controlled and the settings are saved separately.

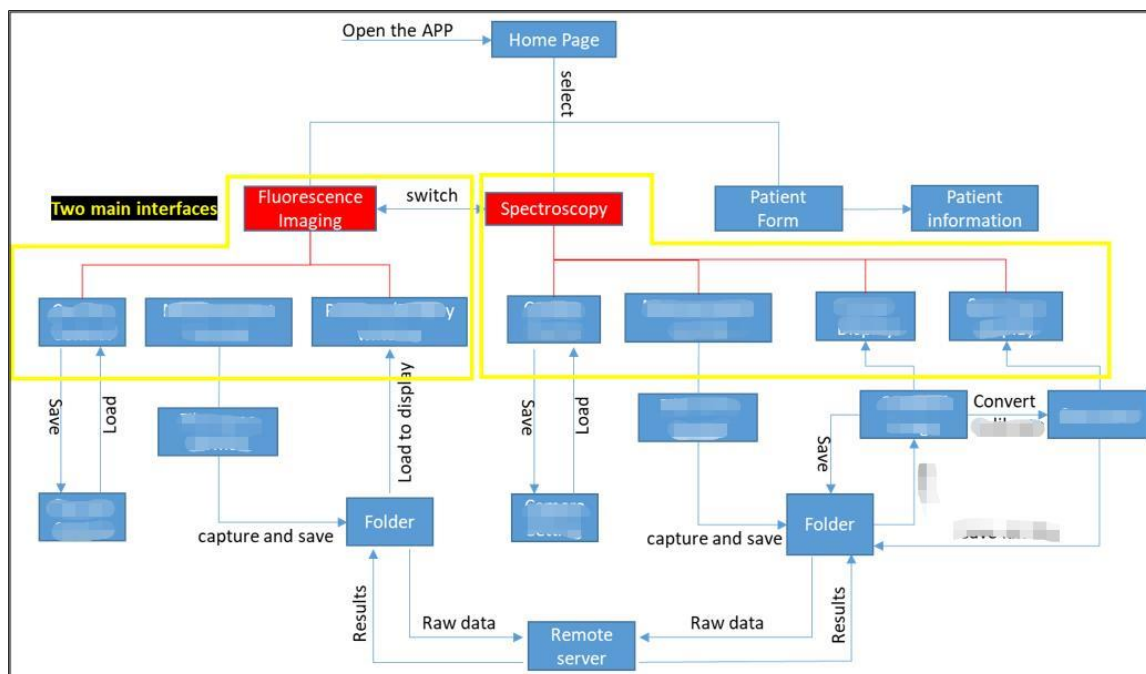


Figure 4-4: Architecture of the smartphone App

During a procedure, a doctor can use a patient ID or name to retrieve the PHI from the hospital's electronic medical records (or manually entered, if not available) and display it on the screen. For each new SmartME procedure, a unique ID related to the patient ID was generated. The App also assigns a site number and a measure number for each measurement saved, and the measure number increases automatically after completion of one scanning. Figure 4-5 shows the screenshots of the main menu and interfaces of the FLI and DRS modules. Measurement information, including the site number, measure number, integration time (for DRS and FLI), and diagnosis status will be displayed on the screen. The remote server downloads the data from the Cloud performs the image/spectral analysis and diagnosis (the images could be read by a physician as well) and returns the results to the App for display.

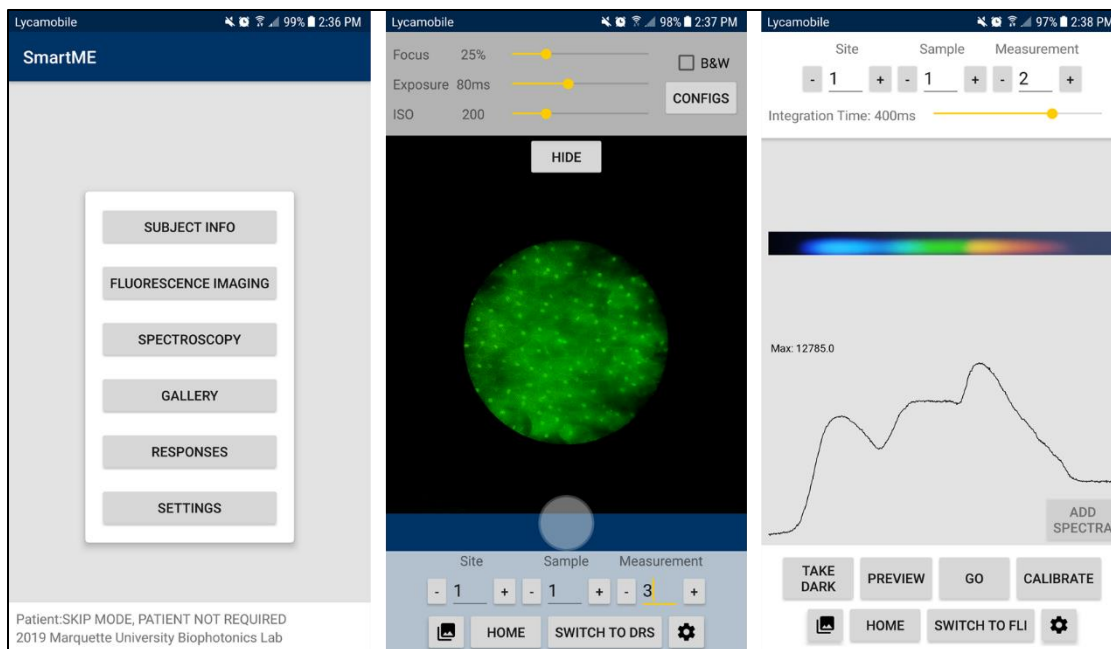


Figure 4-5: Screenshots of the SmartME App

Left: the home screen of the App that allows the operator to enter the patient/subject information and configure the settings for the measurement. **Middle:** the user interface of the FLI module. The focus and exposure time can be manually controlled to obtain the best imaging quality. **Right:** the user interface of the DRS module. Both the raw spectral image and spectrum were displayed for better visualization during measurement.

While it is impossible to go over all the details of the App, several critical features that specially designed are presented as follows. In order to increase the speed of data transmission and processing, the DRS spectrum within the region of interest is cropped out, wavelength calibrated and converted to a text file in the App before sending to the server for further analysis using the Monte Carlo inverse model. A window of 1500 pixels \times 60 pixels is defined in the setting, as shown in Figure 4-6. A saturation check is then performed in the background before proceeding to wavelength calibration. A warning window will pop out if any pixels of the image becomes saturated. Recall that there are four coefficients in the cubic equation for wavelength calibration. These calibration parameters are saved in the App so that spectral images without saturation are

automatically calibrated and converted to a text file for display and data transfer, as shown in Figure 4-6.

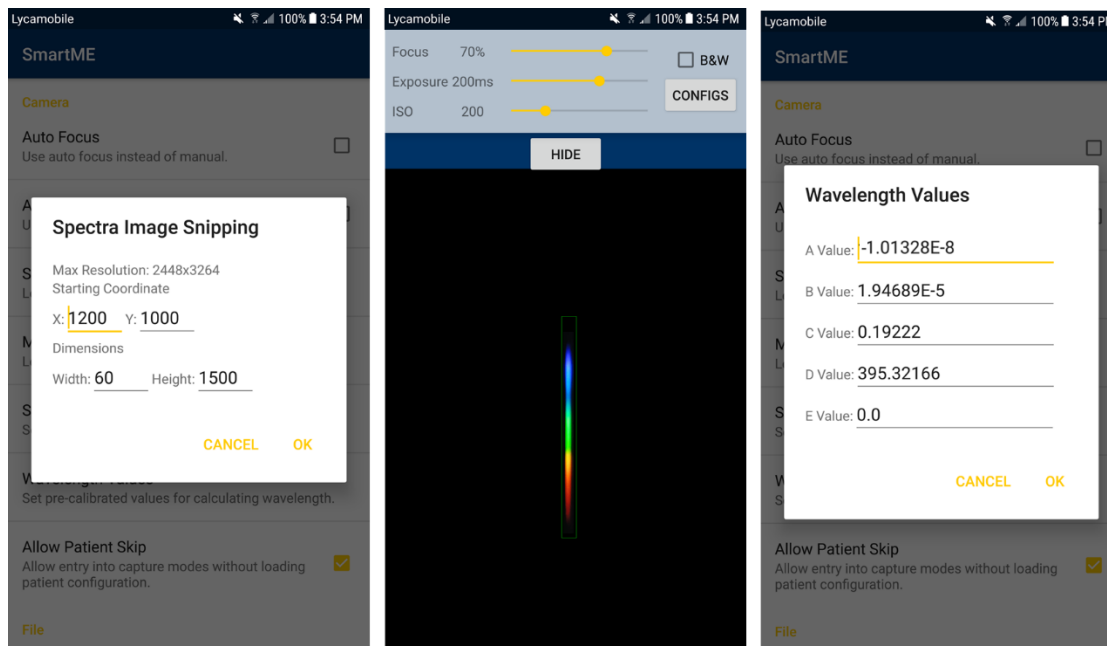


Figure 4-6: Image snipping and wavelength calibration in the App

Left: the setting window to define the area to be cropped out. **Middle:** A green window covering the whole spectrum is set for image snipping. **Right:** Coefficients obtained from the cubic equation (chapter 3) are saved in the App for wavelength calibration.

4.2.2 Wireless communication with the server

Data collected by the App are wirelessly transmitted to the server through remote access with IP address. Data analysis are performed in the remote server where the image processing algorithms and Monte Carlo model are loaded. A custom tool named “SmartME Uploader” was developed and installed on the server to ensure a smooth connection between the SmartME and the server. Figure 4-7 shows the interface of the SmartME uploader software. To create a connection between the device and server, IP address and port number should be typed into the App, and a user account of the operator

should be created. Once the connection is established, data files will be uploaded to the server in real-time whenever a measurement is taken.



Figure 4-7: SmartME remote server

It takes less than 1 second for the App to transmit one data file to the server. A message will pop up on the server once the data files (image and text file) are successfully received. In the meantime, the successful data reception activates data processing modules. With the help of the fast Monte Carlo model, the inversion takes less than a second to extract the optical properties of the measured diffuse reflectance. The processed results are saved in the server and also sent back to the SmartME device for display. Figure 4-8 presents the results displayed in the App that are processed by the remote server. On the measurement page, the real-time display of the results for the most recent measurement is designed to disappear in 5 seconds. However, the results of all the analyses are saved in the App and available for browsing.

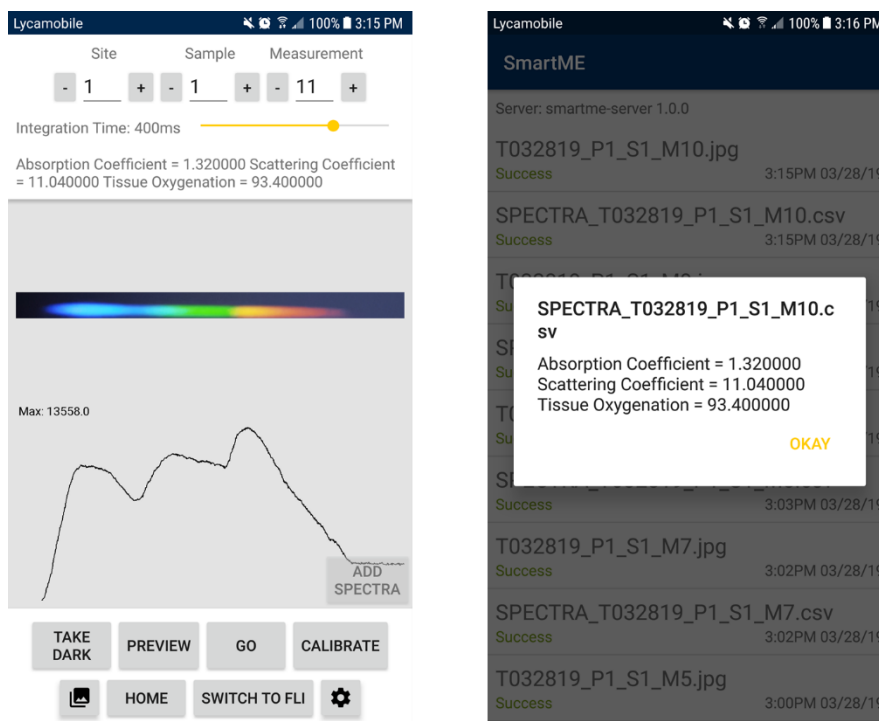


Figure 4-8: Display of results in the App

Left: the real-time display of the data for current measurement disappears in 5 seconds or overwritten by the next measurement. Right: results files are also saved in the App.

4.3 PERFORMANCE VERIFICATION AND IN VIVO STUDY

4.3.1 System performance characterization

The performance of the combined SmartME has been characterized using similar procedures described in Chapter 2 and 3. Briefly, the spatial resolution of the smartphone FLI was estimated by taking fluorescence images of a 1951 USAF resolution test target. The smallest pair of lines in the fluorescence images that can be successfully resolved was Element 2 in Group 7. Thus, the spatial resolution was estimated to be about $3.5 \mu\text{m}$, which is high enough to resolve the cell nuclei.

For the DRS, wavelength calibration using neon and krypton lamps was conducted. The resolving power was estimated to be 2 nm based on the FWHM method.

Liquid phantom experiments combined with the fast Monte Carlo inverse model were conducted to test the accuracy in measuring diffuse reflectance. The inversion process was repeated 14 times (for all 14 phantoms), in each inversion one phantom was selected as a reference to analyze all phantoms.^[151] The percent errors, which are the difference between the extracted and expected values in μ_a and μ'_s divided by the expected values, were computed. An averaged accuracy of 95% in measuring diffuse reflectance was obtained. Among all phantoms, the phantom #9 was selected as the reference to calibrate the SmartME DRS channel for tissue measurements because it yielded the smallest error.

4.3.2 *Ex vivo* measurements of biological samples

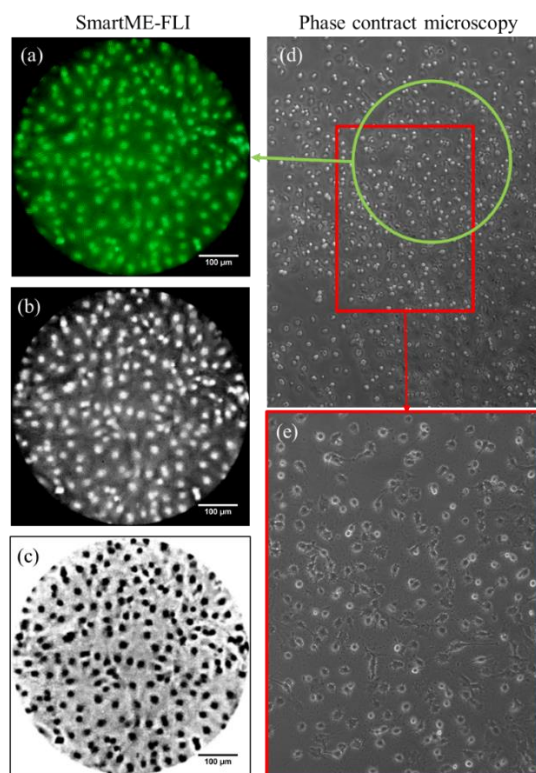


Figure 4-9: Fluorescence images of HeLa cells

(a)-(c): Raw and processed fluorescence images taken by SmartME FLI module. (d) and (e): phase contrast images taken by a microscope. Because the fiber-optic probe touched the cells during measurement, the cell distribution in the circled-out area (green) of the microscopic image was not exactly the same as it appeared in the fluorescence image.

Monolayer HeLa cells (cervical cancer cell line) grown in a disk was imaged using the SmartME-FLI. Proflavine at a concentration of 0.01% (wt/vol in PBS) was applied on the surface of the cells. The fiber-optic probe held on a Z-stage was adjusted until a clear image can be obtained. The end of the probe had a gentle contact with the cells. Figure 4-9(a)-(c) are raw and processed fluorescence images collected from the HeLa cells using the SmartME and miniature fiber-optic probe. The cell nuclei are clearly visualized with some background fluorescence, which is attributed to the excessive proflavine in the culture medium. Figure 4-9(d) and (e) are two phase contrast images at different magnifications. To further verify the capability of the device in imaging tissue samples, tumor tissue harvested from a nude rat xenograft model (breast cancer 4T1, epithelial) was imaged *in vitro* using the SmartME FLI. As shown in Figure 4-10, the cancer cells are densely packed. The tumor tissue is highly hypoxic (almost white in color) leads to a lot of reflectance background lights. Besides, fluorescence light from the cells of deeper layers is scattered by the surface layer. Therefore, the contrast of the fluorescence image of the tumor tissue was not as good as the contrast of monolayer cell line.

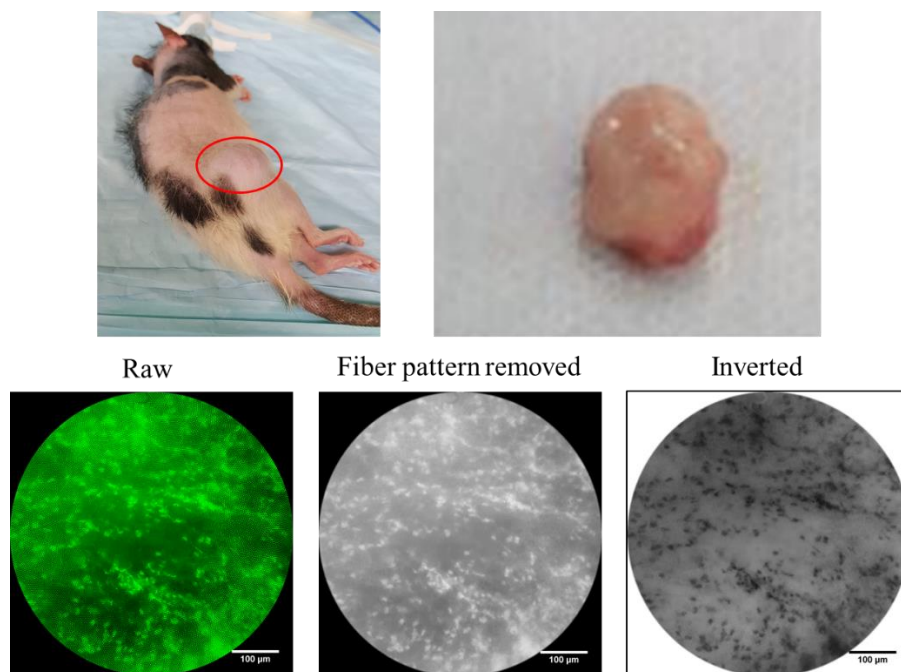


Figure 4-10: Fluorescence image of tumor tissue *in vitro*

4.3.3 *In vivo* measurements of healthy oral tissue

To test the feasibility of the SmartME for quantitative characterization of epithelial tissue properties, three types of healthy oral mucosa tissues, including labial mucosa, gingival tissue and tongue dorsum, from a healthy human volunteer were imaged *in vivo*. The experiment was conducted on the researcher himself. The subject in this self-experiment fully understood the procedures and gave his consent to participate in the experiment voluntarily. Exempt determination was received from Marquette University's Institutional Review Board (IRB). All methods were performed in accordance with the relevant guidelines and regulations of the institution. Before the optical measurements, the volunteer was asked to rinse his mouth with a 0.9% saline solution. The SmartME endoscope was cleaned using 2% chlorhexidine digluconate in ethanol. Eight random sites were imaged from both labial mucosa and tongue dorsum tissues, while five random

sites were measured from gingival tissues. All measurements were taken under dimmed room light. To take a measurement, the endoscope was handheld and brought in gentle contact with the tissue. Diffuse reflectance spectra were collected by turning on the white LED and switching the SmartME App to the DRS mode. A diffuse reflectance spectrum was taken from a diffuse reflectance standard puck (Spectralon, Labsphere) for calibration purpose following the tissue measurements. A background spectrum was also collected and subtracted from all tissue spectra and the puck spectrum.

Immediately following the DRS measurements, the surface of the same tissue sites was topically stained using cotton swabs with proflavine at a concentration of 0.01% wt/vol (in PBS) for 15 seconds, and then rinsed with PBS to remove excessive fluorescence dye. Fluorescence images were taken by turning on the blue LED and switching the App to the FLI mode. Each of the twenty-one tissue sites was imaged five times by slightly shifting the endoscope within the area of interest, resulting in a total of 105 diffuse reflectance spectra and 105 fluorescence images. All the spectral data and fluorescence images were saved in the App and wirelessly transferred to the remote server for further processing to extract the biological properties using the methods described below.

The image reconstruction method discussed in chapter 2 has been employed using MATLAB to eliminate the fiber pattern artifacts in the fluorescence images. The imaging area of the fiber bundle was defined as the region of interest (ROI) and circularly cropped out of the whole raw image. The intensity within each fiber has a Gaussian distribution. Therefore, the intensity at the center pixel of each fiber (which occupies multiple pixels on the smartphone camera) represents the fluorescence intensity collected by that fiber

and is assigned to the neighboring pixels within the fiber to construct a comb structure free image. The image was then converted to a binary image in ImageJ to calculate the N/C for the selected ROI using the built-in particle analyzer.

The fast Monte Carlo inverse model of reflectance discussed in Chapter 3 was loaded in the remote server to analyze the diffuse reflectance spectra. The diffuse reflectance spectra of the liquid tissue phantoms were used to extract the μ_a and μ'_s between 450 nm and 630 nm. The tissue hemoglobin concentrations were computed from the extracted μ_a using the Beer-Lambert law. Phantom #9 of the phantom experiment was selected as the reference to invert the diffuse reflectance spectra of the oral tissues.

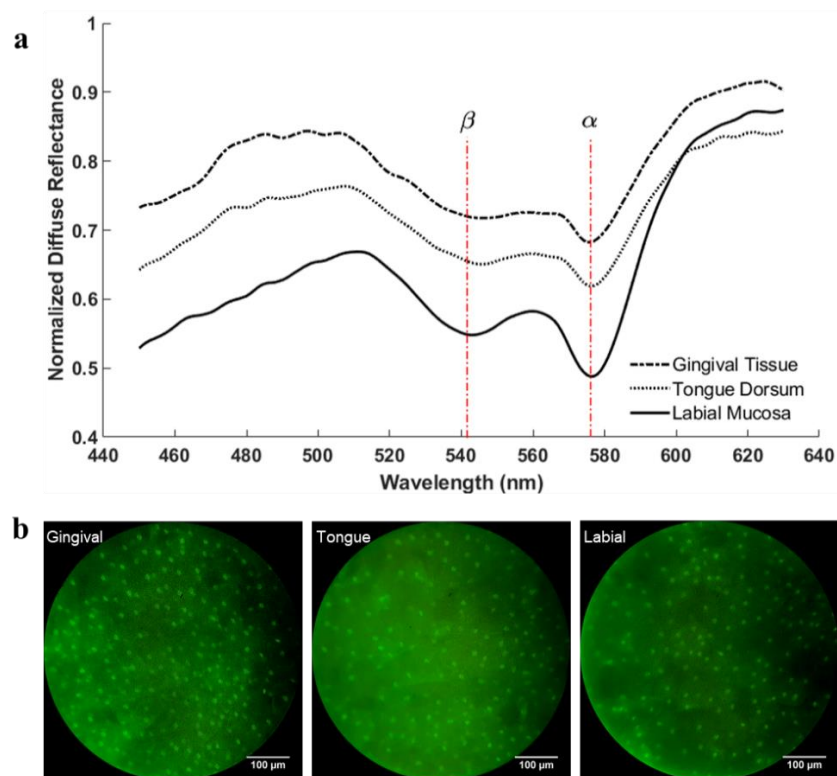


Figure 4-11: DRS and FLI measurements of healthy oral tissues

(a) Normalized representative diffuse reflectance spectra and (b) typical raw fluorescence images measured from healthy gingival tissue, tongue dorsum and labial mucosa *in vivo*.

Figure 4-11(a) shows representative diffuse reflectance spectra from three healthy oral sites that are normalized by (point-by-point) dividing the puck spectrum. The two major absorption bands (α and β bands) of oxyhemoglobin are clearly visible in the spectra. The measured spectra of the three types of oral tissue are different from each other in shape and intensity, representing the difference in their underlying physiological and morphological characteristics. Typical raw fluorescence images taken from the three oral tissues are shown in Figure 4-11(b). The bright spots in the images represent the nuclei instead of the cells because proflavine selectively labels the cell DNA.

Reduced scattering coefficients μ'_s and total hemoglobin concentrations (THC) were extracted from the tissue spectra using the Monte Carlo inverse model. Assumed that both the μ'_s and THC are normally distributed, Student's t-tests were performed using Minitab to test if there are significant differences among the three tissue types. Interval plots using the individual standard deviation of extracted THC and μ'_s are presented in Figure 4-12(a) and (b), respectively. Each dot in the plots represents the average of 5 repeated measurements taken from the same tissue site. Although the optical properties vary from site to site even for the same tissue type, the variation within each group of tissue type is generally smaller compared to differences between different tissue types. The extracted THC of labial mucosa is significantly higher than that of gingival and tongue tissues ($P < 0.001$). The THC of gingival and tongue tissues are also significantly different from each other ($p < 0.003$). While the extracted μ'_s of the tongue dorsum is significantly lower than gingival tissue and labial mucosa, there is no significant difference between gingival tissue and labial mucosa ($P = 0.60$).

The reconstructed, fiber pattern free fluorescence images for three representative tissues are presented in Figure 4-12(c). The inverted and enhanced images were further processed to extract the N/Cs for the tissues. The average N/C (overall sites of the same tissue type) is 4.4 ± 0.6 (%) for gingival tissue, 4.1 ± 0.5 (%) for tongue dorsum and 3.9 ± 0.8 (%), for labial mucosa. Consequently, the results suggest that the intervention of DRS measurements can provide diagnostically complementary information about the samples in question when it has difficulty in differentiating the tissues by using FLI alone.

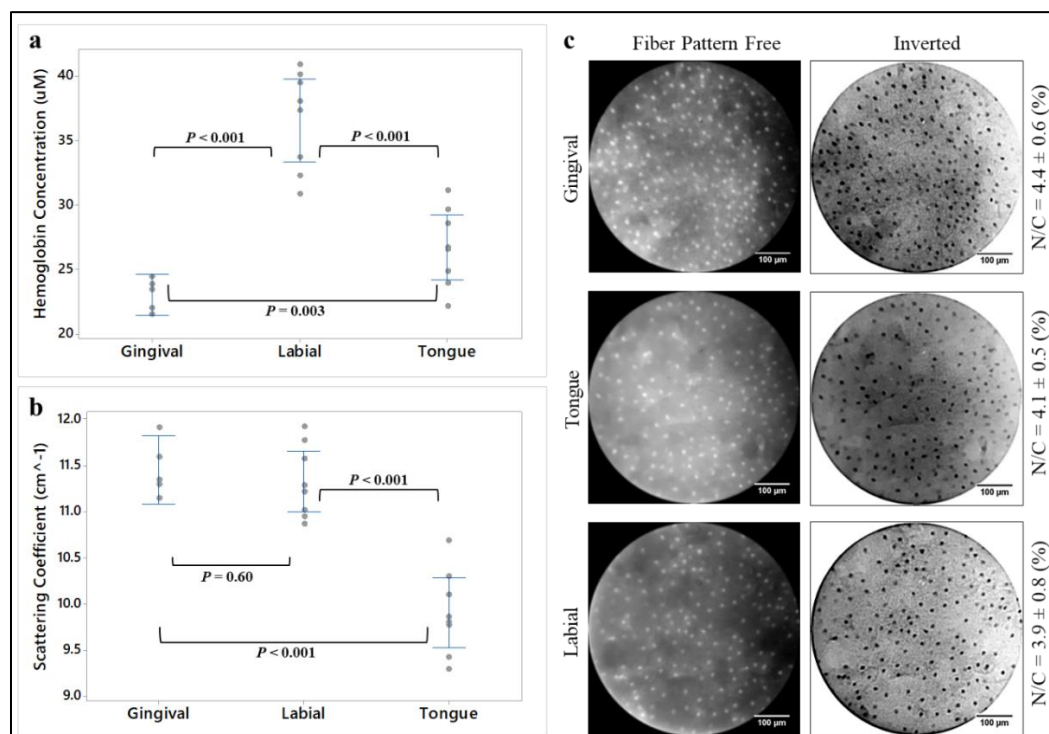


Figure 4-12: Quantitative analysis of tissue properties

(a) Interval plots of extracted total hemoglobin concentration and (b) extracted wavelength-averaged reduced scattering coefficient for three oral tissue types (gingival, labial and tongue). Each dot represents an average of 5 repeated measurements from the same tissue site. P-values are calculated using two-sided Student's t-test at a significance level of 5%; (c) Representative, fiber pattern removed fluorescence images of the three oral tissues and the inverted images used for N/C calculation.

4.4 DISCUSSION

We have developed a dual-modality smartphone fiber-optic microendoscope that integrates quantitative DRS and high-resolution FLI into a portable, cost-effective and globally connected device. The SmartME can noninvasively quantify the optical properties, hemoglobin concentrations and the nuclear-cytoplasmic ratio of epithelial tissues. The ability to measure these tissue parameters at low cost has a significant impact on epithelial cancer and pre-cancer detection in low-resource settings. In a clinical study for cervical cancer detection using DRS conducted by Chang *et al.*^[79], a significant increase in THC and a decrease in mean μ'_s were observed in high-grade neoplasia compared to low-grade lesions and normal tissues. Hornung *et al.*^[163] and Georgakoudi *et al.*^[100] also observed a decreasing trend in μ'_s ($P = 0.16$) in high-grade neoplasia using spectroscopy. In a review article by Thekkek *et al.*^[51], DRS was shown to have achieved sensitivities and specificities in the ranges of 83 – 92% and 80 – 90% for cervical precancer detection. High-resolution FLI also allows differentiating high-grade neoplastic changes from their low-grade and normal counterparts using the N/C. For example, a sensitivity of 86% and specificity of 87% were achieved using N/C in differentiating high-grade lesions from non-neoplastic cervical tissues in 26 cervical cancer patients by Quinn *et al.*^[53]. A large advantage of the SmartME system is that it combines the benefits of both FLI and DRS to provide complementary information that can be used to improve the sensitivity and specificity in differentiating different epithelial tissue types. Therefore, the SmartME has great potential to be used for imaging of neoplastic changes in oral mucosa and cervical tissues as well as gastrointestinal tract tracts.

The implementation of the SmartME system is intended to provide a cost-effective solution for precancerous screening in resource-limited settings. The integration of optical imaging technologies on a smartphone platform can significantly reduce the cost, weight and size, while maintains the high performance in the meantime. The total cost of the current SmartME device is less than \$2500, among which the major costs are from the imaging fiber bundle, light sources and fluorescence filters. The cost may be further reduced by batch ordering and mass production, making it even more affordable to LMIC. More importantly, the App developed for the SmartME has the ability to send the images collected on site to a remote server for diagnostic analysis. The smartphone-based diagnosis could potentially be used as a point-of-care device for telemedicine applications in LMIC where multiple clinical visits are not feasible and centralized laboratories do not exist.

CHAPTER 5: CONCLUSIONS AND SUGGESTED FUTURE WORK

5.1 SUMMARY

The scope of this dissertation was to design and develop a cost-effective smartphone-based endoscope system that can perform both high-resolution fluorescence imaging and diffuse reflectance spectroscopy for early detection of cervical neoplastic changes. Figure 5-1 shows the development and prototyping history of the device.

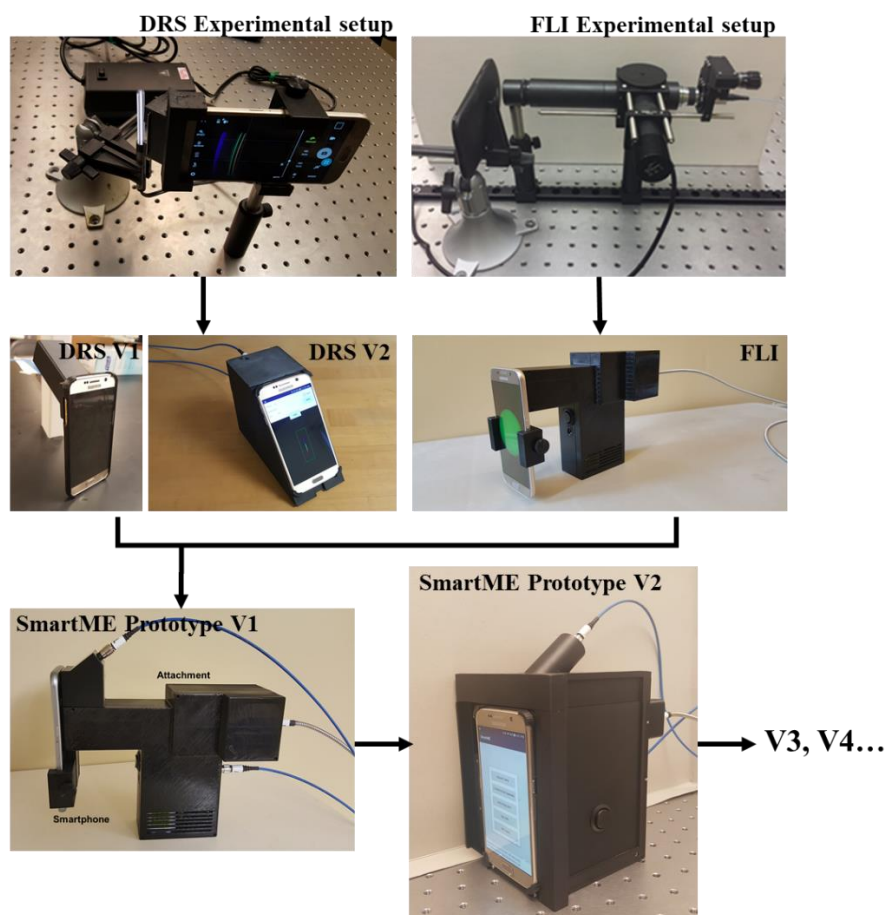


Figure 5-1: The development history of SmartME

In Chapter 2, development procedures and performance characterization of the smartphone-based fluorescence imaging device were discussed. The results showed that

the imaging resolution (3.5 μm) and contrast of the device were as good as the benchtop system that had been verified in clinical studies, while the smartphone-based device was more cost-effective and easier to use. Chapter 3 presented the design and development of a fiber-optic smartphone-based spectrometer. While the spectrometer was very compact, the performance of the device, including optical resolving power (2 nm) and accuracy (95%) in measuring diffuse reflectance, was comparable to a commercial spectroscopy system. Chapter 4 further combined the two modalities onto the smartphone platform to obtain a dual-modality device SmartME. The rear camera was shared by two modules due to the hardware limitations of the front-face camera. Biological samples including monolayer HeLa cells and *ex vivo* tumor tissues (4T1) were imaged using the SmartME. The results showed that cell nuclei were clearly visualized when fluorescence agent proflavine was applied on the sample surfaces. Beyond this, an *in vivo* study of healthy human oral tissue using the SmartME was conducted to verify its capability to quantitatively characterize the epithelial tissue properties. Three types of normal oral mucosa tissues, including labial mucosa, gingival tissue and tongue dorsum, were measured by both modalities. Optical and tissue properties such as scattering coefficient, total hemoglobin concentration and nuclear-cytoplasmic ratio were extracted from the diffuse reflectance spectra and fluorescence images using a fast Monte Carlo inverse model and image processing algorithms. The results showed that the measured spectra of the three types of oral tissue are significantly different from each other in shape and intensity due to different absorption and scattering properties, representing the difference in their underlying physiological and morphological characteristics. Since all measurements were taken on normal tissues, the N/Cs were similar across all three types

of tissues, which met our expectation. However, with the help of DRS, tissue types were successfully distinguished from each other that otherwise impossible if solely based on N/Cs obtained from FLI.

5.2 SIGNIFICANCE OF THIS WORK

From the 1990s, improving the medical conditions of all human beings and scaling healthcare innovations worldwide have now become the consensus of people from all over the world. However, as stated in a report by WHO in 2003, quote:

“... a significant proportion of the world’s population, especially in developing countries, has yet to derive much benefit from innovations that are commonplace elsewhere. The reasons range from weak supply systems to unaffordable prices. The factors that drive innovation are often biased against conditions that disproportionately affect the populations of developing countries. ... Innovation to address conditions primarily affecting poor people is held back by a combination of market failure and underinvestment by the public sector. The process of bringing a new product to the market is both expensive and lengthy. ...”^[164]

While there is still a long way to go to improve the healthcare conditions in LMICs, we are committed to developing medical devices that are suitable and practicable for LMICs. Figure 5-2 shows how the SmartME can be combined with VIA/VIAM to screen and detect cervical neoplastic changes in LMICs. Without the SmartME, all abnormal lesions identified by VIA/VIAM (low specificity) will be biopsied, leading to a large number of unnecessary biopsies. With the SmartME, only the patients with the highest likelihood of having CIN2+ will be biopsied, thus reducing the number of unnecessary biopsies that might otherwise be taken for diagnosis. In the long-term, if this

combined strategy is proven to be highly specific, it can enable a see-and-treat paradigm in which a diagnosis of CIN2+ could immediately be followed by cryotherapy or LEEP, thereby preventing the need for biopsy and multiple clinical visits.

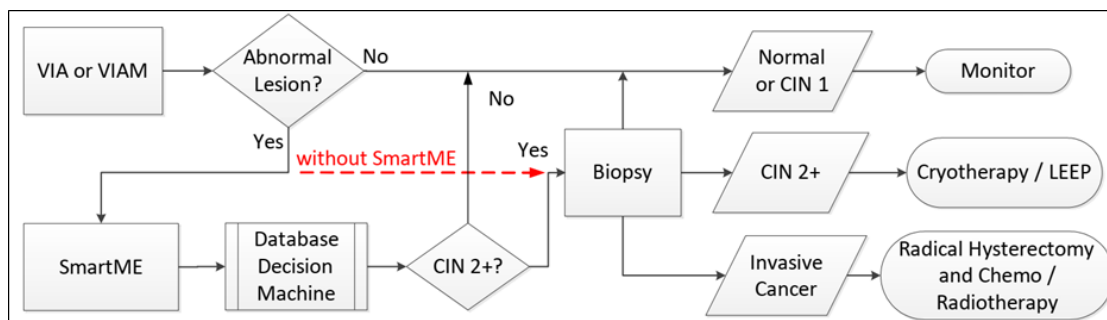


Figure 5-2: Benefits of using SmartME in clinical applications

This study is an application of the translational research concept that takes advantage of recent advancements in high-resolution fluorescence imaging, optical spectroscopy and Mobile Internet technology, and aims at improving or transforming current cancer diagnostic practice in LMICs. The work is scientifically innovative in three aspects: hardware, software, and optical biomarker discovery. The compact integration of FLI and DRS into a miniature fiber-optic endoscope on to a smartphone platform is a key innovation, which enables high-resolution imaging and quantitative endoscopy to be affordable, portable and easy-to-use. Another innovation is that the smartphone App not only allows data collection but also connects the device and operator in a low-resource setting to a high-performance server loaded with custom image/spectral processing and diagnostic software as well as experienced personnel in a developed area. This new solution may transform the current on-site cancer diagnosis in LMICs to a cloud-based online smart diagnosis paradigm. A third innovation is the discovery of

biomarkers that best differentiate high-grade from low-grade lesions and their normal/benign counterparts if the device is successfully validated in the clinical study.

5.2 FUTURE INVESTIGATIONS

We note that the current study on the SmartME is subject to several limitations. First, the effect of acetowhitening phenomena on the FLI and DRS measurements remains unstudied. Studies have shown that acetic acid increases the backscattering of cell nuclei, which leads to images with increased contrast under confocal microscopy.^[11,29] Other studies reported that the backscattering from cytoplasmic fraction dominates backscattering from nuclear or mitochondrial fractions after application of acetic acid.^[34] If both the reported findings mentioned above are correct, it is safe to assume that the contrast of FLI measurements will not be affected much because the fluorescence dye selectively stains the cell nuclei. However, the increased scattering intensity from the cytoplasmic fraction will definitely increase the scattering readings if DRS measurements are taken immediately after acetic acid application. Using scattering coefficient to differentiate tissue types may become less effective. Consequently, comparative experiments in a clinical setting should be conducted to fully investigate whether acetowhitening effects will significantly affect the measurements taken by SmartME device. Alternatively, since most acetowhitening effect starts to decay in 5 minutes after acetic acid application^[28,31], a standardized procedure could be developed in which SmartME measurements are only performed after acetowhitening decay to bypass its effect. Test accuracy is still the most important factor, given that the testing speed and comfort are not significantly reduced.

Second, because only one healthy subject was measured in our *in vivo* study, the conclusions and findings may not be extended to all subjects. Many factors, including race, gender, age, diet habit and physical conditions, may lead to higher inter-subject variations. Future clinical studies that include both normal/benign tissue and cancer or precancer are necessary to fully test its efficacy in early detection of cervical neoplastic changes. We have recently contacted hospitals in developing countries in an attempt to establish a collaborative clinical trial.

Finally, motion artifacts and probe-tissue contact pressure may also contribute to differences in the tissue optical properties from site to site because it is challenging to maintain a consistent pressure applied to the tissue by the endoscope.^[75,165-167] Therefore, device optimization both in hardware and software, such as including a pressure sensor on the tip of the endoscope, adding another imaging modality or improving the communication establishment between the device and the server, may be necessary to improve the reliability and consistency.

BIBLIOGRAPHY

- [1] Schiffman, M., Castle, P. E., Jeronimo, J., Rodriguez, A. C., & Wacholder, S. (2007). Human papillomavirus and cervical cancer. *Lancet*, 370(9590), 890-907. doi:Doi 10.1016/S0140-6736(07)61416-0
- [2] Walboomers, J. M. M., Jacobs, M. V., Manos, M. M., Bosch, F. X., Kummer, J. A., Shah, K. V., . . . Munoz, N. (1999). Human papillomavirus is a necessary cause of invasive cervical cancer worldwide. *Journal of Pathology*, 189(1), 12-19. doi:Doi 10.1002/(Sici)1096-9896(199909)189:1<12::Aid-Path431>3.0.Co;2-F
- [3] Murillo, R., Herrero, R., Sierra, M. S., & Forman, D. (2016). Cervical cancer in Central and South America: Burden of disease and status of disease control. *Cancer epidemiology*, 44, S121-S130.
- [4] Munoz, N., Castellsagué, X., de González, A. B., & Gissmann, L. (2006). HPV in the etiology of human cancer. *Vaccine*, 24, S1-S10.
- [5] de Sanjose, S., Quint, W. G., Alemany, L., Geraets, D. T., Klaustermeier, J. E., Lloveras, B., . . . Shin, H.-R. (2010). Human papillomavirus genotype attribution in invasive cervical cancer: a retrospective cross-sectional worldwide study. *The lancet oncology*, 11(11), 1048-1056.
- [6] Bray, F., Ferlay, J., Soerjomataram, I., Siegel, R. L., Torre, L. A., & Jemal, A. (2018). Global cancer statistics 2018: GLOBOCAN estimates of incidence and mortality worldwide for 36 cancers in 185 countries. *CA: a cancer journal for clinicians*.
- [7] Novikova, T. (2017). Optical techniques for cervical neoplasia detection. *Beilstein journal of nanotechnology*, 8(1), 1844-1862.
- [8] Halperin, E. C., Brady, L. W., Perez, C. A., & Wazer, D. E. (2013). *Perez & Brady's principles and practice of radiation oncology*: Lippincott Williams & Wilkins.
- [9] Devesa, S. S., Silverman, D. T., Young Jr, J. L., Pollack, E. S., Brown, C. C., Horm, J. W., . . . Fraumeni Jr, J. F. (1987). Cancer incidence and mortality trends among whites in the United States, 1947-84. *Journal of the National Cancer Institute*, 79(4), 701-770.
- [10] Zink, D., Fischer, A. H., & Nickerson, J. A. (2004). Nuclear structure in cancer cells. *Nature Reviews Cancer*, 4(9), 677.

- [11] Yang, L., Liu, W.-T., Wu, H., Wang, C., Ping, B., & Shi, D.-R. (2011). Separation of normal and premalignant cervical epithelial cells using confocal light absorption and scattering spectroscopic microscopy ex vivo. *BioMed Research International*, 2011.
- [12] Divya Rani, M., Narasimha, A., Harendra Kumar, M., & Sheela, S. (2014). Evaluation of Pre-Malignant and Malignant Lesions in Cervico Vaginal (Pap) Smears by Nuclear Morphometry. *Journal of clinical and diagnostic research: JCDR*, 8(11), FC16.
- [13] Zhao, M., Chen, L., Bian, L., Zhang, J., Yao, C., & Zhang, J. (2015). Feature quantification and abnormal detection on cervical squamous epithelial cells. *Computational and mathematical methods in medicine*, 2015.
- [14] Koliopoulos, G., Arbyn, M., Martin-Hirsch, P., Kyrgiou, M., Prendiville, W., & Paraskevaidis, E. (2007). Diagnostic accuracy of human papillomavirus testing in primary cervical screening: a systematic review and meta-analysis of non-randomized studies. *Gynecologic Oncology*, 104(1), 232-246.
- [15] Chang, V. T.-C., Merisier, D., Yu, B., Walmer, D. K., & Ramanujam, N. (2011). *Calibration schemes of a field-compatible optical spectroscopic system to quantify neovascular changes in the dysplastic cervix*. Paper presented at the Design and Quality for Biomedical Technologies IV.
- [16] Arrossi, S., Sankaranarayanan, R., & Parkin, D. M. (2003). Incidence and mortality of cervical cancer in Latin America. *Salud pública de México*, 45, 306-314.
- [17] Soler, M. E., Gaffikin, L., & Blumenthal, P. D. (2000). Cervical cancer screening in developing countries. *Primary care update for Ob/Gyns*, 7(3), 118-123.
- [18] Chang, V. T.-C., Merisier, D., Yu, B., Walmer, D. K., & Ramanujam, N. (2011). Towards a field-compatible optical spectroscopic device for cervical cancer screening in resource-limited settings: effects of calibration and pressure. *Optics Express*, 19(19), 17908-17924.
- [19] Sankaranarayanan, R., Basu, P., Wesley, R. S., Mahe, C., Keita, N., Mbalawa, C. C. G., . . . Nacoulma, M. (2004). Accuracy of visual screening for cervical neoplasia: Results from an IARC multicentre study in India and Africa. *International Journal of Cancer*, 110(6), 907-913.
- [20] Pollack, A., & Tsu, V. (2005). Preventing cervical cancer in low-resource settings: Building a case for the possible. *International Journal of Gynecology & Obstetrics*, 89, S1-S3.

- [21] Goldie, S. J., Gaffikin, L., Goldhaber-Fiebert, J. D., Gordillo-Tobar, A., Levin, C., Mahé, C., & Wright, T. C. (2005). Cost-effectiveness of cervical-cancer screening in five developing countries. *New England Journal of Medicine*, 353(20), 2158-2168.
- [22] Sankaranarayanan, R., Nene, B. M., Shastri, S. S., Jayant, K., Muwonge, R., Budukh, A. M., . . . Kothari, A. (2009). HPV screening for cervical cancer in rural India. *New England Journal of Medicine*, 360(14), 1385-1394.
- [23] Zeferino, L. C., & Derchain, S. F. (2006). Cervical cancer in the developing world. *Best Practice & Research Clinical Obstetrics & Gynaecology*, 20(3), 339-354.
- [24] Gaffikin, L., Lauterbach, M., & Blumenthal, P. D. (2003). Performance of visual inspection with acetic acid for cervical cancer screening: a qualitative summary of evidence to date. *Obstetrical & gynecological survey*, 58(8), 543-550.
- [25] of Zimbabwe, U., & Project, J. C. C. (1999). Visual inspection with acetic acid for cervical-cancer screening: test qualities in a primary-care setting. *The Lancet*, 353(9156), 869-873.
- [26] Anderson, M. C. (1992). *A text and atlas of integrated colposcopy: for colposcopists, histopathologists and cytologists*: Chapman and Hall.
- [27] Lambert, R., Rey, J., & Sankaranarayanan, R. (2003). Magnification and chromoscopy with the acetic acid test. *Endoscopy*, 35(05), 437-445.
- [28] Wu, T. T., Qu, J. Y., Cheung, T. H., Yim, S. F., & Wong, Y. F. (2005). Study of dynamic process of acetic acid induced-whitening in epithelial tissues at cellular level. *Optics Express*, 13(13), 4963-4973.
- [29] Collier, T., Shen, P., de Pradier, B., Sung, K.-B., Richards-Kortum, R., Malpica, A., & Follen, M. (2000). Near real time confocal microscopy of amelanotic tissue: dynamics of aceto-whitening enable nuclear segmentation. *Optics Express*, 6(2), 40-48.
- [30] Collier, T., Lacy, A., Richards-Kortum, R., Malpica, A., & Follen, M. (2002). Near real-time confocal microscopy of amelanotic tissue: detection of dysplasia in ex vivo cervical tissue. *Academic radiology*, 9(5), 504-512.
- [31] Gutiérrez-Fragoso, K., Acosta-Mesa, H. G., Cruz-Ramírez, N., & Hernández-Jiménez, R. (2017). Optimization of classification strategies of acetowhite temporal patterns towards improving diagnostic performance of colposcopy. *Computational and mathematical methods in medicine*, 2017.

- [32] Pogue, B. W., Kaufman, H., Zelenchuk, A. R., Harper, W., Burke, G. C., Burke, E. E., & Harper, D. M. (2001). Analysis of acetic acid-induced whitening of high-grade squamous intraepithelial lesions. *Journal of Biomedical Optics*, 6(4), 397-404.
- [33] Balas, C. (2001). A novel optical imaging method for the early detection, quantitative grading, and mapping of cancerous and precancerous lesions of cervix. *IEEE transactions on biomedical engineering*, 48(1), 96-104.
- [34] Wu, T. T., & Qu, J. Y. (2007). Assessment of the relative contribution of cellular components to the acetowhitening effect in cell cultures and suspensions using elastic light-scattering spectroscopy. *Applied Optics*, 46(21), 4834-4842.
- [35] Schmid-Saugeon, P., Pitts, J. D., Kaufman, H. B., Zelenchuk, A., & Harper, D. M. (2004). Time-resolved imaging of cervical acetowhitening. *Draft paper*.
- [36] Jeronimo, J., Bansil, P., Lim, J., Peck, R., Paul, P., Amador, J. J., . . . Satyanarayana, L. (2014). A multicountry evaluation of careHPV testing, visual inspection with acetic acid, and papanicolaou testing for the detection of cervical cancer. *International Journal of Gynecological Cancer*, 24(3), 576.
- [37] Pankaj, S., Kumari, A., Kumari, S., Choudhary, V., Kumari, J., Kumari, A., & Nazneen, S. (2018). Evaluation of Sensitivity and Specificity of Pap Smear, LBC and HPV in Screening of Cervical Cancer. *Indian Journal of Gynecologic Oncology*, 16(3), 49.
- [38] Saleh, H. S. (2014). Can visual inspection with acetic acid be used as an alternative to Pap smear in screening cervical cancer? *Middle East Fertility Society Journal*, 19(3), 187-191.
- [39] Ardahan, M., & Temel, A. B. (2011). Visual inspection with acetic acid in cervical cancer screening. *Cancer Nursing*, 34(2), 158-163.
- [40] Gallwas, J. K., Turk, L., Stepp, H., Mueller, S., Ochsenkuehn, R., Friese, K., & Dannecker, C. (2011). Optical coherence tomography for the diagnosis of cervical intraepithelial neoplasia. *Lasers in surgery and medicine*, 43(3), 206-212.
- [41] Fujimoto, J. G., Pitris, C., Boppart, S. A., & Brezinski, M. E. (2000). Optical coherence tomography: an emerging technology for biomedical imaging and optical biopsy. *Neoplasia*, 2(1-2), 9-25.
- [42] Zuluaga, A. F., Follen, M., Boiko, I., Malpica, A., & Richards-Kortum, R. (2005). Optical coherence tomography: a pilot study of a new imaging technique for

noninvasive examination of cervical tissue. *American journal of obstetrics and gynecology*, 193(1), 83-88.

- [43] Gallwas, J., Jalilova, A., Ladurner, R., Kolben, T. M., Kolben, T., Ditsch, N., . . . Dannecker, C. (2017). Detection of cervical intraepithelial neoplasia by using optical coherence tomography in combination with microscopy. *Journal of Biomedical Optics*, 22(1), 016013.
- [44] Liu, Z., Belinson, S. E., Li, J., Yang, B., Wulan, N., Tresser, N. J., . . . Zhou, Y. (2010). Diagnostic efficacy of real-time optical coherence tomography in the management of preinvasive and invasive neoplasia of the uterine cervix. *International Journal of Gynecologic Cancer*, 20(2), 283-287-283-287.
- [45] Almond, L. M., Hutchings, J., Lloyd, G., Barr, H., Shepherd, N., Day, J., . . . Stone, N. (2014). Endoscopic Raman spectroscopy enables objective diagnosis of dysplasia in Barrett's esophagus. *Gastrointestinal endoscopy*, 79(1), 37-45.
- [46] Bergholt, M., Zheng, W., Lin, K., Ho, K., Teh, M., Yeoh, K., . . . Huang, Z. (2011). In vivo diagnosis of esophageal cancer using image-guided Raman endoscopy and biomolecular modeling. *Technology in cancer research & treatment*, 10(2), 103-112.
- [47] Ellis, D. I., & Goodacre, R. (2006). Metabolic fingerprinting in disease diagnosis: biomedical applications of infrared and Raman spectroscopy. *Analyst*, 131(8), 875-885.
- [48] Utzinger, U., Heintzelman, D. L., Mahadevan-Jansen, A., Malpica, A., Follen, M., & Richards-Kortum, R. (2001). Near-infrared Raman spectroscopy for in vivo detection of cervical precancers. *Applied spectroscopy*, 55(8), 955-959.
- [49] Krishna, C. M., Prathima, N., Malini, R., Vadhiraaja, B., Bhatt, R. A., Fernandes, D. J., . . . Kartha, V. (2006). Raman spectroscopy studies for diagnosis of cancers in human uterine cervix. *Vibrational Spectroscopy*, 41(1), 136-141.
- [50] Duraipandian, S., Zheng, W., Ng, J., Low, J. J., Ilancheran, A., & Huang, Z. (2012). Simultaneous fingerprint and high-wavenumber confocal Raman spectroscopy enhances early detection of cervical precancer in vivo. *Analytical chemistry*, 84(14), 5913-5919.
- [51] Thekkek, N., & Richards-Kortum, R. (2008). Optical imaging for cervical cancer detection: solutions for a continuing global problem. *Nature Reviews Cancer*, 8(9), 725.

- [52] Pierce, M. C., Guan, Y., Quinn, M. K., Zhang, X., Zhang, W.-H., Qiao, Y.-L., . . . Richards-Kortum, R. (2012). A pilot study of low-cost, high-resolution microendoscopy as a tool for identifying women with cervical precancer. *Cancer prevention research, canprevres.* 0221.2012.
- [53] Quinn, M. K., Bubi, T. C., Pierce, M. C., Kayembe, M. K., Ramogola-Masire, D., & Richards-Kortum, R. (2012). High-resolution microendoscopy for the detection of cervical neoplasia in low-resource settings. *PloS one*, 7(9), e44924.
- [54] Marcu, L., French, P. M., & Elson, D. S. (2014). *Fluorescence lifetime spectroscopy and imaging: principles and applications in biomedical diagnostics*: CRC Press.
- [55] Coda, S., Thompson, A. J., Kennedy, G. T., Roche, K. L., Ayaru, L., Bansi, D. S., . . . Dunsby, C. (2014). Fluorescence lifetime spectroscopy of tissue autofluorescence in normal and diseased colon measured ex vivo using a fiber-optic probe. *Biomedical optics express*, 5(2), 515-538.
- [56] Thompson, A. J., Coda, S., Sørensen, M. B., Kennedy, G., Patalay, R., Waitong-Brämning, U., . . . Bendsøe, N. (2012). In vivo measurements of diffuse reflectance and time-resolved autofluorescence emission spectra of basal cell carcinomas. *Journal of biophotonics*, 5(3), 240-254.
- [57] Zonios, G., Perelman, L. T., Backman, V., Manoharan, R., Fitzmaurice, M., Van Dam, J., & Feld, M. S. (1999). Diffuse reflectance spectroscopy of human adenomatous colon polyps in vivo. *Applied Optics*, 38(31), 6628-6637.
- [58] Lovat, L. B., Johnson, K., Mackenzie, G. D., Clark, B. R., Novelli, M. R., Davies, S., . . . Pickard, D. (2006). Elastic scattering spectroscopy accurately detects high grade dysplasia and cancer in Barrett's oesophagus. *Gut*, 55(8), 1078-1083.
- [59] Georgakoudi, I., Jacobson, B. C., Van Dam, J., Backman, V., Wallace, M. B., Müller, M. G., . . . Thomas, G. A. (2001). Fluorescence, reflectance, and light-scattering spectroscopy for evaluating dysplasia in patients with Barrett's esophagus. *Gastroenterology*, 120(7), 1620-1629.
- [60] Ge, Z., Schomacker, K. T., & Nishioka, N. S. (1998). Identification of colonic dysplasia and neoplasia by diffuse reflectance spectroscopy and pattern recognition techniques. *Applied spectroscopy*, 52(6), 833-839.
- [61] Dhar, A., Johnson, K. S., Novelli, M. R., Bown, S. G., Bigio, I. J., Lovat, L. B., & Bloom, S. L. (2006). Elastic scattering spectroscopy for the diagnosis of colonic lesions: initial results of a novel optical biopsy technique. *Gastrointestinal endoscopy*, 63(2), 257-261.

- [62] Peng, K., He, L., Wang, B., & Xiao, J. (2015). Detection of cervical cancer based on photoacoustic imaging—the in-vitro results. *Biomedical optics express*, 6(1), 135-143.
- [63] Li, C., Yang, J.-M., Chen, R., Yeh, C.-H., Zhu, L., Maslov, K., . . . Wang, L. V. (2014). Urogenital photoacoustic endoscope. *Optics letters*, 39(6), 1473-1476.
- [64] Ryu, I. S., Choi, S. H., Kim, D. H., Han, M. W., Roh, J. L., Kim, S. Y., & Nam, S. Y. (2013). Detection of the primary lesion in patients with cervical metastases from unknown primary tumors with narrow band imaging endoscopy: preliminary report. *Head & neck*, 35(1), 10-14.
- [65] Fujii, T., Nakamura, M., Kameyama, K., Saito, M., Nishio, H., Ohno, A., . . . Aoki, D. (2010). Digital colposcopy for the diagnosis of cervical adenocarcinoma using a narrow band imaging system. *International Journal of Gynecological Cancer*, 20(4), 605-610.
- [66] Fanfani, F., Rossitto, C., Fagotti, A., Gallotta, V., Gagliardi, M. L., & Scambia, G. (2011). Narrow-band imaging in laparoscopic management of cervical carcinoma. *Journal of minimally invasive gynecology*, 18(2), 146-147.
- [67] Hayashi, T., Muto, M., Hayashi, R., Minashi, K., Yano, T., Kishimoto, S., & Ebihara, S. (2010). Usefulness of narrow-band imaging for detecting the primary tumor site in patients with primary unknown cervical lymph node metastasis. *Japanese journal of clinical oncology*, 40(6), 537-541.
- [68] Gallwas, J., Turk, L., Friese, K., & Dannecker, C. (2010). Optical coherence tomography as a non-invasive imaging technique for preinvasive and invasive neoplasia of the uterine cervix. *Ultrasound in Obstetrics and Gynecology*, 36(5), 624-629.
- [69] Robichaux-Viehoever, A., Kanter, E., Shappell, H., Billheimer, D., Jones III, H., & Mahadevan-Jansen, A. (2007). Characterization of Raman spectra measured in vivo for the detection of cervical dysplasia. *Applied spectroscopy*, 61(9), 986-993.
- [70] Sung, K., Liang, C., Descour, M., Collier, T., Follen, M., Malpica, A., & Richards-Kortum, R. (2002). Near real time in vivo fibre optic confocal microscopy: sub-cellular structure resolved. *Journal of microscopy*, 207(2), 137-145.
- [71] Tan, J., Quinn, M., Pyman, J., Delaney, P., & McLaren, W. (2009). Detection of cervical intraepithelial neoplasia in vivo using confocal endomicroscopy. *BJOG: An International Journal of Obstetrics & Gynaecology*, 116(12), 1663-1670.

- [72] Pierce, M., Yu, D., & Richards-Kortum, R. (2011). High-resolution fiber-optic microendoscopy for in situ cellular imaging. *Journal of visualized experiments: JoVE*(47).
- [73] Grant, B. D., Schwarz, R. A., Quang, T., Schmeler, K. M., & Richards-Kortum, R. (2015). High-resolution microendoscope for the detection of cervical neoplasia. In *Mobile Health Technologies* (pp. 421-434): Springer.
- [74] Shin, D., Pierce, M. C., Gillenwater, A. M., Williams, M. D., & Richards-Kortum, R. R. (2010). A fiber-optic fluorescence microscope using a consumer-grade digital camera for in vivo cellular imaging. *PloS one*, 5(6), e11218.
- [75] Yu, B., Shah, A., Nagarajan, V. K., & Ferris, D. G. (2014). Diffuse reflectance spectroscopy of epithelial tissue with a smart fiber-optic probe. *Biomedical optics express*, 5(3), 675-689.
- [76] Skala, M. C., Palmer, G. M., Vrotsos, K. M., Gendron-Fitzpatrick, A., & Ramanujam, N. (2007). Comparison of a physical model and principal component analysis for the diagnosis of epithelial neoplasias in vivo using diffuse reflectance spectroscopy. *Optics Express*, 15(12), 7863-7875.
- [77] Schwarz, R. A., Gao, W., Daye, D., Williams, M. D., Richards-Kortum, R., & Gillenwater, A. M. (2008). Autofluorescence and diffuse reflectance spectroscopy of oral epithelial tissue using a depth-sensitive fiber-optic probe. *Applied Optics*, 47(6), 825-834.
- [78] Arifler, D., Schwarz, R. A., Chang, S. K., & Richards-Kortum, R. (2005). Reflectance spectroscopy for diagnosis of epithelial precancer: model-based analysis of fiber-optic probe designs to resolve spectral information from epithelium and stroma. *Applied Optics*, 44(20), 4291-4305.
- [79] Chang, V. T.-C., Cartwright, P. S., Bean, S. M., Palmer, G. M., Bentley, R. C., & Ramanujam, N. (2009). Quantitative physiology of the precancerous cervix in vivo through optical spectroscopy. *Neoplasia*, 11(4), 325-332.
- [80] Mirabal, Y. N., Chang, S. K., Atkinson, E. N., Malpica, A., Follen, M., & Richards-Kortum, R. R. (2002). Reflectance spectroscopy for in vivo detection of cervical precancer. *Journal of Biomedical Optics*, 7(4), 587-595.
- [81] Arifler, D., MacAulay, C. E., Follen, M., & Richards-Kortum, R. R. (2006). Spatially resolved reflectance spectroscopy for diagnosis of cervical precancer: Monte Carlo modeling and comparison to clinical measurements. *Journal of Biomedical Optics*, 11(6), 064027.

- [82] Cardenas-Turanzas, M., Freeberg, J. A., Benedet, J., Atkinson, E. N., Cox, D. D., Richards-Kortum, R., . . . Cantor, S. B. (2007). The clinical effectiveness of optical spectroscopy for the in vivo diagnosis of cervical intraepithelial neoplasia: where are we? *Gynecologic Oncology*, *107*(1), S138-S146.
- [83] Freeberg, J. A., Benedet, J., MacAulay, C., West, L. A., & Follen, M. (2007). The performance of fluorescence and reflectance spectroscopy for the in vivo diagnosis of cervical neoplasia; point probe versus multispectral approaches. *Gynecologic Oncology*, *107*(1), S248-S255.
- [84] Yu, B., Ferris, D. G., Liu, Y., & Nagarajan, V. K. (2014). Emerging optical techniques for detection of oral, cervical and anal cancer in low-resource settings. *Austin J. Biomed. Eng.*, *1*(2), 1007.
- [85] Müller, M. G., Valdez, T. A., Georgakoudi, I., Backman, V., Fuentes, C., Kabani, S., . . . Dasari, R. R. (2003). Spectroscopic detection and evaluation of morphologic and biochemical changes in early human oral carcinoma. *Cancer: Interdisciplinary International Journal of the American Cancer Society*, *97*(7), 1681-1692.
- [86] Sharwani, A., Jerjes, W., Salih, V., Swinson, B., Bigio, I., El-Maaytah, M., & Hopper, C. (2006). Assessment of oral premalignancy using elastic scattering spectroscopy. *Oral oncology*, *42*(4), 343-349.
- [87] Amelink, A., Kaspers, O., Sterenborg, H., Van Der Wal, J., Roodenburg, J., & Witjes, M. (2008). Non-invasive measurement of the morphology and physiology of oral mucosa by use of optical spectroscopy. *Oral oncology*, *44*(1), 65-71.
- [88] Rahman, M., Chaturvedi, P., Gillenwater, A., & Richards-Kortum, R. R. (2008). Low-cost, multimodal, portable screening system for early detection of oral cancer. *Journal of Biomedical Optics*, *13*(3), 030502.
- [89] Stephen, M. M., Jayanthi, J. L., Unni, N. G., Kolady, P. E., Beena, V. T., Jeemon, P., & Subhash, N. (2013). Diagnostic accuracy of diffuse reflectance imaging for early detection of pre-malignant and malignant changes in the oral cavity: a feasibility study. *BMC cancer*, *13*(1), 278.
- [90] Wang, H.-W., Jiang, J.-K., Lin, C.-H., Lin, J.-K., Huang, G.-J., & Yu, J.-S. (2009). Diffuse reflectance spectroscopy detects increased hemoglobin concentration and decreased oxygenation during colon carcinogenesis from normal to malignant tumors. *Optics Express*, *17*(4), 2805-2817.
- [91] Richards-Kortum, R., Rava, R., Petras, R., Fitzmaurice, M., Sivak, M., & Feld, M. (1991). Spectroscopic diagnosis of colonic dysplasia. *Photochemistry and photobiology*, *53*(6), 777-786.

- [92] Georgakoudi, I., & Feld, M. S. (2004). The combined use of fluorescence, reflectance, and light-scattering spectroscopy for evaluating dysplasia in Barrett's esophagus. *Gastrointestinal Endoscopy Clinics*, 14(3), 519-537.
- [93] Wang, A. M. J., Nammalvar, V., & Drezek, R. A. (2007). Targeting spectral signatures of progressively dysplastic stratified epithelia using angularly variable fiber geometry in reflectance Monte Carlo simulations. *Journal of Biomedical Optics*, 12(4), 044012.
- [94] Vieira, S. C., Silva, B. B., Pinto, G. A., Vassallo, J., Moraes, N. G., Santana, J. O., . . . Zeferino, L. C. (2005). CD34 as a marker for evaluating angiogenesis in cervical cancer. *Pathology-Research and practice*, 201(4), 313-318.
- [95] Lee, J. S., Kim, H. S., Jung, J. J., Lee, M. C., & Park, C. S. (2002). Angiogenesis, cell proliferation and apoptosis in progression of cervical neoplasia. *Analytical and quantitative cytology and histology*, 24(2), 103-113.
- [96] Dellas, A., Moch, H., Schultheiss, E., Feichter, G., Almendral, A. C., Gudat, F., & Torhorst, J. (1997). Angiogenesis in cervical neoplasia: microvessel quantitation in precancerous lesions and invasive carcinomas with clinicopathological correlations. *Gynecologic Oncology*, 67(1), 27-33.
- [97] Lane, P. M., Gilhuly, T., Whitehead, P. D., Zeng, H., Poh, C., Ng, S., . . . MacAulay, C. E. (2006). Simple device for the direct visualization of oral-cavity tissue fluorescence. *Journal of Biomedical Optics*, 11(2), 024006.
- [98] Pavlova, I., Weber, C., Schwarz, R. A., Williams, M. D., Gillenwater, A. M., & Richards-Kortum, R. R. (2009). Fluorescence spectroscopy of oral tissue: Monte Carlo modeling with site-specific tissue properties. *Journal of Biomedical Optics*, 14(1), 014009.
- [99] Hasina, R., & Lingen, M. W. (2001). Angiogenesis in oral cancer. *Journal of dental education*, 65(11), 1282-1290.
- [100] Georgakoudi, I., Sheets, E. E., Müller, M. G., Backman, V., Crum, C. P., Badizadegan, K., . . . Feld, M. S. (2002). Trimodal spectroscopy for the detection and characterization of cervical precancers in vivo. *American journal of obstetrics and gynecology*, 186(3), 374-382.
- [101] Liu, Q., & Ramanujam, N. (2006). Sequential estimation of optical properties of a two-layered epithelial tissue model from depth-resolved ultraviolet-visible diffuse reflectance spectra. *Applied Optics*, 45(19), 4776-4790.

- [102] Shao, X., Zheng, W., & Huang, Z. (2010). Polarized near-infrared autofluorescence imaging combined with near-infrared diffuse reflectance imaging for improving colonic cancer detection. *Optics Express*, 18(23), 24293-24300.
- [103] Bedard, N., Pierce, M., El-Naggar, A., Anandasabapathy, S., Gillenwater, A., & Richards-Kortum, R. (2010). Emerging roles for multimodal optical imaging in early cancer detection: a global challenge. *Technology in cancer research & treatment*, 9(2), 211-217.
- [104] Boppart, S., Deutsch, T., & Rattner, D. (1999). Optical imaging technology in minimally invasive surgery. *Surgical endoscopy*, 13(7), 718-722.
- [105] Freeberg, J. A., Serachitopol, D. M., McKinnon, N., Price, R. L., Atkinson, E. N., Cox, D. D., . . . Pikkula, B. M. (2007). Fluorescence and reflectance device variability throughout the progression of a phase II clinical trial to detect and screen for cervical neoplasia using a fiber optic probe. *Journal of Biomedical Optics*, 12(3), 034015.
- [106] Twiggs, L. B., Chakhtoura, N. A., Ferris, D. G., Flowers, L. C., Winter, M. L., Sternfeld, D. R., . . . Wilkinson, E. J. (2013). Multimodal hyperspectroscopy as a triage test for cervical neoplasia: pivotal clinical trial results. *Gynecologic Oncology*, 130(1), 147-151.
- [107] Coda, S., Siersema, P. D., Stamp, G. W., & Thillainayagam, A. V. (2015). Biophotonic endoscopy: a review of clinical research techniques for optical imaging and sensing of early gastrointestinal cancer. *Endoscopy international open*, 3(05), E380-E392.
- [108] Hong, X., Nagarajan, V. K., Mugler, D. H., & Yu, B. (2016). Smartphone microendoscopy for high resolution fluorescence imaging. *Journal of Innovative Optical Health Sciences*, 9(05), 1650046.
- [109] Union, I. T. (2017). ICT facts and figures 2017. In: Author Geneva, Switzerland.
- [110] Breslauer, D. N., Maamari, R. N., Switz, N. A., Lam, W. A., & Fletcher, D. A. (2009). Mobile phone based clinical microscopy for global health applications. *PloS one*, 4(7), e6320.
- [111] Switz, N. A., D'Ambrosio, M. V., & Fletcher, D. A. (2014). Low-cost mobile phone microscopy with a reversed mobile phone camera lens. *PloS one*, 9(5), e95330.

- [112] Tseng, D., Mudanyali, O., Oztoprak, C., Isikman, S. O., Sencan, I., Yaglidere, O., & Ozcan, A. (2010). Lensfree microscopy on a cellphone. *Lab on a Chip*, 10(14), 1787-1792.
- [113] Zhu, H., Yaglidere, O., Su, T.-W., Tseng, D., & Ozcan, A. (2011). Cost-effective and compact wide-field fluorescent imaging on a cell-phone. *Lab on a Chip*, 11(2), 315-322.
- [114] Chu, K., Smith, Z. J., Espenson, A., Dwyre, D., Lane, S., Matthews, D., & Wachsmann-Hogiu, S. (2011). *Microscopy and spectroscopy on a cell phone*. Paper presented at the Laser Science.
- [115] Gallegos, D., Long, K. D., Yu, H., Clark, P. P., Lin, Y., George, S., . . . Cunningham, B. T. (2013). Label-free biodetection using a smartphone. *Lab on a Chip*, 13(11), 2124-2132.
- [116] Iqbal, Z., & Eriksson, M. (2013). Classification and quantitative optical analysis of liquid and solid samples using a mobile phone as illumination source and detector. *Sensors and Actuators B: Chemical*, 185, 354-362.
- [117] Smith, Z. J., Chu, K., Espenson, A. R., Rahimzadeh, M., Gryshuk, A., Molinaro, M., . . . Wachsmann-Hogiu, S. (2011). Cell-phone-based platform for biomedical device development and education applications. *PloS one*, 6(3), e17150.
- [118] Wang, S. X., & Zhou, X. J. (2008). Spectroscopic sensor on mobile phone. In: Google Patents.
- [119] Zhang, J. (2013). Spectrometers miniaturized for working with cellular phones and other portable electronic devices. In: Google Patents.
- [120] Edwards, P., Zhang, C., Zhang, B., Hong, X., Nagarajan, V. K., Yu, B., & Liu, Z. (2017). Smartphone based optical spectrometer for diffusive reflectance spectroscopic measurement of hemoglobin. *Scientific reports*, 7(1), 12224.
- [121] Bromwich, M. (2016). Adapter to couple a mobile phone to an endoscope. In: Google Patents.
- [122] Wu, C.-J., Wu, S.-Y., Chen, P.-C., & Lin, Y.-S. (2014). An innovative smartphone-based otorhinoendoscope and its application in mobile health and teleotolaryngology. *Journal of medical Internet research*, 16(3).
- [123] Jongsma, P. J., & Schölly, W. (2006). Device for coupling an endoscope to a videophone. In: Google Patents.

- [124] Beery, A. (2014). Introduction to mobileOCT's multimodal imaging. Retrieved from <http://www.mobileoct.com/introduction-to-multimodal.html>
- [125] Emptage, N. J. (2001). Fluorescent imaging in living systems. *Current opinion in pharmacology*, 1(5), 521-525.
- [126] Wainwright, M. (2001). Acridine—a neglected antibacterial chromophore. *Journal of Antimicrobial Chemotherapy*, 47(1), 1-13.
- [127] Browning, C., Gulbransen, R., & Thornton, L. (1917). The antiseptic properties of acriflavine and proflavine, and brilliant green: with special reference to suitability for wound therapy. *British medical journal*, 2(2951), 70.
- [128] Prieto, S. P., Powless, A. J., Boice, J. W., Sharma, S. G., & Muldoon, T. J. (2015). Proflavine Hemisulfate as a Fluorescent Contrast Agent for Point-of-Care Cytology. *PloS one*, 10(5), e0125598.
- [129] Albert, A. (1965). 864. Acridine syntheses and reactions. Part VI. A new dehalogenation of 9-chloroacridine and its derivatives. Further acridine ionisation constants and ultraviolet spectra. *Journal of the Chemical Society (Resumed)*, 4653-4657.
- [130] Dixon, J. M., Taniguchi, M., & Lindsey, J. S. (2005). PhotochemCAD 2: A Refined Program with Accompanying Spectral Databases for Photochemical Calculations¶. *Photochemistry and photobiology*, 81(1), 212-213.
- [131] Taniguchi, M., & Lindsey, J. S. (2018). Database of Absorption and Fluorescence Spectra of > 300 Common Compounds for use in Photochem CAD. *Photochemistry and photobiology*, 94(2), 290-327.
- [132] Prahl, S. (2017). Proflavin. Retrieved from <https://omlc.org/spectra/PhotochemCAD/html/078.html>
- [133] Melhuish, W. (1964). Measurement of quantum efficiencies of fluorescence and phosphorescence and some suggested luminescence standards. *JOSA*, 54(2), 183-186.
- [134] Du, H., Fuh, R. C. A., Li, J., Corkan, L. A., & Lindsey, J. S. (1998). PhotochemCAD‡: a computer-aided design and research tool in photochemistry. *Photochemistry and photobiology*, 68(2), 141-142.

- [135] Göbel, W., Kerr, J. N., Nimmerjahn, A., & Helmchen, F. (2004). Miniaturized two-photon microscope based on a flexible coherent fiber bundle and a gradient-index lens objective. *Optics letters*, 29(21), 2521-2523.
- [136] Winter, C., Rupp, S., Elter, M., Munzenmayer, C., Gerhauser, H., & Wittenberg, T. (2006). Automatic adaptive enhancement for images obtained with fiberoptic endoscopes. *IEEE transactions on biomedical engineering*, 53(10), 2035-2046.
- [137] Suter, M. J., McLennan, G., Reinhardt, J. M., Montague, P. R., Taft, P., Lee, J., & Zabner, J. (2005). Bronchoscopic imaging of pulmonary mucosal vasculature responses to inflammatory mediators. *Journal of Biomedical Optics*, 10(3), 034013.
- [138] Han, J., Lee, J., Lee, T., & Kang, J. (2010). Near infrared imaging of micro-structured polymer-metal surface pattern. *Opto-Electronics Review*, 18(2), 163-167.
- [139] Elter, M., Rupp, S., & Winter, C. (2006). *Physically motivated reconstruction of fiberoptic images*. Paper presented at the 18th International Conference on Pattern Recognition (ICPR'06).
- [140] Wiernik, G., Bradbury, S., Plant, M., Cowdell, R., & Williams, E. (1973). A quantitative comparison between normal and carcinomatous squamous epithelia of the uterine cervix. *British journal of cancer*, 28(6), 488.
- [141] Boas, D. A., Pitris, C., & Ramanujam, N. (2016). *Handbook of biomedical optics*: CRC press.
- [142] Prahl, S. (1999). Optical absorption of hemoglobin. <http://omlc.ogi.edu/spectra/hemoglobin>.
- [143] Jacques, S. L. (2013). Optical properties of biological tissues: a review. *Physics in Medicine & Biology*, 58(11), R37.
- [144] Yu, B., Shah, A., Wang, B., Rajaram, N., Wang, Q., Ramanujam, N., . . . Dewhurst, M. W. (2014). Measuring tumor cycling hypoxia and angiogenesis using a side-firing fiber optic probe. *Journal of biophotonics*, 7(7), 552-564.
- [145] Yu, B., Burnside, E. S., Sisney, G. A., Harter, J. M., Zhu, C., Dhalla, A.-H., & Ramanujam, N. (2007). Feasibility of near-infrared diffuse optical spectroscopy on patients undergoing image-guided core-needle biopsy. *Optics Express*, 15(12), 7335-7350.

- [146] Al-Rawi, P. G., Smielewski, P., & Kirkpatrick, P. J. (2001). Evaluation of a near-infrared spectrometer (NIRO 300) for the detection of intracranial oxygenation changes in the adult head. *Stroke*, 32(11), 2492-2500.
- [147] Wang, L., Jacques, S. L., & Zheng, L. (1995). MCML—Monte Carlo modeling of light transport in multi-layered tissues. *Computer methods and programs in biomedicine*, 47(2), 131-146.
- [148] Wang, L. V., & Wu, H.-i. (2012). *Biomedical optics: principles and imaging*: John Wiley & Sons.
- [149] Cappon, D., Farrell, T. J., Fang, Q., & Hayward, J. E. (2013). Fiber-optic probe design and optical property recovery algorithm for optical biopsy of brain tissue. *Journal of Biomedical Optics*, 18(10), 107004.
- [150] Ren, N., Liang, J., Qu, X., Li, J., Lu, B., & Tian, J. (2010). GPU-based Monte Carlo simulation for light propagation in complex heterogeneous tissues. *Optics Express*, 18(7), 6811-6823.
- [151] Palmer, G. M., & Ramanujam, N. (2006). Monte Carlo-based inverse model for calculating tissue optical properties. Part I: Theory and validation on synthetic phantoms. *Applied Optics*, 45(5), 1062-1071.
- [152] Bender, J. E., Vishwanath, K., Moore, L. K., Brown, J. Q., Chang, V., Palmer, G. M., & Ramanujam, N. (2009). A robust Monte Carlo model for the extraction of biological absorption and scattering in vivo. *IEEE transactions on biomedical engineering*, 56(4), 960-968.
- [153] Yu, B., Fu, H. L., & Ramanujam, N. (2011). Instrument independent diffuse reflectance spectroscopy. *Journal of Biomedical Optics*, 16(1), 011010.
- [154] Palmer, G. M., Viola, R. J., Schroeder, T., Yarmolenko, P. S., Dewhirst, M. W., & Ramanujam, N. (2009). Quantitative diffuse reflectance and fluorescence spectroscopy: tool to monitor tumor physiology in vivo. *Journal of Biomedical Optics*, 14(2), 024010.
- [155] Vishwanath, K., Yuan, H., Barry, W. T., Dewhirst, M. W., & Ramanujam, N. (2009). Using optical spectroscopy to longitudinally monitor physiological changes within solid tumors. *Neoplasia*, 11(9), 889-900.
- [156] Palmer, G. M., Zhu, C., Breslin, T. M., Xu, F., Gilchrist, K. W., & Ramanujam, N. (2006). Monte Carlo-based inverse model for calculating tissue optical properties. Part II: Application to breast cancer diagnosis. *Applied Optics*, 45(5), 1072-1078.

- [157] Brown, J. Q., Bydlon, T. M., Richards, L. M., Yu, B., Kennedy, S. A., Geradts, J., . . . Barry, W. T. (2010). Optical assessment of tumor resection margins in the breast. *IEEE Journal of selected topics in Quantum Electronics*, 16(3), 530-544.
- [158] Bohren, C. F., & Huffman, D. R. (2008). *Absorption and scattering of light by small particles*: John Wiley & Sons.
- [159] Graaff, R., Koelink, M., De Mul, F., Zijlstra, W., Dassel, A., & Aarnoudse, J. (1993). Condensed Monte Carlo simulations for the description of light transport. *Applied Optics*, 32(4), 426-434.
- [160] Kim, N.-H. (2018). How diffractive surfaces are modeled in OpticStudio. Retrieved from <https://customers.zemax.com/os/resources/learn/knowledgebase/how-diffractive-surfaces-are-modeled-in-zemax.aspx>
- [161] Newport. Technical Note: Focusing and Collimating. Retrieved from <https://www.newport.com/n/focusing-and-collimating>
- [162] Newport (Producer). Typical Spectra of Spectral Calib Lamps.
- [163] Hornung, R., Pham, T., Keefe, K., Berns, M., Tadir, Y., & Tromberg, B. (1999). Quantitative near-infrared spectroscopy of cervical dysplasia in vivo. *Human Reproduction*, 14(11), 2908-2916.
- [164] WHO. (2003). Intellectual property rights, innovation and public health. *World Health Assembly Resolution WHA56*, 27.
- [165] Nath, A., Rivoire, K., Chang, S. K., Cox, D. D., Atkinson, E. N., Follen, M., & Richards-Kortum, R. R. (2004). Effect of probe pressure on cervical fluorescence spectroscopy measurements. *Journal of Biomedical Optics*, 9(3), 523-534.
- [166] Chen, W., Liu, R., Xu, K., & Wang, R. K. (2005). Influence of contact state on NIR diffuse reflectance spectroscopy in vivo. *Journal of Physics D: Applied Physics*, 38(15), 2691.
- [167] Atencio, J. D., Guillén, E. O., y Montiel, S. V., Rodríguez, M. C., Ramos, J. C., Gutiérrez, J., & Martínez, F. (2009). Influence of probe pressure on human skin diffuse reflectance spectroscopy measurements. *Optical Memory and Neural Networks*, 18(1), 6-14.